Title	Generation mechanism of relativistic electron beams by high-intensity-laser-plasma interactions
Author(s)	小島, 完興
Citation	大阪大学, 2017, 博士論文
Version Type	VoR
URL	https://doi.org/10.18910/61503
rights	
Note	

Generation mechanism of relativistic electron beams by high-intensity-laser-plasma interactions

by

Sadaoki Kojima

Submitted to the Department of Physics, Graduate School of Science
in partial fulfillment of the requirements for the degree of

Doctor of Philosophy

at the

OSAKA UNIVERSITY, Osaka, JAPAN

March 2017

Author . . . .
Department of Physics, Graduate School of Science
March 22, 2017

Certified by . . . .
Shinsuke Fujioka
Professor of Institute of Laser Engineering, Osaka University
Thesis Supervisor

Accepted by . . . .
Department of Physics, Graduate School of Science
Osaka University

Generation mechanism of relativistic electron beams by high-intensity-laser-plasma interactions

by

Sadaoki Kojima

Submitted to the Department of Physics, Graduate School of Science
on March 22, 2017, in partial fulfillment of the
requirements for the degree of
Doctor of Philosophy

Abstract

Fast Ignition is an alternative scheme for Inertial Confinement Fusion (ICF) that uses a picosecond heating laser to ignite a hot spot in precompressed fuel. The heating laser energy converts into energy of relativistic electrons by laser plasma interaction and these electrons propagate through a plasma to the fuel core and deliver their energy to the fuel core. When the range of relativistic electrons in the fuel becomes to be less than the areal density of the fuel core, the heating efficiency is maximized. Electrons of energies between 1 and 3 MeV have the appropriate range for efficient heating. Thus a quantitative understanding of the mean energy and energy conversion efficiency, and how it responds to variable laser parameters is of paramount importance for fast ignition. In order to determine optimum laser intensity, the dependence of the mean energy of the relativistic electrons on the laser intensity was investigated, and the widely used Ponderomotive scaling law etc. were derived.

As a result of the large scale simulation carried out in recent years, the dependence of the mean energy of relativistic electrons on the pulse duration of the heating laser, which was not considered in the above scaling lows, was revealed. This result was concluded that when the pulse duration becomes long, the heating laser itself generates plasma with long scale length, and the interaction of this plasma with the high intensity laser increases the average energy of relativistic electrons and the energy conversion efficiency. Experimental verification is indispensable because the dependence of the mean energy of relativistic electrons on laser pulse duration is a crucial problem on the optimization of the parameters of the heating laser suitable for fast ignition laser fusion.

For the first time, this study has experimentally demonstrated the effect of the pulse duration of the heating laser on the mean energy of relativistic electrons and the energy conversion efficiency. In carrying out this research, it was necessary to suppress generation of pre-formed plasma (hereinafter referred to as "preplasma") created by foot pulse, pedestal and prepulse, (hereinafter referred to as "preceding pulses ") which are irradiated to the target before reaching the main pulse of the heating laser. "pulse contrast ratio" defined by the intensity ration between the main pulse and the preceding pulses is used as a parameter for evaluating the characteristics of the heating laser.

Using a laser with a pulse contrast ratio of below of 10^{-9}, it is impossible to extract the electron acceleration mechanism by only the main pulse, because the preceding pulses create a preplasma with a scale length which is longer than that of a plasma generated by the main pulse. Therefore, the plasma mirror was introduced to remove the preceding pulses and to improve the pulse contrast.

The laser energy fluence on the surface of the plasma mirror was optimized to realize a plasma mirror with high reflectivity and high spatial uniformity. We had implemented the optimized plasma mirror system in kJ class, picosecond laser, and realized high contrast ratio of 10^{-11} at 1.3 ns before main pulse, so that we successfully suppressed the undesirable preplasma formation.

Furthermore, in carrying out this research, it was necessary to establish a new measurement method for average energy of relativistic electrons and energy conversion efficiency. In previous studies, only electrons that escaping into the vacuum from the plasma out of the all electrons accelerated by a heating laser were observed. In this method, relatively low energy electrons contributing to heating can not be detected because they are trapped by the electric and magnetic field developed around the plasma. While in this study, we converted relativistic electrons into bremsstrahlung x-rays that dose not be trapped by the field. Absolute energy distribution of electrons were obtained from bremsstrahlung x-ray spectrum by using Monte Carlo simulation to calculate charged-particle-matter interaction. In order to measure the x-ray energy spectrum via bremsstrahlung, we developed Compton x-ray spectrometer, and it obtained higher spectral resolution than that of conventional bremsstrahlung x-ray spectrometers.

The above two improvements enabled us to study relativistic electrons acceleration mechanism in an inherent plasma formed by the multi-picosecond main laser pulse itself. Experimentally measured slope temperatures are far beyond the previously reported intensity scaling laws, in which the effect of the pulse duration on the electron acceleration is not considered. Experimental results were analyzed using two-dimensional particle-in-cell simulation. We had revealed that the increasing of average energy of relativistic electrons due to the long pulse irradiation causes not only to the long scale plasma generated by the main pulse itself but also to the quasi-static electric field and magnetic field spontaneously generated in the plasma. The quasi-static electric field effects on relativistic electron acceleration, and the quasi-static magnetic field effects on relativistic electron transport. When the quasi-static electric field is developed, the velocity of the relativistic electron becomes close to the phase velocity of the laser field and the some of relativistic electrons remains to move with the acceleration phase, whereby the relativistic electron gains energy from the laser field.

Moreover, when the quasi-static magnetic field glows strong enough to reflect relativistic electrons coming from the laser plasma interaction region back again there, the reflected relativistic electrons gain additional energy by the laser field in the quasi-static electric field. The strength of quasi-static magnetic field becomes several tens of megagauss approximately several picoseconds after the beginning of the laser-plasma interaction.

Mean energy of relativistic electrons depends on not only laser intensity but also pulse duration because the quasi-static electric and magnetic fields develop with time. These acceleration mechanism must be considered to determine laser parameters for high intensity laser experiments and applications such as the fast ignition inertial confinement fusion and the laboratory astrophysics with a multi-ps intense laser pulse. The relation between the pulse duration of the laser and the time scale of the quasi-static electric field and the growth of the magnetic field was examined, and guidelines for determining the optimum laser parameters for fast ignition laser fusion were obtained.

Osaka, Japan
March, 2017

Sadaoki Kojima

Thesis Supervisor: Shinsuke Fujioka
Title: Professor of Institute of Laser Engineering, Osaka University

Acknowledgments

First and foremost, I want to express my deepest gratitude to my academic advisor, Prof. Shinsuke Fujioka and Prof. Hiroshi Azechi. Not only did they give me the opportunity to do a Ph.D. with them, they have provided me with unending encouragement, support, and guidance the past several years. They have generously given me opportunities to grow as an experimentalist, and taught me to think on my feet, and trusted me to work independently.

I would like to acknowledge with Lecturer Yasunobu Arikawa and Assistant Prof. Alessio Morace, that allowed me to follow my interests and helped me in any way they could to allow me to have the most fruitful possible experience. Especially in the development of plasma mirrors, their precise advice and wonderful ideas have led the experiment to success. To Dr. Masayasu Hata, for all the support about my all works, I would not make it without you. He has provided so much patience and assistance and advice.

Huge thanks are due to Prof. Yasuhiko Sentoku and Dr. Natsumi Iwata, who made a great contribution to the construction of the new model for overdense plasma compression by a laser. They were always helpful and patient with me, and allowed me to ask hundreds of dumb questions.

I would like to thank Prof. Mitsuo Nakai, Prof. Hiroaki Nishimura, Associate prof. Akifumi Yogo, and Prof. Hiroyuki Shiraga for their patience and the support and the guidance they has given me throughout this work. Especially in the development of the Compton X-ray spectrometer, I got a lot of great advice from them and I was able to complete this task. I would like to acknowledge Associate prof. Hideo Nagatomo, Associate prof. Keisuke Shigemori, Associate prof. Youichirou Hironaka, Assistant Prof. Takayoshi Sano, Associate prof. Youichi Sakawa, Associate prof. Junji Kawanaka, Assistant Prof. Shigeki Tokita, Prof. Noriaki Miyanaga, Prof. Masakatsu Murakami, Prof. Nobuhiko Sarukura, Prof. Takayoshi Norimatsu, Dr. Atsushi Sunahara (Institute for Laser Technology), Associate Prof. Tomoyuki Johzaki (Hiroshima University), Associate Prof. Tetso Ozaki (National Institute for Fusion Science), and Prof. Hitoshi Sakagami (National Institute for Fusion Science), for providing me a wonderful research environment. I also acknowledge Dr. Akito Sagisaka, Dr. Koichi Ogura, Dr. Alexander. S. Pirozhkov, Dr. Masaharu Nishikino and Dr. Kiminori Kondo of the Kansai Photon Science Institute, National Institutes for Quantum and Radiological Science and Technology, and Assistant Prof. Shunsuke Inoue, Mr. Kensuke Teramoto, Associate Prof. Masaki Hashida, and Prof. Shuji Sakabe of the Advanced Research Center for Beam Science Institute for Chemical Research, Kyoto University for valuable discussions of laser contrast improvement using a plasma mirror. And thank yous all around to a multitude of people I had the privilege of doing experiments with and learning from: Shouhei Sakata, Yuki Abe, Yuki Taguchi, Lee Seungho, Kazuki Matsuo, King Fai Farly Law, Takayuki Gawa, Shota Tosaki, Takahito Ikenouchi and Takuya Namimoto. The authors thank the technical support staff of the Institute of Laser Engineering at Osaka University and Plasma Simulator at the National Institute for Fusion Science for assistance with laser operation, target fabrication, plasma diagnostics, and computer simulations. I would especially thank Associate Prof. Joao Jorge Santos, Dr. Hui Chen, Dr. Jackson Williams and all the international groups I had the fortune to work with: at University of Bordeaux, LULI, LLNL, CLPU, CELIA, Chinese Academy of Sciences. The list of outstanding people I had the fortune to meet is too long to be reported here, I hope you will forgive me.

This work was supported by Grant-in-Aid for JSPS Research Fellow (No. 14J06592) from the Japan Society for the Promotion of Science. At last, I would like to thank my parents and my girl friend for their support and encouragement.

This doctoral thesis has been examined by a Committee of the Department of Physics as follows:

Professor Shinsuke Fujioka . . . .
Thesis Supervisor & Chairman, Thesis Committee
Professor of Institute of Laser Engineering, Osaka University

Professor Tadashi Shimoda . . . .
Member, Thesis Committee
Professor of Department of Physics, Graduate School of Science, Osaka University

Professor Hiroshi Azechi . . . .
Member, Thesis Committee
Professor of Institute of Laser Engineering, Osaka University

Professor Mitsuo Nakai . . . .
Member, Thesis Committee
Professor of Institute of Laser Engineering, Osaka University

Professor Yasuhiko Sentoku . . . .
Member, Thesis Committee
Professor of Institute of Laser Engineering, Osaka University

Sunset over the Savannah River

57th Annual Meeting of the APS Division of Plasma Physics,
Savannah, Georgia, USA, November 20, 2015

Blue sky of Paris seen from under the Eiffel Tower

Experiments on LULI 2000 facility of École Polytechnique,
France, August, 2015

Contents

List of Figures

List of Tables

CHAPTER 1

Inertial confinement fusion (ICF)

1.1 | Fusion basics

The growth in global energy requirements has resulted in an effort to develop alternative energy sources. In Japan, moreover a powerful earthquake and tsunami occurred at northeast Japanese coast, severely damaged the Fukushima power plant and then large quantities of radioactive material was released in the surrounding areas. As appeared clear after this serious accident, nuclear fission power plant is not completely safe in terms of accidents or terroristic attacks. Therefore, new safe alternative energy sources are requested. Nuclear fusion has many desirable attributes and has emerged as an important candidate of energy source of future.

When two nuclei combine, a huge amount of energy is released. And this energy is called fusion energy. This energy comes from the mass difference between the fusion products and the original interacting nuclei. The energy released is calculated from Einstein's famous relationship $E = mc^2$.

Two nuclei fuse when interacting nuclei have enough energy to overcome the Coulomb barrier of each other and get into the nuclear potential well. The maximum Coulomb barrier is given by

$$V_b = \frac{Z_1 Z_2}{A_1^{1/3} + A_2^{1/3}} \quad \text{MeV}. \tag{1.1}$$

where Z_1 and Z_2 are the nuclear charges. A_1 and A_2 are the atomic numbers. The maximum Coulomb barrier energy is of order of 1 MeV. For example, the Coulomb barrier of two hydrogen nuclei is about 700 keV. The equivalent temperatures is 3.6×10^9 K, which is not a realistic prospect. Indeed, fusion processes can still occur via tunneling even if the energies of interacting nuclei are slightly less than that required to overcome the Coulomb barrier. The tunneling probability increases if the kinetic energy of the incoming nucleus increases.

The lowest binding energies are for hydrogen and its isotopes, deuterium (D) and tritium (T), and for ^{3}He. When these nuclei fuse into heavier elements, energy equivalent to the difference in the binding energy is released.

Figure 1.3 shows the reaction rate for various fusion reactions as a function of the temperature. Amongst all reactions the Deuterium-Tritium one is the most efficient for the temperatures and densities reached in a laboratory. Deuterium and tritium are isotopes of hydrogen and they have respectively one and two extra neutron. The fusion products of D-T reaction are an alpha particle (helium nucleus) with a kinetic energy of 3.6 MeV and a neutron with a kinetic energy of 14.1 MeV,

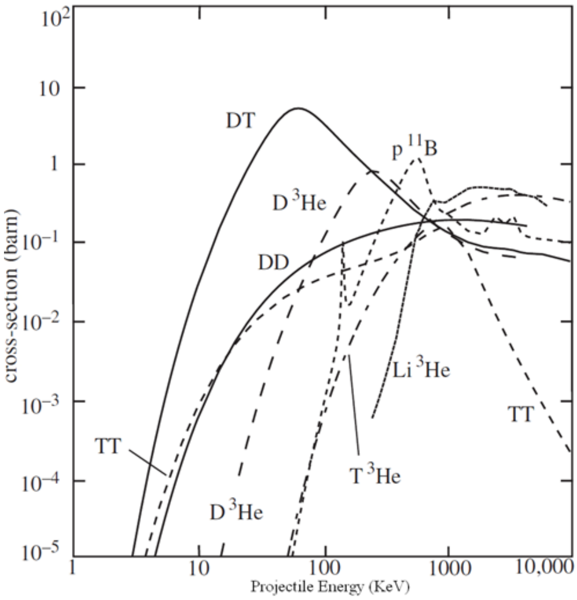

Figure 1-1: Fusion cross sections for hydrogen isotopes and light elements versus ion temperature. The D-T reaction has the highest reaction rate in the entire energy range below 400 keV. Figure taken from Atzeni and Meyer-Ter-Vehn, *The Physics of Inertial Fusion: Beam Plasma Interaction, Hydrodynamics, Hot Dense Matter* (2004).

$$\mathrm{D} + \mathrm{T} = \alpha\ (3.6\ \mathrm{MeV}) + \mathrm{n}\ (14.1\ \mathrm{MeV}) \tag{1.2}$$

This reaction has a number of advantages. Deuterium is supplied from seawater while Tritium is produced by Li-n reaction, using the neutrons generated in the nuclear fusion process. Therefore it is easy to obtain large quantities of the fuel components. And its estimates indicating that there is enough to last for millennia. Since carbon dioxide is not emitted, unlike classic oil thermal power generation, environmental impact is estimated to be low. Moreover, unlike nuclear fission, the production of nuclear waste is minimal and high level radioactive waste with long half-life is not created. In an emergency situation such as large earthquake, because fusion does not rely on a chain reaction, the possibility of a reactor meltdown is precluded.

1.2 | Energy balance and Lawson criterion

Two major approaches to fusion are magnetic confinement fusion (MCF) and inertial confinement fusion (ICF). The MCF uses magnetic field to confine the fuel and plasma is constrained to travel along magnetic field lines. The ICF uses the inertia of an imploding shell driven by laser to confine the fuel. The inertia can hold the fuel for a period of time corresponding to the speed of a sound wave traveling from the surface to the center of the ignited fuel shell. i.e., the confinement time τ can be roughly estimated by the ratio of shell radius R over the sound speed, as $t_c \simeq R/c_s$. For a 100 μm target of current design, the confinement time is roughly 10^{-9} s. Numerical simulations indicates that about 10-20 ns are more realistic. This means that incredibly high plasma densities must be achieved in order for a large amount of the fuel to be burned in the short confinement time.

The minimum confinement time and density required for a fusion plasma is estimated by the condition for balancing the energy generated by the nuclear fusion reaction with the energy losses. We consider a steady state burning fusion plasma which satisfies power balance. It is heated by energy deposition of α-particle (P_α). It cools due to diffusive losses (P_{dif}). The power balance is represented by

$$\begin{aligned} P_\alpha &= P_{dif} \\ \frac{n^2}{4}\langle\sigma v\rangle Q &= \frac{3nk_BT}{\tau} \end{aligned} \tag{1.3}$$

To produce energy from nuclear fusion reaction, the energy obtained from the fusion processes has to be greater than the energy to heat the plasma to such high temperatures. Re-expressed as

$$n\tau > \frac{12k_BT}{\langle\sigma v\rangle Q} \tag{1.4}$$

this relation is called Lawson criterion (Lawson, 1957). Here, v is the relative velocity of the two nuclei and σ the D-T fusion cross section. Q is the kinetic energy of the reaction products given in MeV. n is the number of particles per cm^3 and τ the confinement time.

In addition to the request for fuel confinement, there is a request for fuel temperature. i.e., the fusion particles have to have enough kinetic energy for a sufficient number of fusion reactions to take place in the confinement time. For DT fuel, this temperature is approximately 5-10 keV. In this case, the Lawson criterion becomes

$$n\tau \sim 10^{14} - 10^{15} \quad \mathrm{cm}^{-3}\,\mathrm{s}. \tag{1.5}$$

Since the confinement time is extremely short ($\leq 10^{-10}$ s) in the ICF, the particle densities are typically greater than 10^{25} cm^{-3}.

1.3 | Inertial confinement fusion (ICF)

The high-gain DT fuel shell for the ICF, consists of a spherical shell filled with deuterium-tritium gas (≤ 1.0 mg/cm^3). By cooling the target to cryogenic temperature, an ice layer of fuel is formed on the inner surface of the shell, and the center of shell is filled with a saturated vapor pressure gas. There are two primary schemes for shell implosion using laser. First one is direct drive scheme, in which the lasers are directly irradiated on the shell. Second one is indirect drive scheme, in which the lasers are first irradiated on a high-Z hohlraum such as gold. Then, the shell is compressed by x-rays emitted from hohlraum. In both the direct and indirect drive schemes, the energy of the laser is rapidly delivered to the outer surface of shell called ablator. The heated ablator then expands outwardly. The outward momentum of the ablator then impart inward momentum to the rest of the shell. The shell acceleration is produced by ablation pressure in a rocket-like reaction. And the shell begins compressing and heating the fuel via shocks and PdV work.

1.3.1 | Burn efficiency and areal density of fuel

The burn efficiency is defined by

$$\Phi_b = N_{fus}/N_{DT}^{(0)} \tag{1.6}$$

Here, N_{fus} is total number of D-T fusion reaction and $N_{DT}^{(0)}$ is number of DT pairs initially include in the plasma volume V_0. Let us assume that a DT fuel is uniformly compressed with density ρ, radius R, and temperature T. For the case equimolar DT fuel, the number density of DT ($n_D = n_T$) evolves in time according to the equation

$$\frac{\mathrm{d}n_D}{\mathrm{d}t} = -n_D(t)n_T(t)\langle\sigma v\rangle \tag{1.7}$$

where $\langle\sigma v\rangle$ is the velocity averaged D-T fusion reaction cross section. By assuming that the fusion reaction continues for the confinement time τ and integrating Eq.(1.7) with respect to time, we obtain the burn efficiency Φ defined by

$$\Phi_b = 1 - \frac{n_D(t=\tau)}{n_D(t=0)} = 1 - \frac{n_T(t=\tau)}{n_T(t=0)} = \frac{\tau/\tau_r}{1+\tau/\tau_r} \tag{1.8}$$

where $\tau_r = \langle\sigma v\rangle n_D(t=0)$. The fuel is confined for a period of time corresponding to the speed of a sound wave traveling from the surface to the center of the ignited fuel. However, since the fuel temperature sharply decreases in the region where the rarefaction wave propagates and does not contribute to the nuclear fusion reaction. If we also take into account the substantially contribution of fuel to the nuclear fusion, the effective disassembly time can be roughly estimated by

$$\tau \sim R/4C_s. \tag{1.9}$$

By inserting Eq.(1.9) into Eq.(1.8), the burn fraction Φ_b is given to be

$$\Phi_b \sim \frac{\rho R}{\rho R + H_B(T)} \tag{1.10}$$

where $H_B(T)$ is function of temperature only and defined by

$$H_B(T) = \frac{8m_iC_s}{\langle\sigma v\rangle}. \tag{1.11}$$

Burn parameter $H_B(T)$ has a strong dependence on temperature (e.x. $H_B(T)$=24 g/cm^2 at 10 keV and $H_B(T)$=7 g/cm^2 at 30 keV) and Φ_b at 20-40 keV burn temperature is approximately given by

$$\Phi_b \sim \frac{\rho R}{6+\rho R} \tag{1.12}$$

ρR is areal density in g/cm^2. From the above equation, $\rho R > 3$ g/cm^3 is need for efficient fusion burn (about 30% of burn efficiency is obtained.). The fuel mass to obtain this areal density is described by

$$M = \frac{4\pi}{3}\rho R^3 = \frac{4\pi}{3}\frac{(\rho R)^3}{\rho^2} \tag{1.13}$$

The mass M is proportional to $1/\rho$. If we try to achieve this areal density without fuel compression (i.e. the fuel density is 0.21g/cm^3 of the solid density), the total mass of the fuel needs 2.5 kg. The energy released in the burn of a fusion capsule is substantial. In order to use at a nuclear fusion reactor, the total fuel mass must be limited to 10 mg. With the ρR constraint, this sets the required fuel density at 300-1000 times solid density.

If we get the high density fuel with 1000 times solid density, 2.5 mg of mass is enough to satisfies the condition of $\rho R > 3$g/cm^2. These high density fuel can be achieved through spherical implosions. This idea was first published by Nuckolls *et al.* in 1972.[1] A nuclear fusion reactor output power of

3 million kW can be obtained by causing fusion burn more than 10 times per second. This output power is equivalent to that of the current nuclear power reactor.

1.3.2 | Ignition temperature

A minimum temperature required for ignition is given by power balance between the bremsstrahlung losses and the α-particle heating as first rough estimation. Approximate equations for bremsstrahlung power loss and α-particle heating are respectively given by

$$P_{brem} \sim 5.34 \times 10^{-25} n^2 T_{\mathrm{keV}} \quad (\mathrm{W/m^3}), \tag{1.14}$$

$$P_{alpha} \sim 5.15 \times 10^{-19} n^2 T_{\mathrm{keV}}^{2/3} \quad (\mathrm{W/m^3}), \tag{1.15}$$

where $n = n_D/2 = n_T/2 = n_i = n_e$. We should note that above two equations is only accurate for temperatures up to 25 keV. These equations are plotted in Fig.1-2 From the graph, it can be seen that the minimum temperature required in the plasma is 4.3 keV. Below this temperature bremsstrahlung loss exceeds the heating by α-particles, and the plasma does not burn. In fact, even higher temperatures are required due to other loss mechanisms and incomplete confinement of α-particles.

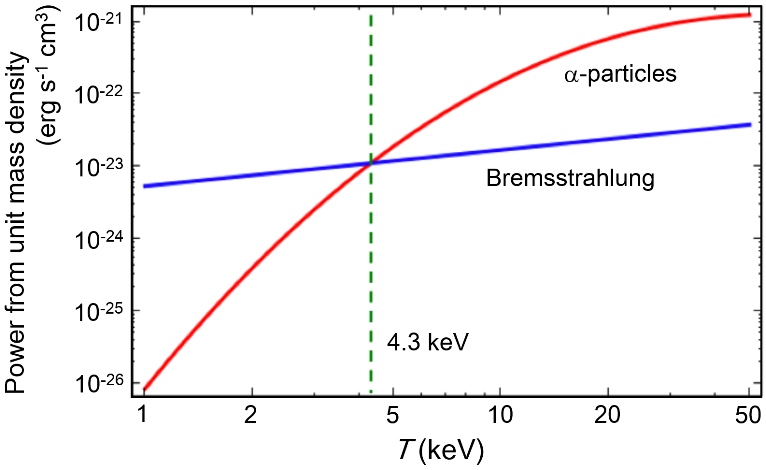

Figure 1-2: A minimum temperature required for ignition. The minimum temperature required in the plasma is 4.3 keV. Below this temperature bremsstrahlung loss exceeds the heating by α-particles, and the plasma does not burn.

1.4 | Fast Ignition (FI)

1.4.1 | Fast ignition concept

Fast ignition is an alternative scheme for Inertial Confinement Fusion (ICF) that uses a picosecond heating laser to ignite a hot spot in pre-compressed fuel. The process of fast ignition is composed of the capsule implosion phase, and fuel heating phase. The heating laser energy converts into energy

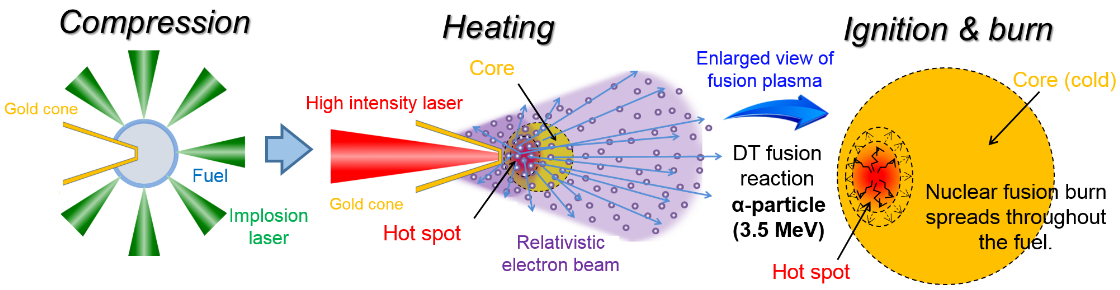

Figure 1-3: Fast ignition concept: Fast ignition is an alternative scheme for Inertial Confinement Fusion that uses a picosecond heating laser to ignite a hot spot in pre-compressed fuel. The process of fast ignition is composed of the capsule implosion phase, and fuel heating phase.

of relativistic electrons by laser plasma interaction and these electrons propagate to the fuel core and deliver their energy to a hot spot. It was first proposed by Tabak *et al.* [2] in 1994, a few years after the development of Chirped Pulse Amplification (CPA) lasers [3] that made possible the delivery of large amounts of energy in timescales short enough for fusion confinement. Since the implosion does not need to create a compressed hot spot, Fast Ignition concept promises higher gains, lower sensitivity to hydrodynamic instabilities, and reduced driver energy when compared to conventional hot spot ICF.

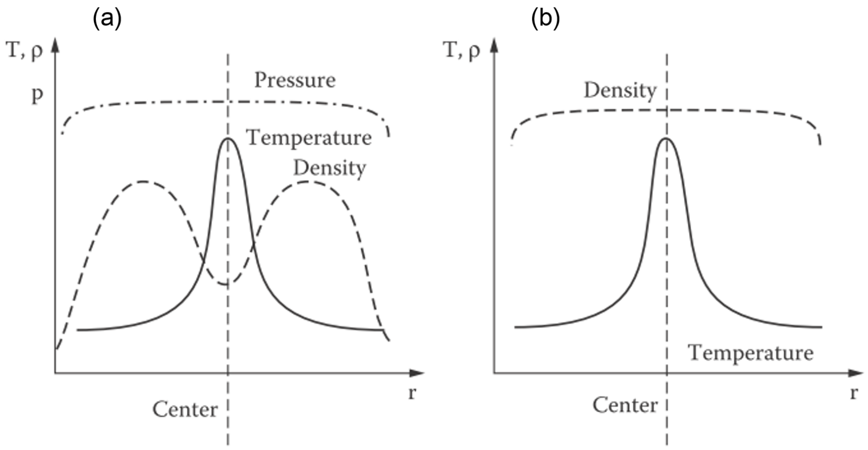

Figure 1-4: Schematic picture of the temperature and density as function of the radius in the (a) conventional hot spot concept and (b) fast ignition concept. Figure taken from S. Pfalzner, *An Introduction to Inertial Confinement Fusion* .

Figure 1-4 shows schematic picture of the temperature and density as function of the radius in the (a) conventional hot spot concept and (b) fast ignition concept. In conventional hot spot concept, the low temperature main fuel surrounds the high temperature hot spot. These two layers were in pressure equilibrium so that the hot spot density had to be about 10 times lower than the main fuel density (see Fig.1-4(a)). In contrast, in the fast ignition concept (see Fig.1-4(b)), such a low-density hot central region is not necessary and there is no need to be pressure equilibrium. Therefore, the central density can be significantly higher than in the hot-spot case. As a result, it is possible to reduce the radius of the area corresponding to the hot spot compared with the hot spot concept. A larger gain could therefore be achieved because the actual burn mass would be larger or the required laser energy would be smaller for the same gain. The crucial question for the fast-ignition concept is whether it is possible to deliver the ignition energy to the pre-compressed core. One obstacle to delivering ignition energy into the core is an extended corona. The short-pulse laser somehow has to penetrate this corona and deliver its energy to the overdense regions in the center. It is hoped that making use of relativistic effects and the ponderomotive pressure, a way could be found to bring the intense light much closer to the compressed core. There are two main suggestions how to achieve this: hole boring scheme or cone guide scheme.

1.4.2 | Beam parameters for ignition

General electron beam requirements for fast ignition were determined by a large series of two-dimensional hydrodynamics simulations. Atzeni *et al.* performed the simulation, where the ignition energy is injected by electron beam into pre-compressed DT fuel, at uniform density and they reported allowable ignition windows by the fast ignition approach, as in Fig.1-5. [4]

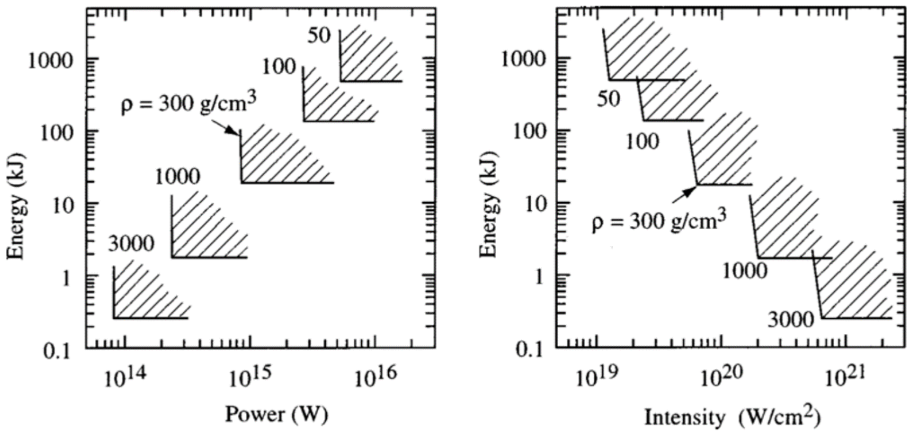

Figure 1-5: Schematic picture of the temperature and density as function of the radius in the (a) conventional hot spot concept and (b) fast ignition concept. Figure taken from S. Atzeni, *Inertial fusion fast ignitor: Igniting pulse parameter window vs the penetration depth of the heating particles and the density of the precompressed fuel* (1999).

It was found that the minimum value of energy, power and intensity shown in the lower left corner of the hatched area in this figure can be approximated by

$$E_{opt} = 140\left(\frac{\rho}{100(\mathrm{g/m^3})}\right)^{-1.85} \quad (\mathrm{kJ}), \tag{1.16}$$

$$W_{opt} = 2.6\times10^{15}\left(\frac{\rho}{100(\mathrm{g/m^3})}\right)^{-1} \quad (\mathrm{W}), \tag{1.17}$$

$$I_{opt} = 2.4\times10^{19}\left(\frac{\rho}{100(\mathrm{g/m^3})}\right)^{0.95} \quad (\mathrm{W/cm^2}), \tag{1.18}$$

where ρ is the density in unit of 100 g/cm^3. Corresponding pulse duration and focal spot size are

$$t_{opt} = 54\left(\frac{\rho}{100(\text{g/m}^3)}\right)^{-0.85} \quad (\text{ps}), \tag{1.19}$$

$$r_{opt} = 60\left(\frac{\rho}{100(\text{g/m}^3)}\right)^{-0.97} \quad (\mu\text{m}). \tag{1.20}$$

According to this approximation formula, the optimal set of parameters of electron beam to ignite compressed DT plasma at a density of 300 g/cm^3 are 6.8×10^{19} W/cm^2, with > 18 kJ of the laser energy. Duration of electro beam is 20 ps and it should be injected in a < 40 μm diameter hot spot.

In the above simulation, energy deposition into the plasma by parallel cylindrical electron beams with a range of R and a radius of r_b was considered The electron beam had uniform stopping power in the plasma, and the path was assumed to be straight. The above equation can be applied to particle penetration depth $0.3 \leq R \leq R_0 = 1.2$ g/cm^2, and further energy is required when the electron beam has a longer range ($R \geq 1.2$ g/cm^2).

Tabak *et al.* [5] reported equations extended to account also for the non optimal range and focal spot, they can be written by

$$\begin{aligned} E_{ign} \geq E_{opt}(\rho) \times \max\left(1, \frac{R}{R_0}\right) \quad (\text{kJ}), \\ \times \begin{cases} \max\left(1; \frac{r_b}{r_{opt}}\right), & r_b \leq 2.5 r_{opt} \\ 2.5\left(\frac{r_b}{2.5 r_{opt}}\right)^2, & r_b \geq 2.5 r_{opt} \end{cases} \end{aligned} \tag{1.21}$$

$$\begin{aligned} I_{ign} \geq I_{opt}(\rho) \times \max\left(1, \frac{R}{R_0}\right) \quad (\text{W/cm}^2), \\ \times \begin{cases} \min\left(1; \frac{r_b}{r_{opt}}\right), & r_b \leq 2.5 r_{opt} \\ 0.4, \quad r_b \geq 2.5 r_{opt}. \end{cases} \end{aligned} \tag{1.22}$$

If we consider more realistic Gaussian profile of electron beam it leads to energy requirements larger by about 30%.

1.4.3 | Laser parameters for ignition

In this section the laser parameters required for ignition are described. Electron beam in fast ignition are produced in the interaction of ultra-intense laser pulses with solid target. The average energy of electron beam and the energy conversion efficiency from the laser to electrons generally depend on the details of this interaction. An assumption, however, is often used that the average energy of electron beam equals the energy of their oscillation in the laser field (i.e., Ponderomotive energy). [6], [7] Ponderomotive energy with a function of laser intensity and wavelength can be written as [8]

$$T_{hot} = \sqrt{\frac{I_{ign}^{laser}}{1.2 \times 10^{19}\ \text{W/cm}^2}\left(\frac{\lambda_{ign}}{1.06\ \mu\text{m}}\right)^2} \quad (\text{MeV}), \tag{1.23}$$

where I_{ign} laser is the incident laser intensity and λ_{ign} is the laser wavelength. Moreover, the penetration depth of monoenergetic electrons is often approximated by the expression R(g/cm^2)

=0.6T_{hot}(MeV). Therefore, the range of electrons can be expressed as

$$R = 0.6 f_R \sqrt{\frac{I_{ign}^{laser}}{1.2 \times 10^{19}\ \mathrm{W/cm^2}} \left(\frac{\lambda_{ign}}{1.06\ \mu\mathrm{m}}\right)^2} \quad (\mathrm{g/cm^2}), \tag{1.24}$$

using laser intensity and wavelength. The parameter f_R accounts for range reduction or lengthening. For instance, Li and Petrasso [9] have studied the collisional stopping of electron beam in pre-compressed plasma with accurate models. They reported that an initially cylindrical beam blooms somewhat and that, due to straggling, deposition is enhanced at the end of the path, and the penetration depth decreases by about 20%.

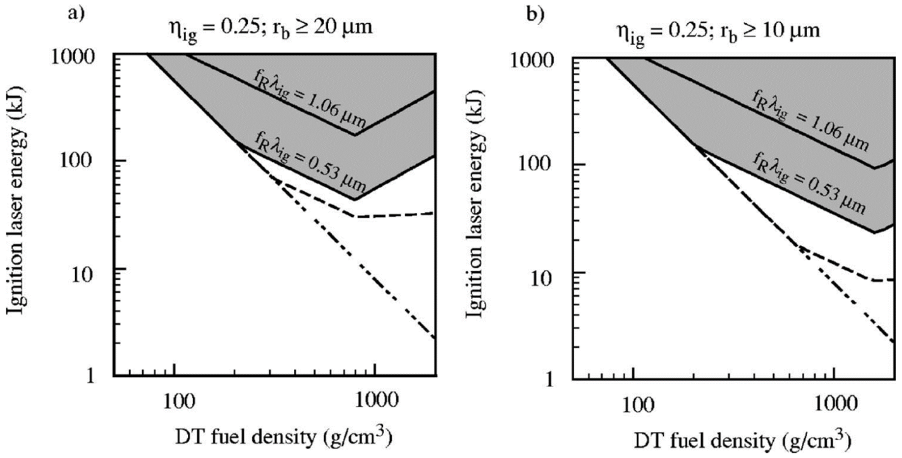

Figure 1-6: Laser ignition energy for electron beam driven fast ignition versus density of the pre-compressed fuel, for different values of the parameter $f_R\lambda_{ign}$ (see labels on the solid curves), and two different values of the minimum spot radius, (a) rb ≥20 μm; and (b) rb ≥10 μm. and energy conversion efficiency η_{ign}=0.25. Figure taken from S. Atzeni and A. S. Bellei *et al.*, *Targets for direct-drive fast ignition at total laser energy of 200-400 kJ* (2007).

Figure 1-6 shows heating laser energy thresholds for fast ignition versus fuel density. The figure shows that if the laser wavelength is 1.06 μm and there is no range shortening, fast ignition requires ignition pulses with energy well above 100 kJ. Ignition with less than 100 kJ and focal spot $r_b \geq$ 20 μm requires $f_R\lambda_{ign} \leq 0.5$ μm, i.e. either range shortening and/or shorter wavelength laser light. The corresponding fuel density is in the range 300-500 g/cm^3. [10]

Calculation of parameters of the heating laser considering the dependence of laser intensity on the average energy of electrons has also been reported by Solodov *et al.* [11]. They performed simulations assuming a Gaussian temporal profile for the laser pulse and a relativistic Maxwellian distribution function for electron beam with ponderomotive energy. In addition, two values of the energy conversion efficiency from laser to electron beam were used with reference to experimental results: η=0.3 and η=0.5. Simulations were performed by using different parameters of the laser pulse such as spot size, duration, wavelengths of 1.06 and 0.53 μm. Average density of pre-compressed fuel was assumed to be 450 g/cm^3.

Using a smaller beam radius and pulse duration leads to higher intensities and more energetic electrons, according to the ponderomotive scaling Eq.1.24. However, very energetic (multi-MeV) electrons require a large stopping range that exceed the size of optimum range. Larger beam radius with ρr_b ≥0.6 g/cm^2 lead to a heated volume greater than the optimal value. In addition, very long laser pulses with duration exceeding the confinement time of the heated region are detrimental and lead to a higher ignition energy. Thus, optimal values of the duration and radius exist for which the laser ignition energy is minimized.

They performed a set of simulations to find optimum conditions. Summary of the results are shown in Tables 1.1 and 1.2.

Table 1.1: Optimal values of the duration and radius for ignition for λ=1.054 μm

η_{L-e}	r_b (μm)	τ (ps)	E^{min}_{Laser}	E^{min}_{e}	T_{hot}	η_{e-pla}
0.3	26.3	16.3	235	71	7.7	0.69
0.5	22.5	13.8	105	53	6.3	0.79

Table 1.2: Optimal values of the duration and radius for ignition for λ=0.527 μm

η_{L-e}	r_b (μm)	τ (ps)	E^{min}_{Laser}	E^{min}_{e}	T_{hot}	η_{e-pla}
0.3	19	8	106	32	3.7	0.86
0.5	16.8	7	50	25	3.2	0.92

Here, τ is the optimal laser pulse duration and r_b is radius, T_{hot} is the average hot electron energy (at the time of the Gaussian peak), η_{e-pla} is the electron beam-fuel coupling efficiency and E^{min}_{Laser} and E^{min}_{e} are the minimum ignition energy of the laser pulse and the electron beam, respectively. They were provided from simulations carried out with two values of the coupling efficiency (η=0.3 or 0.5) and two laser wavelengths (λ=1.054 and 0.527 μm).

These results also indicate that when the laser wavelength is 1.06 μm, fast ignition requires ignition pulse with energy well over 100 kJ. It is consistent with the calculation result by Atzeni *et al.*.

Figure 1-7 shows snap shots of the plasma density and ion temperature for this simulation at two moments of time: at the end of the laser pulse and at the developed burn stage. i.e., the left side of the figure shows the heating by the electron beam and the right side shows the heating by the α-particles generated by the fusion reaction.

Fig.1-7(b) shows that the plasma heating by the electron beam is not locally but occurs over the entire core. Electron beam is not completely stopped in the core and continues to heat the low-density plasma behind the core. The laser intensity at the time of the Gaussian peak is 6.5×10^{20} W/cm^2 and very energetic electrons are produced with the average energy of 7.7 MeV. The range of these electrons is longer ($\approx$ 4.62 g/cm^2) than the areal density of the fuel ($\approx$ 1.2 g/cm^2 if average density is 450 g/cm^3 and radius of fuel is 25 μm), and only 69% of the total electron energy is deposited in the plasma. Ignition is triggered first in the plasma column heated by the electrons and the burn region then expands radially Figs. 1-7(c) and 1-7(d)).

1.4.4 | Outline of the Dissertation

The heating laser energy converts into energy of relativistic electrons by laser plasma interaction and these electrons propagate to the fuel core and deliver their energy to a hot spot. Thus a quantitative understanding of the average energy and energy conversion efficiency, and how it responds to varied laser parameters is paramount for fast ignition. In order to determine the laser intensity of an appropriate heating laser, the dependence of the average energy of the relativistic electrons on

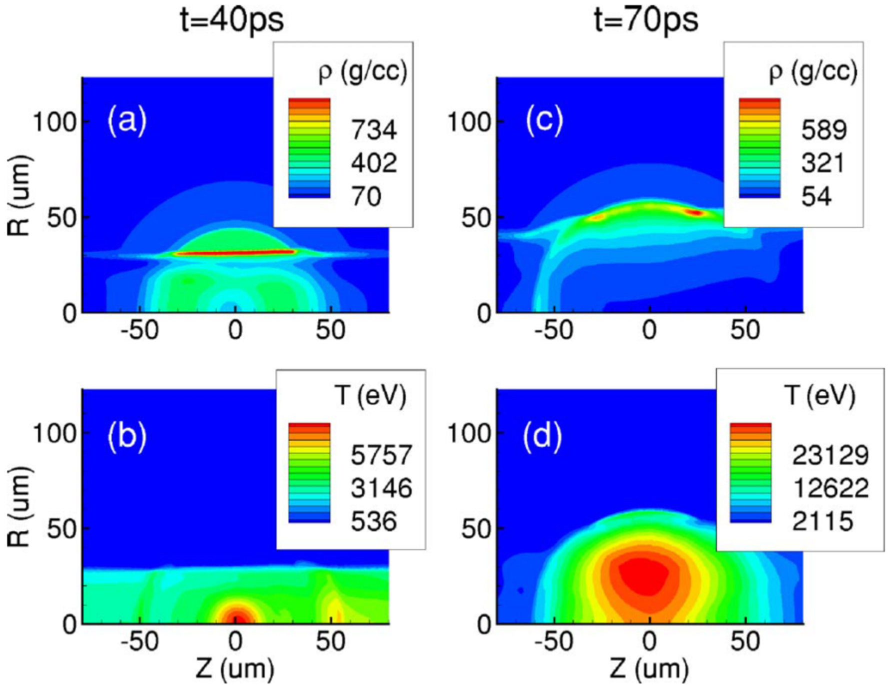

Figure 1-7: Contour plots of the density and ion temperature at selected moments of time in the burn simulation induced by a 235 kJ, 26.3 μm, 16.3 ps laser pulse with the energy conversion efficiency to fast electrons η=0.3. Figure taken from S. Atzeni and A. S. Bellei *et al.*, *Targets for direct-drive fast ignition at total laser energy of 200-400 kJ* (2007).

the laser intensity was studied, and the widely used Ponderomotive scaling law etc. were derived. However, as a result of the large time scale simulation carried out in recent years, the dependence of the average energy of relativistic electrons on the pulse duration of the heating laser, which was not considered in the above scaling lows, was revealed. Experimental verification is indispensable because the dependence of the average energy of relativistic electrons on laser pulse duration is a crucial problem on the determination of the parameters of the heating laser suitable for fast ignition laser fusion. For the first time, this study has experimentally demonstrated the effect of the pulse duration of the heating laser on the average energy of relativistic electrons and the energy conversion efficiency.

Chapter 2 provides an introduction to basic physics of relativistic intense laser-plasma interactions and some of the absorption and acceleration mechanisms that allow energy to be transferred from the laser to the plasma.

Chapter 3 describes optimization of the laser energy fluence on the surface of the plasma mirror to realize a plasma mirror with high reflectivity, high spatial uniformity and high improved pulse contrast ratio. We implemented the optimized plasma mirror system on kJ class, picosecond laser, realized high contrast ratio of 10^{-11} at 1.3 ns before main pulse, and successfully suppressed undesirable pre-plasma formation.

Chapter 4 describes estimation of average energy and energy conversion efficiency of relativistic electrons by spectrum reconstruction of hard x ray. In this study, we converted relativistic electrons into bremsstrahlung x-rays that dose not be trapped by the field. In order to measure the energy spectrum of bremsstrahlung x ray, we developed Compton x-ray spectrometer, and it obtained higher spectral resolution than that of conventional bremsstrahlung x-ray spectrometers.

Chapter 5 describes relativistic electrons acceleration mechanism in an inherent plasma formed by the main laser pulse itself in 1-4 ps time range. We revealed that the increasing of average energy of relativistic electrons due to the long pulse irradiation causes not only to the long scale plasma generated by the main pulse itself but also to the quasi-static electric field and magnetic field spontaneously generated in the plasma. Slope temperature of relativistic electrons' average energy depends on not only laser intensity but also pulse duration because the quasi-static electric and magnetic fields develop with time.

Chapter 6 describes conclusions of this study.

CHAPTER 2

Laser-Plasma Interactions

2.1 | Interaction with Single Atoms

2.1.1 | Ionization mechanisms

When a high intensity laser is irradiated on matter, its surface is instantaneously ionized and creates plasma. The natural base line often used to define high laser intensity is the hydrogen atom. We can derive minimum laser intensity to ionize of hydrogen atom from a Bohr model. From a Bohr model, the electric field strength between electron and hydrogen atom is

$$\begin{aligned} E_a &= \frac{e}{a_B^2} \qquad \text{(cgs)} \\ &= \frac{e}{4\pi\epsilon_0 a_B^2} \qquad \text{(SI)} \\ &\simeq 5.1 \times 10^9 \ \ \mathrm{Vm^{-1}}. \end{aligned} \tag{2.1}$$

The value equals to the electric field of laser with intensity of

$$\begin{aligned} I_a &= \frac{cE_a^2}{8\pi} \qquad \text{(cgs)} \\ &= \frac{\epsilon_0 c E_a^2}{2} \qquad \text{(SI)} \\ &\simeq 3.51 \times 10^{16} \ \ \mathrm{W/cm^{-2}}, \end{aligned} \tag{2.2}$$

Here a_B is Bohr radius ($a_B = \hbar^2/me^2 = 5.3 \times 10^{-9}$ cm). The simple classic approach suggests that any material ionizes at above this intensity. However in fact ionization occurs readily at lower intensities.

There are five ionization mechanisms (**multiphoton ionization**, **above threshold ionization**, **tunneling ionization**, **barrier suppression ionization** and **impact ionization**). First four mechanisms generates some free electrons from neutral condition. Then impact ionization generates more electrons. Free electron density eventually become more than critical density that needs for reflect a laser light. The dominant ionization mechanism in each of experimental condition depends on laser intensity and wave length.

Let us consider separating-parameter γ of multiphoton ionization and tunnel ionization.

(a) *Multi-Photon Ionization*

(b) *Above Threshold Ionization*

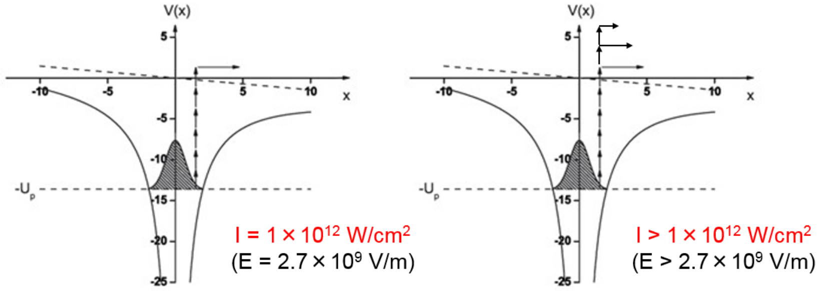

(c) *Tunneling Ionization*

(d) *Barrier Suppression Ionization*

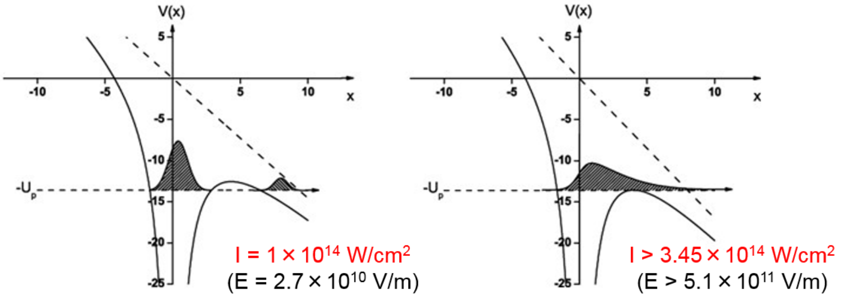

Figure 2-1: (a) Multi photon ionization, (b) Above threshold ionization, (c) Tunneling ionization, (d) Barrier suppression ionization

$$\gamma = \omega_L \sqrt{\frac{2E_{\text{ion}}}{I_L}} \sim \sqrt{\frac{E_{\text{ion}}}{\Phi_{\text{pond}}}} \tag{2.3}$$

where

$$\Phi_{\text{pond}} = \frac{e^2 E_L^2}{4m\omega_L^2} \tag{2.4}$$

is the so-called ponderomotive potential of the laser field, expressing the effective quiver energy acquired by an oscillating electron. And where E_{ion} is the ionization energy. For the case of strong fields and long wavelength, i.e. for $\gamma < 1$, tunneling ionization become dominant. For $\gamma > 1$, multiphoton ionization occurs.

2.2 | Interaction with Single Electrons

2.2.1 | Motion of a single electron in an infinite plane wave

In this section, we starts with a relatively simple description of the motion of a single electron subjected to an infinite plane wave. The motion of a single electron with charge e and mass m in the $\boldsymbol{E}$ and $\boldsymbol{B}$ of the laser field, is described by,

$$\frac{d\boldsymbol{P}}{dt} = -e\left(\boldsymbol{E} + \frac{\boldsymbol{v}}{c} \times \boldsymbol{B}\right), \tag{2.5}$$

where $\boldsymbol{p} = \gamma m \boldsymbol{v}$ is the electron momentum, $\gamma = \sqrt{1 + (|\boldsymbol{P}|/mc)^2} = 1/\sqrt{1-\beta^2}$ is the Lorentz factor and $\beta = v/c$ is the electron velocity in units of the speed of light. As first, we starts with a relatively simple description of the motion of a single electron subjected to an infinite plane wave of linearly polarized laser. For a plane wave in vacuum, $|\boldsymbol{B}| = \frac{1}{c}|\boldsymbol{E}|$ and two regimes of interaction can be directly identified from Eq.(2.5). In the non-relativistic case (i.e., $v \ll c$), electric field component of the laser dominantly acts on the electron and the electron oscillates only along the polarization direction.

The equation of motion of electrons along transverse direction is given by

$$\begin{aligned} m\frac{d^2\boldsymbol{x}}{dt^2} &= -e\boldsymbol{E}_0\cos(\omega_0 t), \\ \frac{d\boldsymbol{x}}{dt} &= -\frac{e\boldsymbol{E}_0}{m\omega_0}\sin(\omega_0 t), \\ \boldsymbol{x} &= -\frac{\nu_{os}}{\omega_0}\cos(\omega_0 t). \end{aligned} \tag{2.6}$$

The equation of motion of electrons along forward direction is given by

$$\begin{aligned} m\frac{d^2\boldsymbol{z}}{dt^2} &= -ev_x\boldsymbol{B}_0\cos(\omega_0 t), \\ &= -\frac{e\nu_{os}}{c}\boldsymbol{E}_0\sin(\omega_0 t)\cos(\omega_0 t), \\ &= -\frac{e\nu_{os}}{c}\boldsymbol{E}_0\frac{1}{2}\sin(2\omega_0 t), \\ \frac{d\boldsymbol{z}}{dt} &= -\frac{\nu_{os}}{c}\frac{e\boldsymbol{E}_0}{m\omega_0}\frac{1}{4}\cos(2\omega_0 t), \\ \boldsymbol{z} &= -\frac{1}{8}\frac{\nu_{os}}{c}\frac{\nu_{os}}{\omega}\sin(2\omega_0 t). \end{aligned} \tag{2.7}$$

The laser propagates along z and has a linear polarization along x. The transverse momentum p_x oscillates with the frequency of the laser field whereas the forward directed momentum p_z oscillates with twice laser frequency.

However, if the oscillation speed of electrons approaches the speed of light by the action of a strong electric field, we must consider the contribution to the motion of the electron by the magnetic field component. In the relativistic case (i.e., $v \approx c$), the magnetic component of the Lorentz force become very important. The main effect of the $\boldsymbol{v} \times \boldsymbol{B}$ force is to push the particle forward and electrons are accelerated by laser field along the Poynting vector of the laser field.

Figure 2-2 shows the results of numerical calculation of motion of single electron in a plane wave. Here the electron, initially at rest, is subjected to a linearly polarized laser pulse with a peak intensity of 3.5×10^{19} W/cm^2 ($a_0 = 5$). The laser propagates along z and has a linear polarization along x. The transverse momentum p_x oscillates with the frequency of the laser field whereas the forward directed momentum p_z oscillates with twice laser frequency. During each oscillation the electron is pushed forward, while it remains at rest after the laser pulse has passed. The net effect is therefore just a forward translation. We should note that the electron does not gain energy from the laser field. When an electron is injected into different initial phase ϕ_0 of laser, the motion is strongly dependent on the initial phase. Moreover the initial phase crucially governs the maximal energy achieved in the field $\gamma_{max} = 1 + \frac{a_0^2}{2}(1 + \sin\phi_0)^2$.

2.2.2 | Pondermotive force

In most experimental situations, the laser field is not an infinite wave described in the previous section, but a tightly focused laser pulse. A tightly focused laser pulse has strong photon pressure intensity gradients and it acts to push electrons away from the regions of high laser intensity. The ponderomotive force can thus be expressed as the gradient of the energy of oscillation in the longitudinal and transverse fields. In the limit $v/c \ll 1$, a single electron oscillates near the center $\boldsymbol{r}$ of a

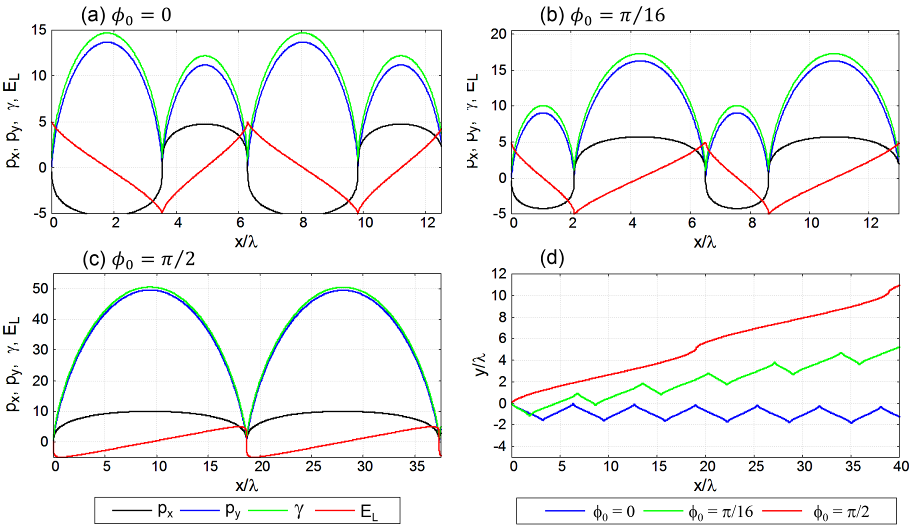

Figure 2-2: Single electron motion in a linear polarized laser. Depending on the injection phase ϕ_0, the electron is accelerated within one quarter ($\phi_0 = 0$) to one half cycle ($\phi_0 = \pi/2$) of driving filed.

focused beam and then the electron equation of motion is given by

$$\frac{d\boldsymbol{P}}{dt} = -e\left(\boldsymbol{E}(\boldsymbol{r}) + \frac{\boldsymbol{v}}{c} \times \boldsymbol{B}(\boldsymbol{r})\right), \tag{2.8}$$

Assume the wave has an electric field of the form $\boldsymbol{E} = \boldsymbol{E}_0(\boldsymbol{r})\cos(\omega_0 t)$, where $\boldsymbol{E}_0(\boldsymbol{r})$ is spatial distribution of electric field. Here, we assume that the electron velocity can be described as a sum of first and second order terms, $\boldsymbol{v} = \boldsymbol{v}1 + \boldsymbol{v}2$.

We start in first order of motion at the initial position $\boldsymbol{r}_0$, the $\boldsymbol{v} \times \boldsymbol{B}$ can be neglected, and

$$\begin{aligned} m\frac{d\boldsymbol{v}_1}{dt} &= -e\boldsymbol{E}(\boldsymbol{r}_0), \\ \boldsymbol{v}_1 &= -\frac{e}{m\omega_0}\boldsymbol{E}_0(\boldsymbol{r}_0)\sin(\omega_0 t), \\ \boldsymbol{r}_1 &= \frac{e}{m\omega_0^2}\boldsymbol{E}_0(\boldsymbol{r}_0)\cos(\omega_0 t). \end{aligned} \tag{2.9}$$

Moving onto second order of motion, Taylor expansion of the electric field around the initial position of the electrons gives

$$\boldsymbol{E}(\boldsymbol{r}) = \boldsymbol{E}(\boldsymbol{r}_0) + (\boldsymbol{r}_1 \cdot \nabla)\boldsymbol{E}|_{r=r_0} + \cdots , \tag{2.10}$$

and the motion of the electrons in second order is

$$m\frac{d\boldsymbol{v}_2}{dt} = -e\left[(\boldsymbol{r}_1 \cdot \nabla)\boldsymbol{E} + \frac{\boldsymbol{v}_1 \times \boldsymbol{B}_1}{c}\right], \tag{2.11}$$

$\boldsymbol{B}_1$ is given by Integrating Faraday's law, $\partial\boldsymbol{B}/\partial t = -c(\nabla \times \boldsymbol{E})$, it is written as c

$$\boldsymbol{B}(\boldsymbol{r}) = -\frac{c}{\omega_0}\nabla \times \boldsymbol{E}_0|_{r=r_0}\sin(\omega_0 t). \tag{2.12}$$

Substituting above expressions for $\boldsymbol{v}_1$, $\boldsymbol{B}_1$, and $\boldsymbol{r}_1$ into Eq.(2.11) and averaging over the laser period, gives

$$
\begin{aligned}
\boldsymbol{F}_P = m\left\langle\frac{d\boldsymbol{v}_2}{dt}\right\rangle &= -\frac{1}{2}\frac{e^2}{m\omega_0^2}[(\boldsymbol{E}_0\cdot\nabla)\boldsymbol{E}_0 + \boldsymbol{E}_0\times(\nabla\times\boldsymbol{E}_0)],\\
&= -\frac{1}{2}\frac{e^2}{m\omega_0^2}\nabla < \boldsymbol{E}_0^2(\boldsymbol{r}) >,\\
&= \frac{e^2}{4m\omega_0^2}\nabla\boldsymbol{E}_0^2.
\end{aligned}
\tag{2.13}
$$

This is the nonlinear ponderomotive force. The ponderomotive force sometimes be written as a force per unit volume by multiplying by the electron density n_0 and it is written as

$$
\begin{aligned}
\boldsymbol{F}_{P,vol} &= -\frac{\epsilon_0}{2}\frac{\omega_p^2}{\omega_0}\nabla < \boldsymbol{E}^2 >,\\
&= -\frac{\epsilon_0}{2}\frac{n_0}{n_c}\nabla < \boldsymbol{E}^2 >,
\end{aligned}
\tag{2.14}
$$

The ponderomotive force is proportional to the plasma density n_0 and the gradient of the laser intensity ($\boldsymbol{I} \propto \boldsymbol{E}^2$)

In the limit $v/c \approx 1$, the oscillation of a single electron can no longer be approximated as being close to the center of the focused beam, and the equation of motion can be described as

$$
\frac{d\boldsymbol{p}}{dt} + \boldsymbol{v}\cdot\nabla\boldsymbol{p} = -e\left[\boldsymbol{E} + \frac{\boldsymbol{v}\times\boldsymbol{B}}{c}\right].
\tag{2.15}
$$

The field components can be replaced by their vector potential definitions (i.e., $\boldsymbol{E} = -1/c(\partial\boldsymbol{A}/\partial t) - \nabla\phi$ and $\boldsymbol{B} = \nabla\times\boldsymbol{A}$). Additionally, substituting the momentum vector for the velocity (i.e., $\boldsymbol{v} = \boldsymbol{p}/\gamma m$) we obtain

$$
\frac{d\boldsymbol{p}}{dt} + \frac{\boldsymbol{p}\cdot\nabla\boldsymbol{p}}{\gamma m} = -e\left[-\frac{1}{c}\frac{\partial\boldsymbol{A}}{\partial t} - \nabla\phi + \frac{\boldsymbol{p}\times\nabla\times\boldsymbol{A}}{\gamma mc}\right].
\tag{2.16}
$$

The laser propagates along z and has a linear polarization along x. The momentum can be decomposed into a transverse $\boldsymbol{p}_t$and a longitudinal $\boldsymbol{p}_z$ component. $\boldsymbol{A}$ is defined to have only a transverse component and vary only in the z direction. The transverse components of Eq.(2.16) decompose into

$$
\frac{\partial}{\partial t}\left(\boldsymbol{p_t} - \frac{e}{c}\boldsymbol{A}\right) + \frac{p_z}{\gamma m}\frac{\partial}{\partial z}\left(\boldsymbol{p_t} - \frac{e}{c}\boldsymbol{A}\right) = 0,
\tag{2.17}
$$

thus, the transverse momentum is

$$
\boldsymbol{p_t} = \frac{e}{c}\boldsymbol{A}.
\tag{2.18}
$$

Furthermore, the longitudinal components of Eq.(2.16) decompose into

$$
\frac{\partial\boldsymbol{p}_z}{\partial t} + \frac{\boldsymbol{p}\cdot\nabla\boldsymbol{p}}{\gamma m} = -e\left[-\nabla\phi + \frac{\boldsymbol{p}\times\nabla\times\boldsymbol{A}}{\gamma mc}\right].
\tag{2.19}
$$

Taking the curl of Eq.(2.18), and adding the curl of the longitudinal component, the curl of vector potential $\nabla\times\boldsymbol{A}$ can be substituted into Eq.(2.20). Additionally, since $\boldsymbol{p} = \gamma m\boldsymbol{v}$, γ is written as $\gamma = \sqrt{1 + \frac{p^2}{m^2c^2}}$. Equation (2.20) can be rewritten as,

$$
\frac{\partial\boldsymbol{p}_z}{\partial t} + \frac{\boldsymbol{p}\cdot\nabla\boldsymbol{p}}{m\sqrt{1+\frac{p^2}{m^2c^2}}} = -e\left[\nabla\phi + \frac{\boldsymbol{p}\times\nabla\times\boldsymbol{p}}{m\sqrt{1+\frac{p^2}{m^2c^2}}}\right].
\tag{2.20}
$$

The vector identity $\nabla(\boldsymbol{A}\cdot\boldsymbol{B}) = \boldsymbol{A}\times(\nabla\times\boldsymbol{B}) + \boldsymbol{B}\times(\nabla\times\boldsymbol{A}) + (\boldsymbol{A}\cdot\nabla)\boldsymbol{B} + (\boldsymbol{B}\cdot\nabla)\boldsymbol{A}$, can be transformed into

$$\frac{\boldsymbol{A}\cdot\nabla\boldsymbol{A}}{\sqrt{1+\boldsymbol{A}^2}}+\frac{\boldsymbol{A}\times\nabla\times\boldsymbol{A}}{\sqrt{1+\boldsymbol{A}^2}}=\nabla\sqrt{1+\boldsymbol{A}^2}. \tag{2.21}$$

Using above transformation, the longitudinal component of equation of motion can be written as

$$\frac{\partial\boldsymbol{p}_z}{\partial t}=e\nabla\phi-m_0c^2\nabla(\gamma-1). \tag{2.22}$$

This is the ponderomotive force in the relativistic regime. The term in the gradient, along with the m_0c^2 coefficient, is called the ponderomotive potential U_p and it is given by

$$U_p=m_0c^2(\gamma-1)=m_0c^2\left(\sqrt{1+\frac{I\lambda_{\mu m}^2}{1.37\times10^{18}}}-1\right). \tag{2.23}$$

for linear polarized laser.

2.3 | Laser propagation in a plasma medium

In this section we consider the propagation of laser in plasma. Plasma consists of electrons and ions. Electrons can freely move around ions, and in that respect they have property different from that of dielectrics. In general, the ions are stationary and serve only as a charge-neutralizing background to the electron motion. Thus, the plasma is described there as a vacuum with electromagnetic sources, given by the electric charge density ρ_e and electric current density $\boldsymbol{J}_e$.

In Gaussian units, the two Maxwell equations that include the sources are

$$\nabla\cdot\boldsymbol{E}=4\pi\rho_e,\qquad\nabla\cdot\boldsymbol{B}=\frac{1}{c}\frac{\partial\boldsymbol{E}}{\partial t}+\frac{4\pi}{c}\boldsymbol{J_e}, \tag{2.24}$$

where $\rho_e=-en_e-qn_0$, and $\boldsymbol{J}_e=-en_e\boldsymbol{v}_e$. We assume an electromagnetic field

$$\boldsymbol{E}(\boldsymbol{r},t)=\boldsymbol{E}(\boldsymbol{r})\mathrm{e}^{-i\omega t}\qquad\boldsymbol{B}(\boldsymbol{r},t)=\boldsymbol{B}(\boldsymbol{r})\mathrm{e}^{-i\omega t}. \tag{2.25}$$

The electron velocity v_e in the electric current is calculated from equation of motion. The equation of motion is written as

$$\begin{aligned}\frac{\partial\boldsymbol{p}}{\partial t}&=-e\boldsymbol{E}-m_e\nu_e\boldsymbol{v}_e,\\ \frac{\partial\boldsymbol{v}_e}{\partial t}+\nu_e\boldsymbol{v}_e&=-\frac{e}{m_e}\boldsymbol{E}(\boldsymbol{r})\mathrm{e}^{-i\omega t}.\end{aligned} \tag{2.26}$$

where ν_e is the electron collision frequency. Solving Eq.(2.26) for constant $\boldsymbol{\nu}_e$ is

$$\boldsymbol{v}_e(\boldsymbol{r},t)=\frac{-ie\boldsymbol{E(r,t)}}{m_e(\omega+i\nu_e)}. \tag{2.27}$$

Substituting this velocity into the electric current density, we get

$$\boldsymbol{J}_e(\boldsymbol{r},t)=\sigma_E\boldsymbol{E}(\boldsymbol{r},t),\qquad\sigma_E=\frac{i\omega_p^2}{4\pi(\omega+i\nu_e)} \tag{2.28}$$

where σ_E is defined as electric conductivity and ω_p is plasma frequency.

Substituting $\boldsymbol{J}_e$ and using $\partial/\partial t=i\omega$ into the second Eq.(2.24), we gets

$$\nabla \cdot (\epsilon \boldsymbol{E}) = 0, \qquad \nabla \cdot \boldsymbol{B} = \frac{1}{c}\frac{\partial(\epsilon \boldsymbol{E})}{\partial t}, \tag{2.29}$$

if the dielectric function of the plasma medium is defined by

$$\varepsilon = 1 - \frac{\omega_p^2}{\omega(\omega + i\nu_{ei})} = 1 + \frac{i4\pi\sigma_E}{\omega} \tag{2.30}$$

where ω_p is the plasma frequency and ν_{ei} is the electron-ion collision frequency. In generally the plasma frequency includes two components of high frequency electron oscillations and low frequency ion oscillations. Under high frequency condition, the ion that has large mass, can not response and the contribution of ion oscillation is negligible. Plasma frequency can be defined as only the electron component.

Plasma frequency is given from the dispersion relation of an laser field, that propagates in an unmagnetized plasma,

$$\begin{aligned} \omega^2 &= \omega_p^2 + c^2k^2, \text{or} \\ k^2 &= \frac{\omega^2}{c^2}\left(1 - \frac{\omega_p^2}{\omega^2}\right) \end{aligned} \tag{2.31}$$

where ω is the angular laser frequency and k the wave number. ω_p is the plasma frequency and written by

$$\omega_p = \sqrt{\frac{4\pi n_e e^2}{m_e}} \tag{2.32}$$

Here, n_e is the free electron density, e is the electron charge, and m_e for the electron mass. The dispersion relation of Eq.(2.43) shows that an laser field can propagate in a plasma when the laser angular frequency is larger than the plasma frequency. The relation can also give in terms of a critical electron density

$$n_c = \frac{m_e\omega^2}{4\pi e^2} \cong 1.1 \times 10^{21}\left(\frac{\lambda}{\mu\text{m}}\right)\text{cm}^{-3} \tag{2.33}$$

For laser wave with wavelength 1053 nm (LFEX laser) the critical density is about 1.1×10^{21} cm^3. At the point where local free electron density equals to n_c, a laser field cannot propagate toward higher density plasma. When a laser field propagates through plasma with incident angle θ with respect to the plasma density gradient, this wave can penetrate up to the point where the dielectric constant ε equals to $\sin^2\theta$. In over density plasma, the intensity of transmitted field is exponentially decreased and it vanishes on a distance of the order of skin depth l_s. It is defined as

$$l_s = \frac{c}{\sqrt{\omega^2 - \omega_p^2}} \approx \frac{c}{\omega_p} \tag{2.34}$$

2.4 | Laser absorption and charged particle acceleration

The energy transfer from the laser to the plasma depends on the density profile of pre-formed plasma, the incident angle of the laser, the laser intensity, laser wavelength, polarization and the pulse length. Different absorption mechanisms apply in dependence on those laser and target parameters. In general, absorbed laser energy is spend to plasma heating and ionization or to accelerate charged particles.

The main laser absorption processes that has been reported, are collisional absorption (inverse bremsstrahlung), normal skin effect, anomalous skin effect, sheath inverse bremsstrahlung, sheath transit absorption, vacuum (Brunel) heating, resonance absorption, ponderomotive acceleration, stochastic heating and parametric instabilities.

These absorption processes can be divided into two groups. The first group increase kinetic energy of the bulk electrons of the interaction region. As the result of these processes, plasma temperature is increased. This group is categorized as heating processes. The second group accelerates some of free electrons included in plasma up to high speed. This group is categorized as acceleration processes.

List of the main absorption processes is presented in Table 2.1 together with these category, the conditions for high efficiency, and reference.

Table 2.1: Laser absorption and charged particle acceleration

Absorption mechanism	Category	Type of process	Conditions for high efficiency	Reference
Inverse bremsstrahlung	Heating	collisional linear	$L \geq \lambda$ $\lambda_{mfp}(= v_t/\nu_{ei}) < l_s$	[12] [13] [14]
Normal skin effect	Heating	collisional linear	$L \to 0$ $\lambda_{mfp} < l_s$	[15]
Anomalous effect	Heating	collisionless linear	$\lambda_{mfp} > l_s, v_{osc} < v_t,$ $\theta = 0°, v_t/\omega > l_s$	[16]
Sheath inverse bremsstrahlung	Heating	collisionless linear	$\lambda_{mfp} > l_s, v_{osc} < v_t,$ $\theta = 0°, v_t/\omega < l_s$	[17]
Sheath transit absorption	Heating	collisionless linear	$\lambda_{mfp} > l_s, v_{osc} < v_t,$ $\theta > 0°$	[18]
Vacuum heating	Acceleration	collisionless nonlinear	$L < v_{osc}/\omega, v_{osc} > v_t,$ $\theta > 0°$ (P-polar.)	[19]
Resonance absorption	Acceleration	collisionless linear	$\omega L/c \sim \sin\theta$ $\theta > 0°$ (P-polar.)	[14] [20] [21]
Ponderomotive acceleration	Acceleration	collisionless nonlinear	$a_0 > 1$ linear polarization	[22] [23] [24]
Stochastic heating	Acceleration	collisionless nonlinear	$a_1 \times a_2 > 1$ (Colliding wave)	[25] [26]
Parametric instabilities	Acceleration	collisionless nonlinear	$\Gamma(a_0, \omega_p) \leq \tau$ $L \ll \omega$	[27] [20] [28] [20]

2.4.1 | Inverse Bremsstrahlung (Collisional Absorption)

In vacuum, free electrons do not gain energy from the plain laser field. However, in plasma, free electrons can collide with ions. Inverse bremsstrahlung (Collisional absorption) is the process in which kinetic energy of an electron oscillating in laser field is converted thermal energy while colliding with an ion or with another electron in a plasma. The transfer of energy is caused by Joule heating (Ohmic heating). Here we consider a simple model where the ion motion and the electron thermal motion is neglected.

The absorption coefficient is

$$\alpha_{abs} = 1 - \exp\left(-\frac{8}{3}\frac{\nu_{ei}(n_c)L}{c}\right) \tag{2.35}$$

where L is the density scale length of an exponential density profile and $\nu_e i(n_c)$ is the electron-ion collision frequency evaluated at the critical density n_c. The collisional frequency depends on T_e , n_i and Z_i and it is written by

$$\nu_{ei} = \frac{4}{3}\frac{(2\pi)^{1/2} Z_i^2 e^4 n_i \ln\Lambda}{(k_B T_e)^{3/2} m_e^{1/2}} \simeq 2.9 \times 10^{-6} \frac{Z_i^2 n_i \ln\Lambda}{T_e^{3/2}\ [\mathrm{eV}]} \quad [1/\mathrm{s}] \tag{2.36}$$

where $\Lambda = b_{max}/b_{min}$, and the factor $\ln\Lambda$ is called the Coulomb logarithm. For low-density plasmas and moderate laser intensities Coulomb logarithm typically lies in the range of 10-20.

The fast electron slope temperature given by inverse bremsstrahlung, scales as

$$T_e \sim 8(I_{16}\lambda^2_{\mu m}) \quad [\mathrm{keV}] \tag{2.37}$$

where I_{16} is the laser intensity in 10^{16} W/cm^2 and λ is the laser wavelength in μm. At higher laser intensities ($> 10^{16}$ W/cm^2) with higher electron temperature ($\sim$ 2 keV), as the collision frequency $\nu_{ei} \propto T_e^{-3/2}$, inverse bremsstrahlung becomes relatively less efficient and other absorption processes become more dominant.

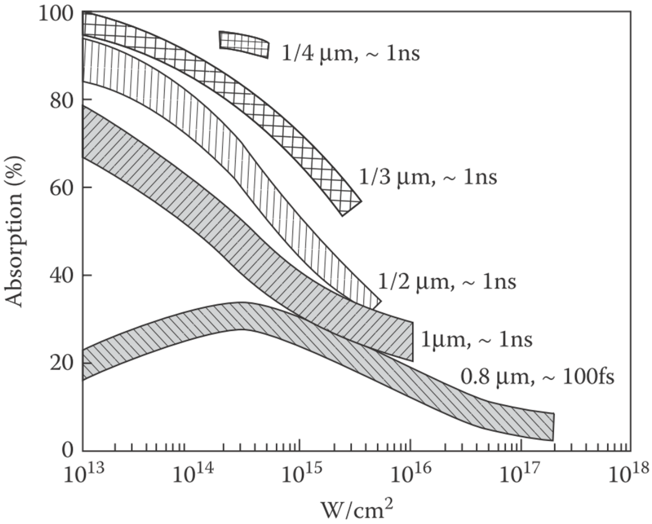

Figure 2-3: Experimental data of the laser absorption by collisional absorption in solid low-Z targets. Figure taken from Eliezer, *An introduction to internal confinement fusion* (2002).

2.4.2 | Normal Skin Effect

Normal skin effect is a special case of collisional absorption that occurs in plasma with very steep density profile ($L \to 0$). In the such very steep density profile plasma, the laser field penetrates into overdense plasma region. Intensity of transmitted field is exponentially decreased and it vanishes on a distance of the order of skin depth. In the case that the eld intensity in the skin layer is lower and the electron density is very high, electron-ion collision frequency is high. Therefore inverse bremsstrahlung in the skin layer become relatively efficient again.

2.4.3 | Resonance Absorption

When a laser is obliquely incident at incidence angle θ into expanding plasma with p-polarization, resonance absorption occurs. The laser field penetrates up to a turning point at density $n_c \cos^2 \theta$. The tunneling electric field accelerates electrons parallel to the density gradient. At $n_e = n_c$, electrons bunch are excited to oscillate resonantly with the p-polarized electric field and generates an electrostatic plasma wave (a Langmuir wave).

The electrostatic plasma wave dissipates its energy by collisions in lower laser intensities and heats plasma. In collision less plasma, its energy is dissipated by particle trapping and wave breaking. Therefore, laser energy absorbs by resonance absorption process even in the collisionless plasma. Resonance absorption appears only for p-polarization. The s-polarized laser can not generate an electrostatic plasma wave, because the field is perpendicular to the density gradient.

A further characteristic of resonant absorption is the generation of fast electrons. In resonance absorption, only a small part of electrons trapped by plasma wave absorb a large amount of energy and is accelerated to high velocity compared with thermal velocity.

Efficiency of resonance absorption depends on scale length of plasma L and incident angle of laser θ. According to theoretical and numerical studies, the maximum efficiency is achieved when the following relation is fulfilled

$$(kL)^{1/3} \sin\theta \sim 0.8, \tag{2.38}$$

where k is the laser wave number. More than 50% of the laser energy can be absorbed by fast electrons due to resonance absorption at the optimum condition.

The fast electron slope temperature given by resonance absorption, scales as

$$Te \sim 10(T_{keV} I_{15} \lambda_{\mu m}^2)^{1/3} \quad \text{[keV]} \tag{2.39}$$

where the T_{keV} is the background electron temperature in keV, I_{15} is the laser intensity in 10^{15} W/cm^2 and λ is the laser wavelength in μm.

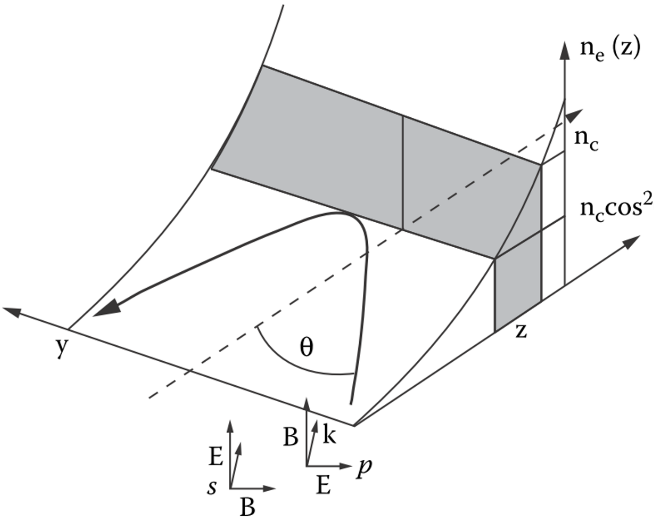

Figure 2-4: Schematic picture of p-polarization for resonance absorption. Figure taken from Eliezer, *An introduction to internal confinement fusion* (2002).

2.4.4 | Vacuum heating (Brunel absorption)

For very sharp density gradients (the amplitude of the resonantly oscillating electrons exceeds the scale length), resonant absorption becomes inefficient and vacuum heating becomes dominate. An electron at the boundary layer between plasma and vacuum is rapidly accelerated into the vacuum during half cycle of oscillation of the laser field. Then, in next half cycle of oscillation, the electron is accelerated back into the plasma. If the typical oscillation displacement of the electrons is greater than the scale length of the plasma, the electron is screened from the electric field and does not feel the restoring force that accelerates the electron into vacuum. The electron propagates beyond the skin depth and dissipates its energy via collisions.

2.4.5 | Parametric instability

When laser intensity becomes high, plasma interacts with laser field nonlinearly and lead to parametric instabilities. A parametric instability is nonlinear phenomenon where a periodic variation in the plasma is grown oscillations at a different frequency. In plasma, the nonlinear effects are caused by such terms as $\boldsymbol{v} \times \boldsymbol{B}, \nabla \boldsymbol{v}, \nabla \cdot (n\boldsymbol{v})$, ponderomotive forces, changes of mass due to relativistic velocities, velocity-dependent collision frequency, etc. These terms can cause a large amplitude wave, which provides the driving force to excite other wave. Main parametric instabilities in ICF research, is the resonant decay of the incident wave into two new waves. Although there also exist processes involving four or more waves, these do not play significant role. In the absence of magnetic field, three modes of waves are possible to generate in plasma (an electromagnetic wave, an electron plasma wave and an acoustic ion plasma wave). Main processes of parametric instability related to ICF research is following.

Parametric decay instability **(TDI)** : EM wave → ion wave + electron wave
Two-plasmon decay instability **(TPD)** : EM wave → electron + electron wave
Stimulated Brillouin scattering **(SBS)** : EM wave → EM wave + ion wave
Stimulated Raman scattering **(SRS)** : EM wave → EM wave + electron wave

EM wave means electromagnetic wave. Electron wave and ion wave are known as plasmon or Langmuir wave and acoustic wave, respectively.

2.5 | Characteristics of the relativistic electrons

2.5.1 | Electron temperature scaling

The random electron acceleration in the laser field results in fluctuations in their trajectories and their gained energies. The energy distribution of accelerated electrons often follows the Maxwellian distribution, and gradient temperature of Maxwell distribution is often used for a parameter showing characteristics of the electrons. A single temperature Maxwellian distribution can be defined as a function of kinetic energy, E , as;

$$f(E) = N_0 \sqrt{\frac{4E}{\pi (k_B T_e)^3}} \exp\left(-\frac{E}{k_B T_e}\right) \tag{2.40}$$

where N_0 is the total number of electrons and $k_B T_e$ is the slope temperature of electrons.

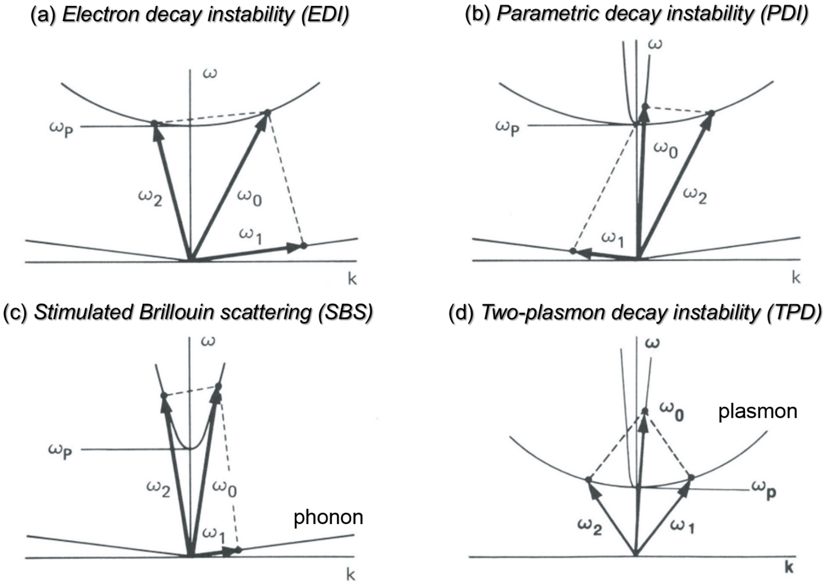

Figure 2-5: Parallelogram constructions showing the simultaneous matching of frequency and wavenumber for (A) electron decay instability, (B) parametric decay instability, (C) stimulated Brillouin backscattering instability, and (D) two-plasmon decay instability.

The slope temperature of electrons depends on the laser intensity and the scaling law of the slope temperature of electrons with respect to laser intensity has been discussed in various papers. These scaling law are summarized in Table 2.2.

Table 2.2: Summary of scaling laws of slope temperature of electrons with respect to laser intensity

Scaling	Type	$I_0\lambda_0^2$	L/λ_0	θ	k_BT_e (keV)
Resonance	Simulation	$< 10^{17}$	> 1	$\sin^{-1}(c/2\omega L)^{1/3}$	$14(k_BT_eI_{16}\lambda_{\mu m}^2)^{1/3}$
Brunel	Theory	$> 10^{17}$	< 1	73°	$3.7(I_{16}\lambda_{\mu m}^2)$
Gibbon	Simulation	$< 10^{17}$	≤ 0.1	45°	$7(I_{16}\lambda_{\mu m}^2)^{1/3}$
Beg	Experiment	$< 10^{19}$	> 1	30°	$100(I\lambda_{\mu m}^2/10^{17})^{1/3}$
Haines	Theory	$> 10^{18}$	-	-	$511[(1+(I_{18}\lambda_{\mu m}^2)^{1/2})^{1/2}-1]$
Wilks	Simulation	$> 10^{18}$	~ 1	0°	$511[(1+0.73I_{18}\lambda_{\mu m}^2)^{1/2}-1]$

Previous measurements of the electron energy distribution relied on several techniques: vacuum electron spectrometers, nuclear activation Bremsstrahlung spectrometers, buried fluorescent foils, and proton emission.

Beg et al. [29] empirically demonstrated a scaling of $100(I\lambda_{\mu m}^2/10^{17})^{1/3}$ where $\lambda_{\mu m}$ is the laser wavelength in μm and I is the laser intensity in W/cm^2. H. Chen *et al.* [30] and Tanimoto *et al.* [31] also reported similar scaling. This scaling applies for laser intensities up to 10^{19} W/cm^2, and electron acceleration mechanism of this scaling is attributed to resonance or vacuum heating. Haines *et al.* [32] found a scaling that is described relativistic analytic model based on energy and momentum conservation laws for the laser interaction with an overdense plasma. It provides a small relativistic correction to the Beg scaling for cases of when the precursor plasma density profile is swept up, and therefore steepened by the main laser pulse.

At higher laser intensities ($> 10^{19}$), $\boldsymbol{j} \times \boldsymbol{B}$ force dominates acceleration mechanism of electrons and it gives ponderomotive scaling. S. C. Wilks *et al.* [8] firstly reported a simulated result of electron acceleration by a high intense laser with an intensity greater than 10^{19} W/cm^2. This scaling was experimentally confirmed by G. Malka *et al.* [33].

Furthermore, the slope temperature of electrons is also affected by the density profile of the plasma on which the laser is incident. If scale length of the plasma is longer than the skin depth ($L \gg c/\omega_{pe}$), the skin depth is longer than the electron excursion length. The electron can be "fully" accelerated by the laser field during the interaction. If scale length of the plasma is shorter than the skin depth ($L \ll c/\omega_{pe}$), however, the electrons do not have the distance to fully accelerate by the laser field during the interaction. This effect leads to a decrease in the slope temperature of the electrons. It has been reported that plasma with such a small density gradient is created by compression of high density plasma by the ponderomotive force of the laser. Because skin depth is inversely proportional to the density at the critical surface, the electron spectrum temperature drops by a factor of $\sqrt{\gamma n_c/n_p}$, where n_p is the electron density in the steepened plasma slab. Calculated results by detailed PIC simulation were reported by Chrisman *et al.* [34] and Kemp *et al.* [35].

2.5.2 | Energy conversion efficiency from laser to electrons

In previous works, energy conversion efficiencies have been estimated by experiment using typical three kinds of targets: a thin foil, buried tracer layers in a thick block and a cone wire target.

Myatt *et al.* [36] and Nilson *et al.* [37] used a very thin foil target with strong refluxing. They found $\eta_{L-Total}$ of 10-30%, independent of the laser intensity for $I = 10^{17}$-10^{20} W/cm^2 using a hybrid particle in cell model. In those experiments, Ohmic potential produced around a thin foil was enough high to refluxing electron until electrons deposit their all energy to the foil and K-shell emission was assumed to increase proportionally to $\eta_{L-Total}$.

Yasuike *et al.* [38] and Wharton *et al.* [39] used buried tracer layers with variable front layer thickness. They found $\eta_{L-Total}$ is laser intensity dependent (from 10% at 10^{18} W/cm^2 to 50% at 10^{20} W/cm^2). $\eta_{L-Total}$ was estimated by comparison of K-shell emission recorded at experiment and Monte Carlo simulation results. C.D.Chen *et al.* [40] used cubic metal block to estimate energy conversion efficiency. They found energy conversion efficiency is 20-40% ($\eta_{L-Total}$) at 10^{19} W/cm^2 and 3-12% ($\eta_{L-1-3MeV}$).

The experiment to measure conversion efficiency of cone geometry was performed by T. Ma *et al.* [41] They used a cone-wire target. They found $\eta_{L-Total}$ is 2.5-8.4% and $\eta_{L-1-3MeV}$ is 0.03-0.57% at the laser intensity $I = 10^{20}$ W/cm^2 .

2.6 | Laser Interaction with Overdense Plasmas

2.6.1 | Hole-boring

The hole-boring uses the ponderomotive pressure of the incident laser to push the critical surface. The ponderomotive pressure exceeds 1 Gbar at the laser intensity of 10^{19} W/cm^2. Here R is the reflectivity and I is the laser intensity.

The equation of momentum balance at an interaction surface, is given by

$$(1+R)\frac{I}{c} = n_e T_e + 2M_i n_i u^2 \approx 2M n_i u^2 \tag{2.41}$$

where R is the reflectivity and I is the laser intensity. Mi and ni are the ion mass and the density at the interaction surface. Neglecting the electron temperature, the hole-boring velocity is obtained by [8]

$$\frac{u}{c} = \sqrt{\frac{n_c}{2n_e}\frac{Zm_e}{M_i}\frac{I\lambda^2}{1.37 \times 10^{18}}} \tag{2.42}$$

According to Eq.(2.42), if the intensity is 10^{19} W/cm^2, the ponderomotive pressure accelerates a plasma of critical density (10^{21} cm^{-3}) to 2×10^9 cm/s. Since the energy loss of the laser was neglected in the Eq.(2.42), the pushing speed is higher than the realistic speed.

2.6.2 | Relativistic transparency

Relativistic transparency [42] is an additional effect of the laser hole-boring into overdense plasma. The laser wave can propagate when the dielectric constant has the condition $\epsilon = 1 - \omega_p^2/\gamma\omega^2 > 0$. Here ω_p and ω are the plasma frequency and the laser frequency, respectively.

In the relativistic regime, electron quiver velocity approaches the speed of light c. The mass of accelerated changes by the relativistic effect and increases by γ factor. This effect decreases the plasma frequency $\omega_p = \sqrt{4\pi e^2 n_e/\gamma m_e}$. Moreover, this effect shifts the critical density to γn_c.

For a laser wave (k, ω), the plasma dispersion relation is described by

$$k^2c^2 = \omega^2 - \omega_p^2/c, \tag{2.43}$$

and the relativistic group velocity in the plasma is given by

$$v_g = \frac{\partial \omega}{\partial k} = c\sqrt{1 - \frac{n_e}{\gamma n_c}} \tag{2.44}$$

This modification is correct at least when the plasma density n_e is less than n_c, and energy loss of the laser can ignore. When $n_e > n_c$, the energy loss of the laser can not ignore, thus the effective group velocity will be smaller than that from Eq.(2.44).

2.7 | Spontaneous electric field and magnetic field generation

2.7.1 | Electric field in expanding plasma

When a laser irradiates a target, the electrons are heated and they expand towards the vacuum. Expanding electrons create an static electric field (Debye sheath) by charge separation which tugs on the ions. In this section the strength of static electric field is calculated, by assuming that the electrons and the ions are treated as separate fluids with different temperatures. We assume that electrons expand from the planer target one dimensionally (towards the x direction). This approximation is valid as long as a laser spot $D \gg v_i t$. Here v_i is the expanding velocity of the ions and t is the expansion time.

Electric field induced by plasma expansion is given by

$$E = -\frac{1}{n_e e}\frac{\partial P_e}{\partial x} = -\frac{k_B T_e}{n_e e}\frac{\partial n_e}{\partial x}, \tag{2.45}$$

where $P_e = n_e k_B T_e$ is the electron pressure. This field accelerates ions that is in the vicinity of the target surface. The continuity equation and the momentum equations for the accelerated ions are

$$\frac{\partial n_i}{\partial t} + \frac{\partial}{\partial x}(n_i v_i) = 0, \tag{2.46}$$

$$\frac{\partial v_i}{\partial t} + v_i \frac{\partial v_i}{\partial x} = \frac{Ze}{M} E. \tag{2.47}$$

Substituting Eq.(2.45) into Eq.(2.47) and assuming quasi-neutrality ($n_e \cong Zn_i$), Eq.(2.47) can be rewritten as

$$\frac{\partial v_i}{\partial t} + v_i \frac{\partial v_i}{\partial x} = C_s^2 \frac{1}{n_i} \frac{\partial n_i}{\partial x}, \tag{2.48}$$

where $C_s = (ZT_e/M)^{1/2}$ means ion sound velocity. This calculation is called the isothermal expansion model of plasma. And self-similar solutions are given as

$$\begin{aligned} v_i &= C_s + x/t, \\ n_i &= n_0 \exp(-x/C_s t) \end{aligned} \tag{2.49}$$

The electric field is obtained from the second equation of Eq.(2.45) by substituting Eq.(2.49), yielding

$$E = -\frac{k_B T_e}{n_e e} \frac{\partial n_e}{\partial x} = -\frac{k_B T_e}{e C_s t} \frac{n_i/n_0}{x/C_s t} = \frac{k_B T_e}{e C_s t}. \tag{2.50}$$

The electric potential induced by plasma expansion is given by

$$\phi = \int E \mathrm{d}x = -\frac{k_B T_e}{e} \frac{x}{C_s t} \tag{2.51}$$

2.7.2 | Magnetic field generation

When a high intensity laser is focused on a plasma, static magnetic field is generated, spontaneously. This static magnetic field generation has been a field of active research for last decades. Previous studies have shown that fields of the order of several megaGauss are generated during laser-plasma interaction. There are various mechanisms capable of generating magnetic fields in plasmas.

The magnetic field generated can be calculated by combining Faradays'law and the generalized Ohm's law

$$\frac{\partial \boldsymbol{B}}{\partial t} = -\nabla \times \boldsymbol{E} \tag{2.52}$$

$$\boldsymbol{E} = -\left(\boldsymbol{v} \times \boldsymbol{B} - \frac{\boldsymbol{J} \times \boldsymbol{B}}{n_e e} + \frac{\boldsymbol{q_e} \times \boldsymbol{B}}{\frac{5}{2} p_e} + \frac{\nabla P_e}{n_e e} + \beta \frac{\nabla T}{e} - \eta \boldsymbol{J} - \frac{m_e}{n_e e^2} \frac{\partial J}{\partial t} \right) \tag{2.53}$$

where v is the electron velocity, J is the plasma current density, ∇P_e is the pressure gradient. n_e is the electron density, T_e is the electron temperature, e is charge of the electron, η is plasma resistivity.

Considering only the major source terms, equation of time evolution of static magnetic field is given by,

$$\frac{\partial \boldsymbol{B}}{\partial t} = \nabla \times (\boldsymbol{v} \times \boldsymbol{B}) - \nabla \times \left(\boldsymbol{J} \times \frac{\boldsymbol{B}}{n_e e} \right) + \frac{1}{n_e e} \nabla T_e \times \nabla n_e - \nabla \times (\eta \boldsymbol{J}) \tag{2.54}$$

The above equation contains source terms (second and third), dissipative term (fourth) and convective loss term (first).

The term $\nabla T_e \times \nabla n_e$ of Eq.(2.54) represents the thermoelectric effect source term. The toroidal static magnetic fields is spontaneously generated in a under dense plasma due to non-parallel density

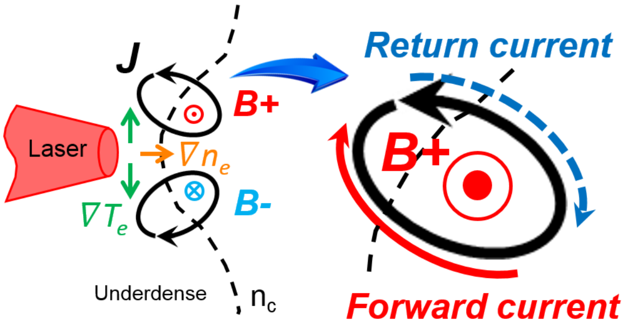

Figure 2-6: Mechanism of magnetic field generation through the $\nabla T_e \times \nabla n_e$ term in a laser-plasma interaction. An average electron current (forward current) flows along the red vector shown and return current flows along the blue vector. The current loop, originates the magnetic field in the under dense plasma.

and temperature gradients. When a laser incidents normal to target surface, the largest contribution to this term comes from a temperature gradient in the radial direction of laser axis and the density gradient due to the plasma expansion along the direction normal to the target surface. The strongest magnetic field is generated near the edge of the focal spot.

An intuitive picture of the field generation mechanism is shown schematically in Fig.2-6. Laser heated plasma expands outwardly from a target surface and sets up density gradient. The density gradient flows an electron current from the target. Since the flow velocity of plasma is greater in the hotter region, an average electron current (forward current) flows along the red vector shown in Fig.2-6. Return current flows along the blue vector shown in Fig.2-6. The current loop formed by red and blue vectors, originates the magnetic field.

CHAPTER 3

Laser intensity contrast improvement by plasma mirror

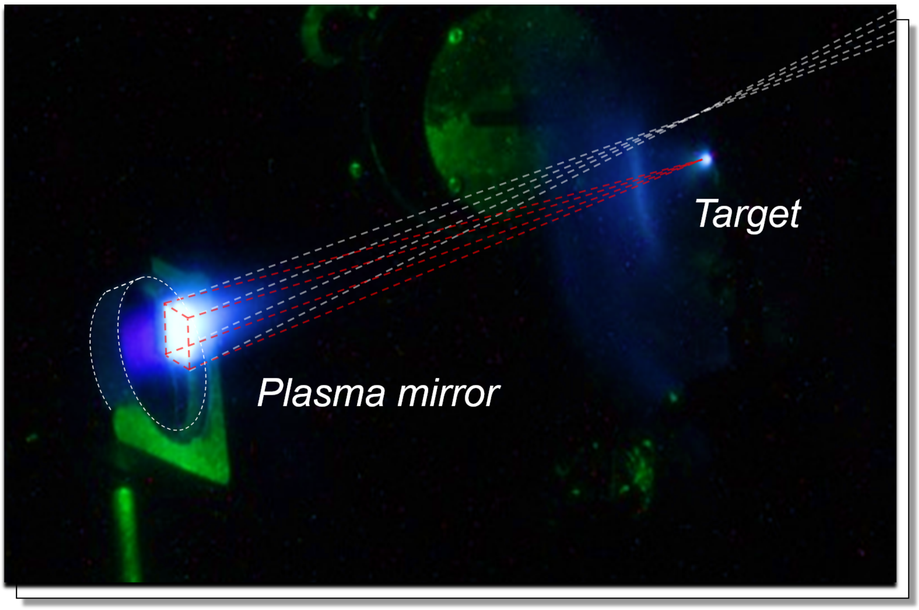

3.1 | Introduction

Using a laser with a pulse contrast ratio on the order of 10^{-9}, it is impossible to investigate only the influence of the pulse duration of the main pulse on the electron acceleration. Because the preceding pulses create a preplasma whose scale length is longer than that of a plasma generated by the main pulse. Therefore, the plasma mirror was used to improve the pulse contrast. The plasma mirror removes the preceding pulses from the low-contrast laser pulse. In Sec.3.2, the type of preceding pulses of LFEX laser is explained. In Sec.3.3, we summarizes schemes of contrast improvement. In Sec.3.4, the concept of the plasma mirror and three parameters to optimize the performance of the plasma mirror are described Section 3.5 reports the reflectivity of the plasma mirror and the spatial uniformity of the reflected pulse on different laser fluence. Section 3.6 explains focusability of spherical plasma mirror and manipulating system of plasma mirror. Section 3.7 explains the effect of laser contrast improvement by the plasma mirror. Laser pulse contrast exceeding 10^{11} was demonstrated on a kilojoule-class petawatt LFEX laser system by implementing a 2 inch plasma mirror. The laser energy fluence on the surface of the plasma mirror was optimized to realize a plasma mirror with high reflectivity, high spatial uniformity and high improved pulse contrast ratio. Laser beams of up to 1.2 kJ striking the plasma mirror with a pulse duration of 1.5 ps were reflected and focused onto a target without significant distortions in the focal spot. Transmitted light from the plasma mirror reveals that it has a high reflectivity 2 ps before the main peak. The estimated laser pulse contrast at the target was 10^{11} at 1 ns before the main peak. No preformed plasma was observed with optical interferometry diagnostics, while in the experiment without a plasma mirror a preplasma was clearly observed. This technique constitutes a promising method to enhance the LFEX laser system performance.

3.2 | Preceding pulses

The preformed plasma is formed by ablation of a material by a laser pulse proceeding prior to the main pulse (shown in Fig.3-1).[43] A typical pulse of high-intensity laser is composed of three components of preceding-pulses in addition to the main pulse. Influence of the preceding pulses on the plasma pre-formation is dependent on the its intensity and duration. Laser performance is expressed by pulse contrast ratio, which means intensity of preceding-pulse divided by the intensity of the main pulse.

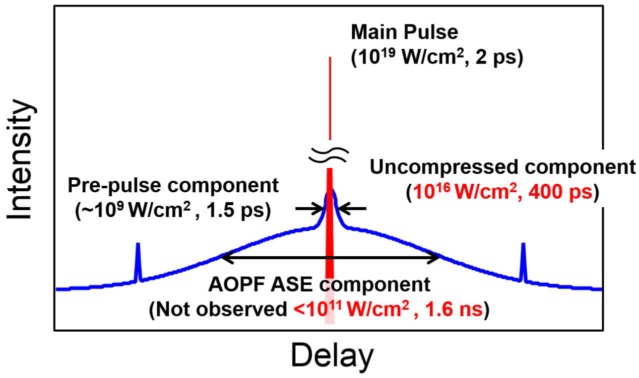

Figure 3-1: Schematic of high-power OPCPA laser pulses. The intensities and pulse durations of the components are system dependent. Figure taken from Shinji Ohira *et al.*, *JOURNAL OF APPLIED PHYSICS* (2012).

The first component of preceding-pulse is the prepulse. And it is the leakage component from pulse slicers in the oscillator stage. This pulse appears in every period of pulse trains continuously generated by the oscillator. Since the prepulse propagates along the same path of the main pulse, it has same focal spot and same pulse duration of the main pulse, except that it has a different energy. The prepulse energy in the LFEX system is designed to be less than 10^{10} that of the main pulse. We can neglect the effect of the prepulse on preformed plasma formation in this study. This component is referred to as the prepulse hereafter. The second component of preceding-pulse is the foot pulse. This component is generated by amplification of optical parametric fluorescence (AOPF) in optical parametric chirped pulse amplification (OPCPA)[44] in a front-end system. This component of the LFEX laser system is predicted to have a duration of a few nanoseconds and an intensity of 10^{10}-10^{13} W/cm^2 at the target. This component is referred to as the foot pulse hereafter. The third component is the pedestal. This component appears at the leading edge of the main pulse. This component is generated by nonlinear processes employed in the pulse stretching, amplification, and pulse compression stages of the chirped pulse amplification (CPA) system. This component is referred to as the pedestal hereafter. This component starts to appear at a few hundreds of picoseconds prior to the onset of the main pulse, and its intensity increases exponentially with time. When the intensity of the preceding pulses exceeds 10^{10} W/cm^2 at the target, a plasma forms on its surface prior to irradiation by the main pulse.[45] In this study, we focused to foot pulse and pedestal pulse that have possibly to form a long-scale preformed plasma.

3.3 | Schemes of contrast improvement

Broad studies to improve the pulse contrast have been performed within the last decades. A saturable absorber [46, 47], a cross-wave polarization technique [48], and a fluorescent quenching technique [49] are known methods to improve the laser pulse contrast before compression. However, these methods can not compensate for the laser pedestals created by imperfections in the pulse compression. Laser frequency doubling [50] is a promising method to obtain a high-contrast pulse with large throughput efficiencies of up to 75%. However, thin large-sized doubling crystals, required to avoid any wavefront distortion caused by nonlinear effects, are too expensive and fairly complex to manufacture. In particular, four crystals with the size of 40 cm×40 cm×1 mm are required for the four-beams LFEX system. The use of plasma mirrors is a promising method [51, 52, 53] because it allows one to improve the contrast of any laser pulse by a factor of ∼100, with up to 80 % throughput efficiency[51] and at a relatively low price.

3.4 | Concept of plasma mirror

Plasma mirror (PM) is a promising device for reduction of a pedestal and a foot pulse of a high intense laser. PM is a flat transparent material at initial condition, and usually, an optically flat glass is used. Firstly, a laser pulse strikes an optically flat glass, with appropriate fluence. The fluence is sufficiently low for the pedestal and the foot pulse to be transmitted through the PM. While, the fluence of main pulse is high enough to ionize the plasma mirror surface. Leading edge of main pulse generates over density plasma. And it acts as a mirror to following pulse. i.e., a PM works as an ultrafast shutter that is switched by the laser light itself (illustrated in Fig.3-2). For the optimization of the plasma mirror, the following three parameters are important.

Wave front uniformity of reflected pulse

In order for the reflecting main pulse to keep high wave front uniformity, high spatial uniformity of the over density plasma surface is required. If pulse duration of a main pulse is shorter than timescale of plasma expansion, the plasma expansion is negligibly small compared to the laser wavelength. If pulse duration of a main pulse is longer than timescale of plasma expansion, no longer, deformation of the reflecting surface can not be neglected. Time required for deformation depends on the fluence of the laser act the PM surface.

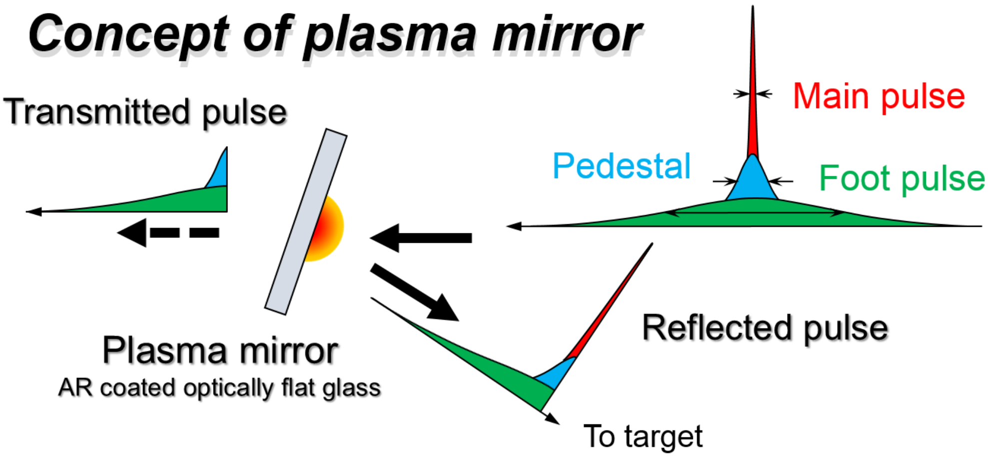

Figure 3-2: Concept of plasma mirror. Laser pulse strikes an optically flat glass with appropriate fluence. The fluence is sufficiently low for a pedestal and the a pulse to be transmitted through the glass. The fluence of main pulse is high enough to ionize. Leading edge of the main pulse generates a dense plasma. And the generated plasma acts as a mirror to a following pulse. Due these process, intensity contrast ratio between the main pulse and the pre-pulse, will improve one hundred times. And high contrast pulse is reflected to a target.

Reflectivity

Reflectivity of the PM is also depends on the fluence. When a main pulse is reflected by a PM, a part of energy is consumed to generate plasma. The generated plasma also partly absorbs energy and results in an energy loss of the reflecting main pulse. The reflectivity of the over density plasma is depended on temperature of plasma, and it implies that the high fluence is important for high reflectivity. Reflectivity is defined by the ratio of the total energy of the incident and reflected main laser pulse.

Contrast enhancement factor

The contrast enhancement factor is determined by ratio of the contrast ratio of incident and reflected light. In order to increase contrast enhancement factor, usually, an optically flat glass is coated by anti-reflected coating for laser wave length. Reflectivity of before working of a PM, is 0.5 % due to Fresnel reflection on the boundary.

3.5 | Reflectivity of the plasma mirror and spatial uniformity of reflected pulse

The laser fluence on a plasma mirror was optimized to obtain high spatial uniformity of reflected laser, and high reflectivity. Firstly, the laser pulse was focused at target chamber center (TCC) using normal off axis parabolic mirror and, defocussing pulse strikes an optically flat glass. A Teflon plastic plate (white screen) was attached on chamber wall (located at about 860 mm from TCC). The PM was an Anti-Reflected (AR) coated quartz plates to minimize Fresnel reflectivity, and to maximize contrast improvement.

PM was exposed at 45° incident angle with the S polarized laser beam (shown in Fig.3-3). The

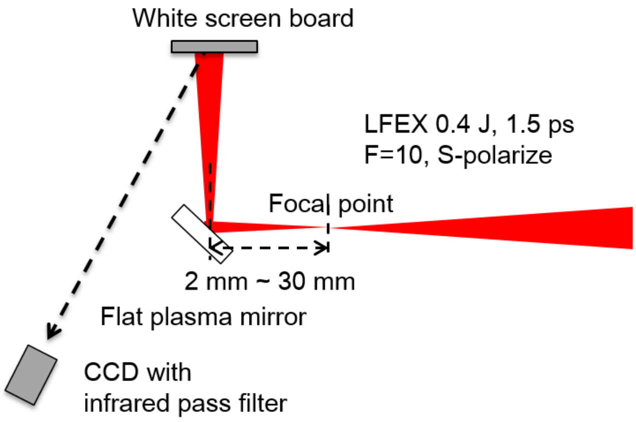

Figure 3-3: Experimental setup for the reflectivity measurement. Firstly, the laser pulse was focused at TCC using normal off axis parabolic mirror and, defocussing pulse strikes an optically flat glass. A Teflon plastic plate (white screen) was attached on chamber wall (located at about 860 mm from TCC). The spatial pattern of the reflected laser on the Teflon plastic plate was recorded by a energy calibrated CCD camera.

laser energy was fixed at 400 mJ and the laser fluence on the PM was varied by changing laser spot size (from 2 mm to 30 mm) on the PM. (Indeed, the distance between the PM and the laser focus point was adjusted.) PM was moved to provide a fresh undamaged surface for each shot.

The spatial pattern of the reflected laser on the Teflon plastic plate was imaged on a energy calibrated charge coupled device camera (CCD camera). Reflectivity was defined as ratio laser energy reflected by the plasma mirror and an dielectric multilayer mirror. The CCD camera was positioned about XX from the laser optical axis and its angle is opposite the irradiation surface of PM to prevent viewing direct light from the plasma. Laser fluence was estimated from laser spot size on the PM and laser energy.

Figure 3-4 shows the reflectivity as a function of laser fluence. Reflectivity clearly depends on the laser fluence. In this measurement, minimum fluence is 20 J/cm^2. Reflectivity is 8% and it is quite high compared with reflectivity of AR coated surface. According to results reported by Wittmann et al, breakdown threshold is about 9.5 J/cm^2 (for 1.7ps duration pulse) and it does not depend on the difference of AR coating. (The threshold fluences were reported that 4 J/cm^2 , 9.5 J/cm^2 and 12.5 J/cm^2 for pulse durations of 60 fs, 1.7 ps and 4 ps respectively.)

We think that the breakdown threshold is lower than 20 J/cm^2 and the electron density exceeds the critical level (n_c) during irradiation and the plasma already begins to reflect.

Above the breakdown threshold with the increasing fluence, a sharp rise in the reflectivity was observed. When the laser fluence was about 50-100 J/cm^2, reflectivity increased up to about 50%. In the high-fluence range (>100 J/cm^2), reactivities decrease and were approached to 35%. The contrast enhancement of higher than 200 was achieved in the range of about 50-100 J/cm^2 fluence.

Figure 3-5 shows the energy distribution in the near-far field of the laser beam on the Teflon plastic plate when the PM was not activated (a), and when it was (b-d) activated at various laser fluence. Corresponding line-outs (a-d) through the center are also shown.

In the case Fig.3-5 (a), the mirror was highly reflective multilayer coated mirror (99.9% reflectivity) and laser fluence was below breakdown threshold (no PM was triggered). In the case of Fig.3-5 (b)-(d), the mirror was AR coated BK7 glass and the incident pulse had a duration of 1.2 ps with a high peak fluence of 50 J/cm^2, 400 J/cm^2, and 4000 J/cm^2 (PM was triggered). Significant

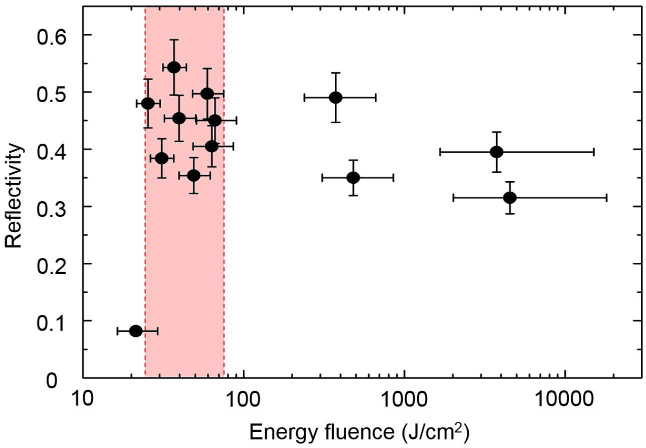

Figure 3-4: Overall reflectivity of the PM versus laser uence for 1.2 ps pulses. Above the breakdown threshold with the increasing uence, a sharp rise in the reflectivity was observed. When the laser fluence was about 50-100 J/cm^2, reflectivity increased up to about 50%. In the high-uence range (>100 J/cm^2), reactivities decrease and were approached to 35%. The contrast enhancement of higher than 200 was achieved in the range of about 50-100 J/cm^2 fluence.

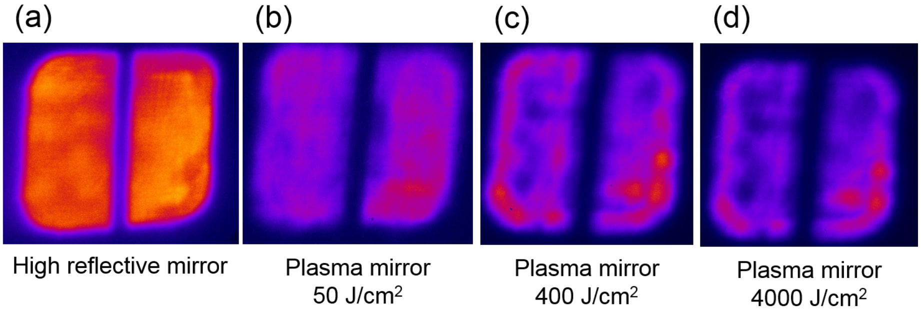

Figure 3-5: Reflected laser pattern from the plasma mirror with a fixed color scale, normalized with respect to the incident laser energy. The distortions in the patterns show the wavefront distortions due to a very high laser pulse intensity on the plasma mirror.

distortions in the laser pattern were observed in these shots with fluence over 500 J/cm^2. Thus, we concluded that the appropriate laser fluence was 50-100 Jcm^2. Thus, we concluded that the appropriate laser fluence was 50-100 J/cm^2. Scaling this condition to the 1.6 kJ LFEX using 4 beams with a total F number of 5, a 2 inch diameter plasma mirror located at 200 mm was designed (written in next subsection).

3.6 | Focusability of plasma mirror and manipulating system

3.6.1 | Spherical focusing plasma mirror

We designed a plasma mirror and a manipulating system for full power LFEX shot. The parabolic mirror of LFEX laser can not accept a large offset of focal position along in vertical and horizontal directions due to its geometrical limitations. Thus, we chose a spherical shaped mirror. It allows us to reimage the originally focused image to the target chamber center with only a small offsetting of the LFEX beam pointing.

According to results reported in above subsection, appropriate laser fluence is 50-100 J/cm^2. Scaling this condition to the 1.6 kJ LFEX using 4 beams with a total F number of 5, the appropriate laser fluence is obtained at 200 mm from TCC. From above scaling, curvature radius of mirror was determined to be 202 mm (f =101 mm). And rear surface of the mirror is flat.

The surfaces of both sides were polished optically, and coated by anti-reflected coating for 1ω light (1053 nm). The distance between two focusing points is designed to be 3 mm. The image at first imaging point are reimage at second imaging point. An enlargement ratio is 1. In theory of reflection of spherical shaped mirror, a ray that starts from center of curvature radius is refocused at same points. Therefore, if we uses a spherical mirror as image relay optics, spherical aberration inevitably exists. Additionally since the light source of the first imaging point always has a finite size, inevitable astigmatism occurs. To confirm the aberrations occurring in the our geometry, a ray tracing was calculated by ZMax code.

Figure 3-6 shows results of ray trace of the spherical shaped mirror, that was calculated by ZMax code. According to the ray tracing calculation, if rays emitted from infinitesimal source point (of the first imaging point), image is relayed as an image with 8 μm of diameter at the second imaging point.

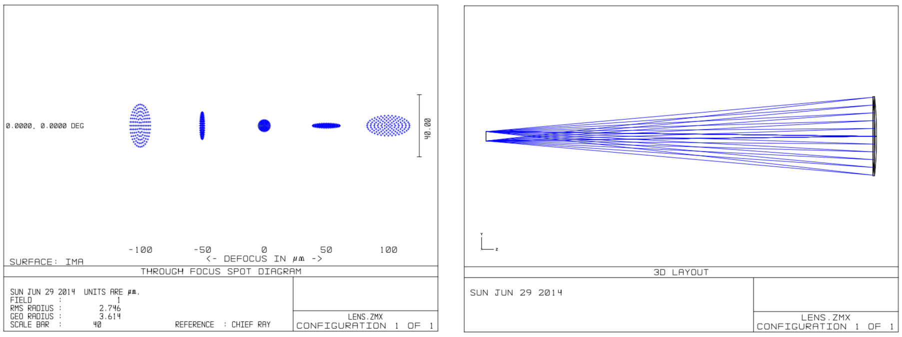

Figure 3-6: Ray tracing of the spherical shaped mirror calculated by ZMax code. According to the ray tracing calculation, if rays emitted from infinitesimal source point (of the first imaging point), image is relayed as an image with 8 μm of diameter at the second imaging point (due to spherical aberration and astigmatism).

The deterioration of the image due to aberrations, was also confirmed experimentally. The focal spots with and without the spherical shaped mirror were separately compared using a low-energy He-Ne laser (633 nm wavelength). The He-Ne laser had an equivalent F number of LFEX laser, and had a small spot of almost comparable with diffraction limit. The original 13 μm focal spot size of the FWHM [as shown in Fig.3-7 (a)] was reimaged using the spherical shaped mirror (surface reflection) with the FWHM new size of 16 μm [as shown in Fig.3-7 (b)]. The distortion can be simply estimated by the FWHM [as shown in Fig.3-7 (c)] $(16^2$ to $13^2)^{1/2} = 9.3$ μm. This shows good agreement with the results of the ray-trace simulation of 8 μm. Thus, the deterioration of the image by aberrations of the spherical shaped mirror, is negligibly small compared to several tens of micrometer of the LFEX spot.

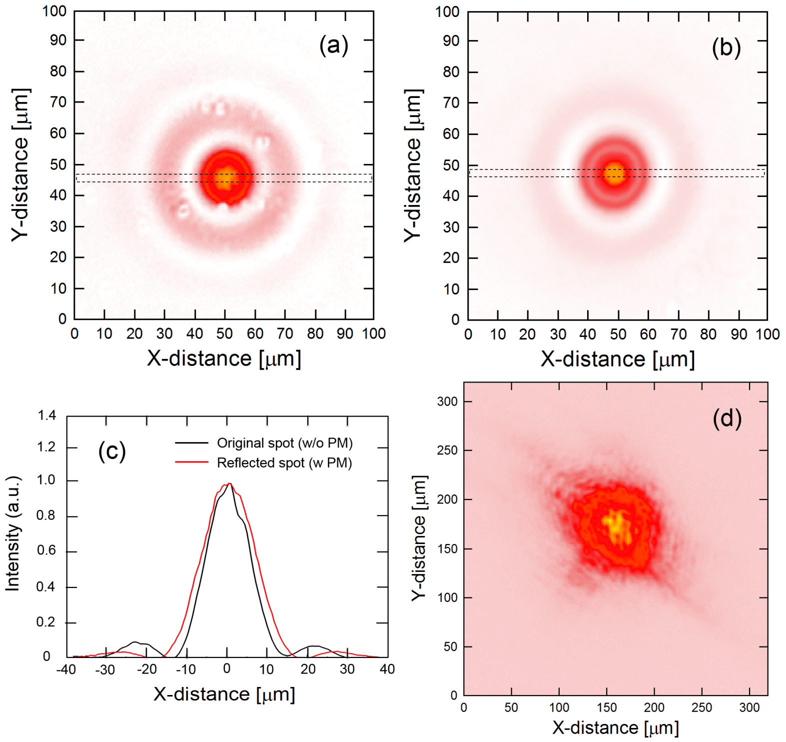

Figure 3-7: The original spot image of He-Ne laser at first imaging point (a). The spot image relayed by spherical shaped mirror at the second imaging point (b). The distortion can be simply estimated by the full width at halfmaximum $(16^2 \text{ to } 13^2)^{1/2} = 9.3\ \mu\text{m}$ (c). The deterioration of the image by aberrations of the spherical shaped mirror, is negligibly small to several tens of micrometer of the LFEX spot (d).

3.6.2 | Designing of a manipulating system

The interaction chamber is spherical, with no possibility of fine optics alignment in its interior, therefore the alignment and focusing of the PM is extremely challenging if performed inside the chamber. Since the laser is focused at the TCC, we must place accurately surface of target at the laser focal point. In a typical experiment, a mimic target is firstly put at TCC for the laser alignment. After the laser alignment, the mimic target is replaced to the real target, and then make the fine adjustment of the position of the target by high magnification cameras. Since the high magnification cameras are attached on the vacuum chamber, the target position can be finely adjusted within the focus depth of the LFEX laser.

In our experiment, we need to relay far field image of the laser at the TCC (first imaging point), to the target surface by the reflection of the plasma mirror. In this situation, we should adjust path length of round trip between the focal plane and the plasma mirror (A distance between the first imaging point and the mirror surface, and a distance between the mirror surface and the second imaging point). If the path length is not precisely adjusted within the focus depth, the reflected laser intensity by the PM on the target will be significantly reduced.

The best solution is to pre-align the PM on an external alignment system together with the target, using a CW laser mimicking the LFEX beam and called ”LFEX skeleton”. Pre-alignment system is configured with the three high magnification cameras and He-Ne laser that has the same F number of LFEX laser (Shown in Fig.3-9(a)). The target and the PM are put on the single bread board. The board on which the target and the plasma mirror is installed is referred to as the ”upper board", hereafter. Mutual relationship between the target and the PM was accurately adjusted on the pre-alignment system.

Another board to fix the top board was installed into the target chamber by target manipulator. (This board is referred to as the "lower board", hereafter.) Finally, the top board was installed on the bottom board in the chamber from 8 inch diameter port (Shown in Fig.3-9(b)). The unique position between top and bottom board in the chamber is well-defined by the three-point kinematic magnet base. In addition, the three-point kinematic magnet base is also attached on pre-alignment system. The unique position between top board and view of the camera of the pre-alignment system, can also be well-defined. The following is a more detailed working procedures.

(In pre-alignment system)
(STEP1) Define the axis of the pre-alignment system.

- Put a tiny plate, and adjust focus of the spot monitor to get a clear image of the plate surface.
- Adjust tilt of target and move z axis of target.

(If we can keep the clear image during moving along z axis, target surface is perpendicular to the surface of upper board.)

- Adjust a rotation of two camera of target monitor such that the edge of mirror is parallel to the edge of image of CCDs.

(STEP2) Define the origin of the pre-alignment system.

- Put 50 μm diameter gold-coated ball at 154 mm above the top surface of the upper board.
- Focus the mimic LFEX laser on the ball.

(Fix the target height)

- Adjust target position and put the target on the focal point of laser.

(See the shadow of the ball. Put the ball in position at which passing laser intensity is the lowest.)

- Maximize the magnification of two target monitor, and write the marker of origin on the screen (mark the position of the ball).

(STEP3) Create one-to-one relationship between the axis of LFEX laser and the axis of mimic LFEX laser.

- To define a perpendicular axis of mimic LFEX laser, we use auto-correlation of mimic LFEX laser.
- Extract the center of mimic LFEX laser using a pinhole.
- Put a tiny mirror at the origin.
- Adjust a rotation of the tiny mirror to reflect the laser on the incident axis.

(See the mirror surface, and keep it at the origin of the pre-alignment system.)

(In the target chamber)

- Install the bottom board in a target chamber by the target manipulator.
- Attach the top board on the bottom board.
- Adjust rotation of the target manipulator (rotation of bottom board) by the auto correlation of LFEX alignment laser.

(See the mirror surface, and keep it at the origin of the chamber.)

- After this step, the rotation axis of the target manipulator is fixed.
- By above step, the axis of the mimic LFEX laser became equal to axis of the LFEX laser.

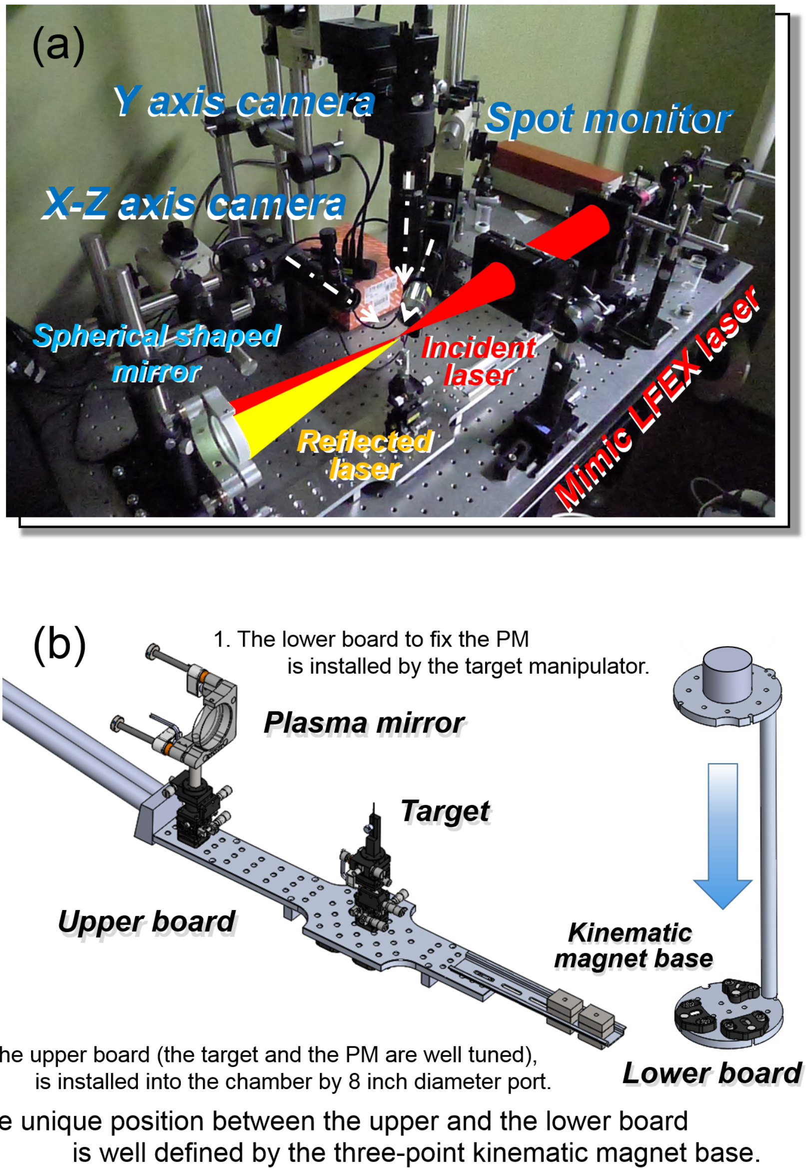

1. The lower board to fix the PM is installed by the target manipulator.

2. The upper board (the target and the PM are well tuned), is installed into the chamber by 8 inch diameter port.

The unique position between the upper and the lower board is well defined by the three-point kinematic magnet base.

Figure 3-8: (a) Pre-alignment system that is configured with the three high magnification cameras and He-Ne laser that has the same F number of LFEX laser. Mutual relationship between the target and the PM was accurately adjusted on the pre-alignment system. (b) Manipulating system of PM into chamber.

(STEP4) Adjust mutual position of the three point (first imaging point, plasma mirror and second imaging point).

- Put a double pinhole target. Adjust tilt of target, such that the surface become perpendicular to the surface of upper board.

(Double pinhole target has two pinholes aligned vertically. Its two holes are separated by 3 mm, and have 100 μm diameter.)

- Adjust the tilt of the spherical shaped mirror so that the laser passes through the two pinholes.

(The position of the top pin hole shows the first imaging point of the spherical shaped mirror. And the position of the bottom pin hole shows the second imaging point.)

- If the laser passes through the both two pinholes, pointing of reflected laser is consistent with the correct point in 50 μm accuracy.
- This accuracy is sufficient accuracy to achieve tight focus by plasma mirror to cone chips with a diameter of 70um in the fast ignition fusion research.
- Move the imaging point of the spot monitor to the bottom pinhole.
- Remove the double pinhole target, and put the tiny mirror at the position of the bottom pin hole.
- Adjust focus position of the reflected laser, using the tiny mirror and spot monitor.
- Put the surface of the tiny mirror in the range of focal depth of spot monitor.
- Adjust focusing axis of the spherical shaped mirror, and minimize the spot size.

(The focus point of reflected laser can be determined within the focal depth.)

- Put a actual target. Adjust rotation by the target monitor.
- Adjust position of focusing-axis by the spot monitor.

(If the target has large thickness, move target in order to consider thickness.)

(In the target chamber)
(STEP5) Final check

- Install the upper board on the lower board.
- Using the LFEX alignment laser, confirm the final focus position.

If the reflected laser is focused on the target, all preparation for shot have been completed.

3.7 | Pulse contrast estimation

Effect on improvement of the pulse contrast of plasma mirror, was measure by two different ways. The first method is based on an optical technique, and the second method is estimated by the time-resolved image of preformed plasma. These measurements were preformed independently of each other, and the results obtained from these measurements were in good agreement with each other.

3.7.1 | Pulse contrast estimation by optical technique

It was impossible to measure the pulse contrast directly after the plasma mirror on full energy shot of LFEX. Thus, we estimated the contrast before and after the mirror as following procedure. The operation of the PM (illustrated in Figure X) is based on the ultrafast ionization of material by intense laser light. PM is a anti-reflected coated optically flat glass in initial condition. When a high intense pulse hits an optically polished surface, it generates a dense plasma that itself acts as a mirror, known as a PM. When the shutter is driven at the leading edge of the main pulse, only main pulse is reflected by the PM, and arrives to a target. And the PM removes proceeding pulse. The

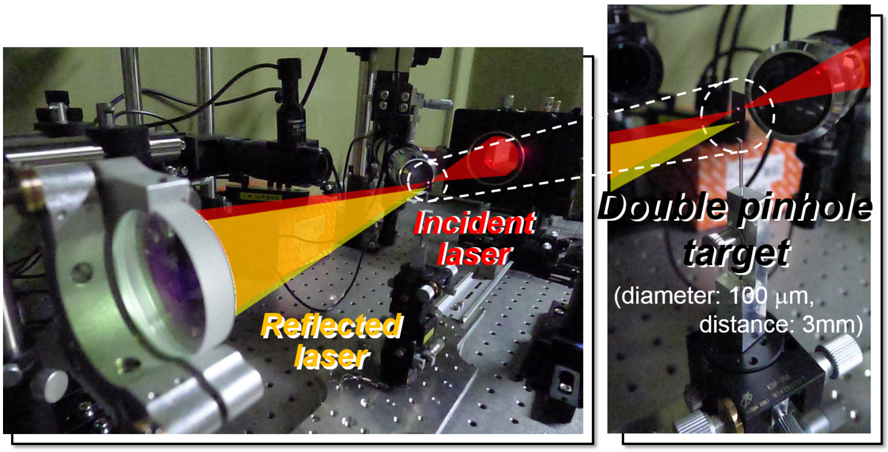

Figure 3-9: Fine tuning of plasma mirror using double pinhole target. Adjust mutual position of the three point (first imaging point, plasma mirror and second imaging point).Put a double pinhole target. Adjust the tilt of the spherical shaped mirror so that the laser passes through the two pinholes. If the laser passes through the both two pinholes, pointing of reflected laser is consistent with the correct point in 50um accuracy.

materials response during few cycle of laser frequency, and are ionized. Thus, we considered that the reflectivity of plasma mirror is changed like step function. The reflectivity of the plasma mirror is 0.5% before the plasma mirror triggering time (comparable to AR coating surface reflection) and it suddenly increases up to 50% after triggering time (measured at the individual experiment and reported at sec.3.5). The triggering time of plasma mirror was estimated by the transmitted laser light of the plasma using a fast response photodiode.

The laser temporal profile from -3 ns to -0.5 ns was measured using a 20 ps rise-time photo-diode connected to a 20-GHz oscilloscope. The one of edge of multi mode fiber was connected to the photo diode, and another edge of fiber was set at behind of Mirror No.8 (M8 is the first mirror after compressor.). A leakage laser pulse of M8 mirror was attenuate by neutral density filter to become appropriate level, and light was transported by the collimator lens coupled fiber. The laser temporal profile was measured at a full energy shot. Transmittance of neutral density filter, and signal response of the photodiode on total amount of light, were corrected by another experiment. The laser temporal profile from -0.5 ns to -0.3 ns was measured using a third-order cross-correlator equipped in the front end of the laser system with a mimic compressor with low-energy 6 Hz laser pulses. The main pulse duration was measured by the single-shot autocorrelator at the M8 mirror in a full energy shot.

The difference between the mimic compressor and the LFEX large compressor was taken into account on result of pedestal pulse contrast measurement. These three temporal profiles show a good agreement between each other, as shown in Fig.3-11. Envelope of blue line shows the temporal profile of the original pulse of LFEX (Without plasma mirror).

Next, the plasma mirror activating time was estimated from the total amount of energy of transmitted pulse of plasma mirror. Figure 3-12 shows the photodiode signal of the transmitted laser pulse, where the main peak is at 0 ns. Two signals preceding the signal of main pulse, are signals of specular-reflected components of the gratings in the compressor. (Here after, we refer to these components with the zero-order pulse.) These components arrive at -100 ns (pulse width 2 ns) and at -48 ns (pulse width smaller than 10 ps) before the main pulse. These zeroth-order pulses are generated at the compressor gratings, and they pass along almost the same laser path of main pulse. Their focal points are 8 mm away from the target. Thus, they can pass through the target

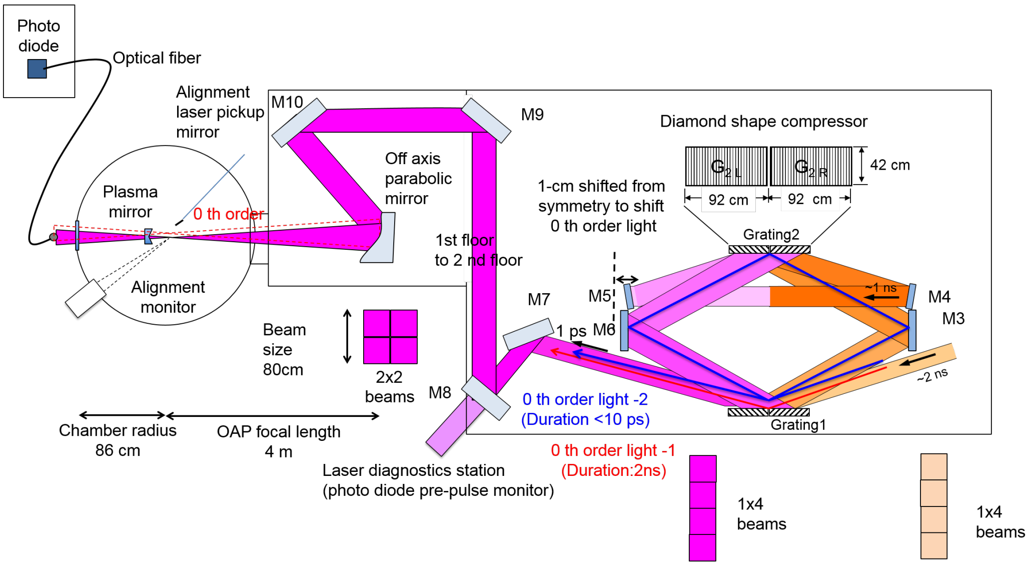

Figure 3-10: LFEX configuration from a compressor to a target. The laser beam path for zeroth-order lights, generated by the grating, and the main beam are illustrated.

in the both condition (with using PM and without using PM). And they are injected to the plasma mirror but intensity is low enough. Thus, the plasma is not generated.

The fraction of transmitted energy relative to the incident energy can be estimated by the ratio between the main pulse and the zeroth-order pulse. The ratio of the integrated signal between the main pulse and the zeroth-order pulse at -48 ns, averaged over 5 shots, was 0.76 ± 0.39. The original ratio between the zeroth-order and main pulses was estimated using a grating efficiency of 0.96 ± 0.01 for diffractiona value obtained from the inspection report. The detailed description of the grating can be consulted in Ref.[54]. The zeroth-order pulse at -48 ns diffracted twice with an efficiency of 0.96 ± 0.01 and once with specular reflection of $0.044 \pm 0.01\%$, giving 0.038 ± 0.009 in total. The main pulse passed through four diffractions of 0.96, resulting in 0.85 ± 0.04 in total. The ratio between the main pulse and the zeroth-order pulse before the plasma mirror was calculated to be 22 ± 5.4. Thus, the plasma mirror transmission efficiency was $(0.76 \pm 0.39)/(22 \pm 5.4) = 0.035 \pm 0.02$. The integral of the signal from -3 ns to -2 ± 1 ps of the initial LFEX pulse waveform, was equal to 0.035 ± 0.02 of the total. We concluded from this value that the laser pulse was mostly transmitted before -2 ps (0.5% reflectivity) and that the plasma mirror was consequently switched ON after it. The reflected laser pulse peak intensity was estimated to be 50% of the initial from the reflectivity. Thus, an improvement of 100 times in pulse contrast was obtained. The red dotted line shows the estimated laser temporal profile after the plasma mirror, assuming the above condition. Finally, the pulse contrast with a plasma mirror was estimated as 10^{11} at -1 ns.

3.7.2 | Pulse contrast estimation by preplasma

A 1 mm cubic gold target was irradiated by the high intense laser, and the preplasma was observed using flash back-light technique. Preplasma was clearly observed in the condition without a plasma mirror at 1.3 ns before the main pulse. While, in the plasma mirror shot, no preplasma was observed at 140 ps before the main pulse. From these results, we can see that the improved contrast laser by plasma mirror, has dramatically suppressed pre plasma formation. In addition, we can estimate the laser temporal profile from these images.

To estimate the pulse contrast, preplasma was simulated by using a two dimensional hydro-

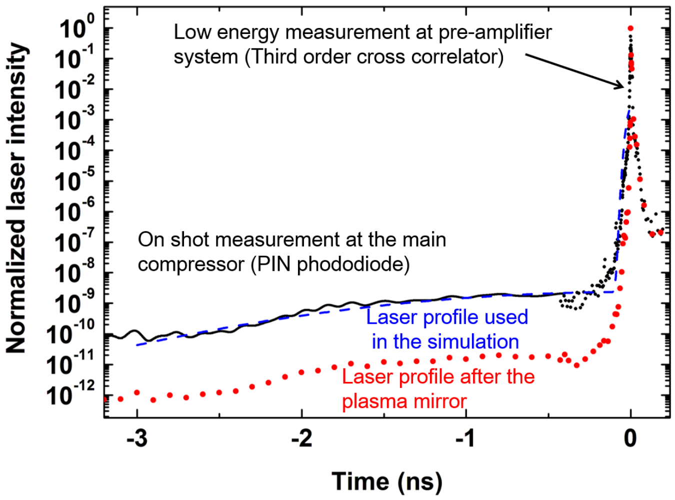

Figure 3-11: Laser temporal profiles of the LFEX measured by a PIN photodiode (3 to 0.4 ns) on a shot after the compressor and third-order cross-correlator (0.4 to 0 ns) with low-energy pulses in the preamplifier without a plasma mirror (black solid line). An estimated pulse profile in a condition with a plasma mirror is also plotted with a red dotted line. The blue line is the laser profile used in the simulation to estimate the preplasma.

dynamic simulation at various laser intensity profile. In the simulation, laser temporal profile was assumed a 3 ns Gaussian profile. And laser intensity was varied to find the best fit with the observed preplasma profile. Top images represent the observed preplasma profile in the experiment. Bottom images show simulated preplasma profile. White lines show result of a ray trace of the probe laser in the plasma. The laser temporal profile shown in blue dotted line was well reproduced the plasma expansion size observed by flash back-light technique. In addition, only a small fringe shift was observed at outer edge of expanding plasma. It indicates density gradient in this region, is very sharp. This characteristic of plasma was also confirmed with the simulated plasma density profile. Intensity contrast ratio of original high intense laser is 10^{-10} at 2.8 ns before main pulse, and 10^{-9} at 1.3 ns before main pulse. The laser contrast ratio of plasma mirror-reflected pulse, can be estimated 100 times better than the original pulse. And it is shown as red dotted line. In the plasma mirror shot with the laser profile of the red dotted line, a slightly expanding preplasma was observed in the simulation. However, this size is less than the spatial resolution of the optical diagnostics and It is impossible to observe. Plasma size at the 140 ps before of the main pulse, is reduced to less than lower level of observation. It is a good agreement with the experiment. Intensity contrast ratio of plasma mirror-reflected pulse is more than 10^{-10} at 140 ps before main pulse. In this contrast level, the preplasma scale length can be reduced to 1.5 μm, which is an ideal condition for fast ignition experiments.

3.8 | Conclusion

2 inch spherical plasma mirror was implemented in the LFEX system to improve laser pulse contrast. We measured a plasma mirror reflectivity of about 50% using a laser fluence of about 50 Jcm^2 on the mirror surface, limiting focal spot distortions. The transmission of the laser light energy through the plasma mirror was equal to $3.5\% \pm 2\%$, allowing us to estimate that the plasma mirror was triggered after a time of 2±1ps from the main peak. An improvement in the laser pulse contrast by a factor of 100 (and up to 10^{11}) was demonstrated on a kJ-class laser system. A significant reduction of

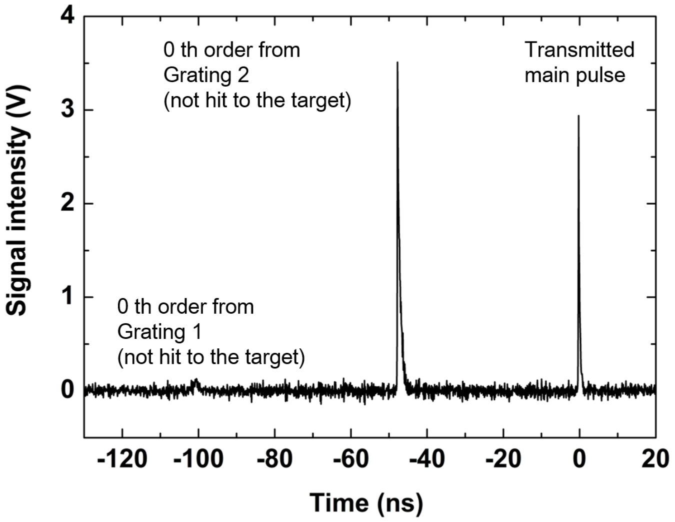

Figure 3-12: Photodiode signals of the transmitted laser pulse from the plasma mirror (at 0 ns) and the zeroth-order pulses from the gratings that pass through the side of the target (at 100 ns and 48 ns)

the preplasma was observed by optical interferometry. This technique is very promising, not only for fast ignition but also for opening very broad applications, such as ion acceleration or setting up a configuration of two counter-propagating laser beams. This technique can also be applied as beam transportation in a highly complex large-energy laser facility, such as OMEGA-EP, ORION, PETAL, and NIF-ARC with 1 ps operation. High contrast laser pulse is possible to extract only the influence of the pulse duration of the main pulse on the electron acceleration.

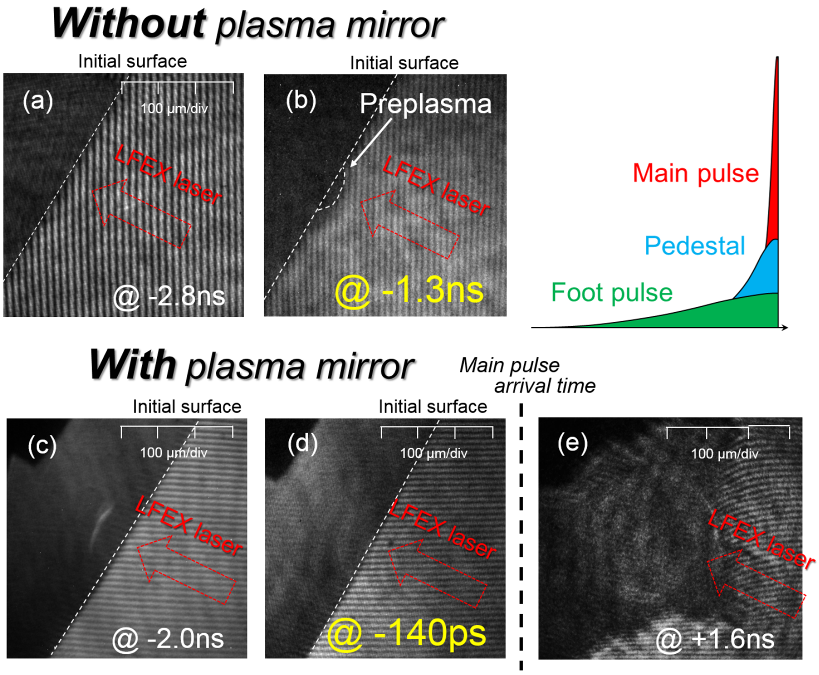

Figure 3-13: Experimentally observed interferogram images without a plasma mirror at -2.8 ns (a) and -1.3 ns (b) and with a plasma mirror at -2.0 ns (c), at -140 ps (d) and at +1.6 ns (e).

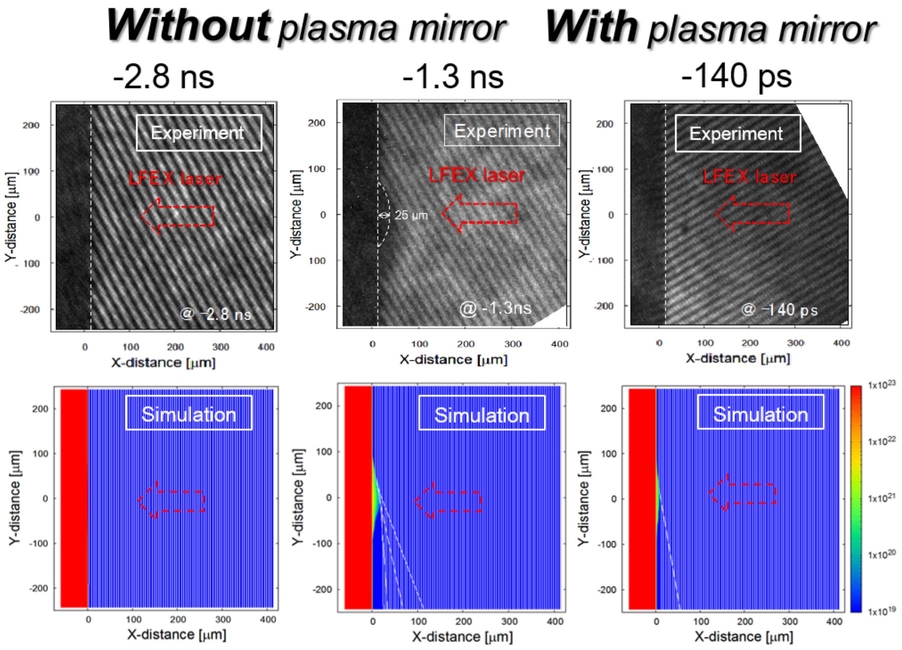

Figure 3-14: Experimentally observed interferogram images without a plasma mirror at -2.8 ns (left) and -1.3 ns (center) and with a plasma mirror at -140 ps (right). The electron density profile by 2D hydrodynamic simulation is shown in log scale for comparison with the experimental data. Simulated laser ray-trace lines show the shadow size of the plasma.

CHAPTER 4

Estimation of energy distribution and energy conversion efficiency of relativistic electrons by spectrum reconstruction of hard x ray

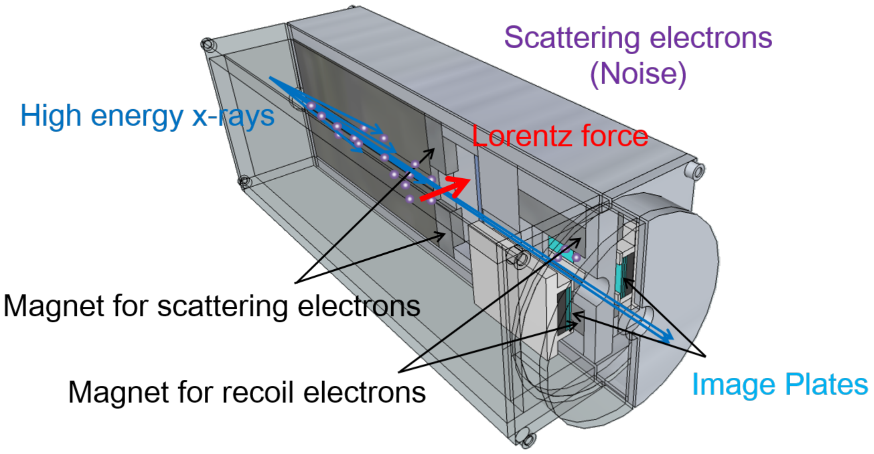

4.1 | Introduction

When laser intensity on the surface of a matter exceeds 10^{18} W/cm^2, the strong oscillating electric-magnetic field directly accelerates electrons to the speed of light. Laser-accelerated relativistic electrons emit intense hard X-ray pulses by the bremsstrahlung process in the matter and plasma. The photon energy of the hard X-ray pulse can reach several tens of mega-electronvolts, and its duration is close to that of the laser pulse. The absolute energy flux and angular distribution of the hard X-rays reflect the laser-plasma interactions. Furthermore, nuclear reactions that occur in high energy density plasma can be investigated by measuring the spectrum and intensity of γ-rays associated with nuclear transitions.

A bundle of hard X-ray detectors with different energy thresholds is used as a conventional single-shot spectrometer for high-flux hard X-rays. Hereafter, this type of spectrometer is referred to as a differential energy threshold (DET) X-ray spectrometer. An X-ray spectrum is obtained from the differences in signal intensity between the detectors with assumptions of spectrum shape (continuum emission and/or expected line emissions). Bound-free photoelectric absorption,[55, 56, 40] photonuclear reactions,[57, 58] and Cherenkov radiation[59] are used to select energy thresholds for the responses of the detectors. After the first demonstration of the DET X-ray spectrometer by Verbinski *et al.*,[60] several spectrometers were developed; however, high-energy resolution ($\Delta h\nu / h\nu < 0.1$) is not achievable with the DET X-ray spectrometer because the energy resolution is limited by the energy differences between the thresholds of the detectors.

A Compton X-ray spectrometer is thus proposed to obtain a higher energy resolution than the DET X-ray spectrometer[61, 62, 63, 64]. X-rays are converted into recoil electrons in the Compton X-ray spectrometer by Compton scattering in a X ray-electron converter. The energy distribution of the recoil electrons is measured with an electron energy analyzer and an incident X-ray spectrum is calculated from the energy distribution of the recoil electrons.

First half of this chapter reports the development of the Compton X-ray spectrometer that is applicable to high intensity laser-plasma interaction experiment. The Compton X-ray spectrometer can be applied to other studies with some modifications. The principle and design of the Compton X-ray spectrometer are described in sec.4.2.1. The material and thickness of the X ray-electron converter must be optimized to maximize the detection efficiency and energy resolution of the Compton X-ray spectrometer, which is discussed in sec.4.2.2. In addition, background reduction and subtraction processes, which are critically important for the Compton X-ray spectrometer, are also discussed in sec.4.2.4. In sec.4.3, the energy resolution evaluation of Compton X-ray spectrometer on mono-energy X-ray measurement using radioisotopes, is shown. In sec.4.4, the accuracy evaluation of Compton X-ray spectrometer on bremsstrahlung X-ray measurement using a linear accelerator, is shown. Application of the Compton X-ray spectrometer to a laser-plasma interaction experiment is described in sec.4.5.

In second half of this chapter, we describe the estimation method of the average energy and the energy conversion efficiency of relativistic electrons by spectral reconstruction of hard x-rays measured by High Energy X-ray Spectrometer which is one of DET X-ray spectrometers. Although this spectrometer is inferior to the Compton spectrometer on energy resolution, it has high sensitivity. The reason for this is that the Compton spectrometer measures via converting X-rays into recoil electrons, while HEXS directly observes x-rays by the IP. Since energy resolution of single HEXS is low, we can not estimate the energy conversion efficiency and the average energy of electrons by only single HEXS. However, hard X-ray spectrum measurement with multiple HEXSs surrounding the target can increase the accuracy of estimation of conversion efficiency and average energy. The signals recorded on the IPs of these HEXSs are comprehensively analyzed using Monte Carlo simulation considering three dimensional hard x-ray radiation distribution. In sec.4.6, we describes a method of estimating the average energy of relativistic electrons and energy conversion efficiency by spectral reconstruction of hard X-rays observed by multiple HEXSs.

4.2 | Principle and design of the Compton X-ray spectrometer

4.2.1 | Principle of the Compton X-ray spectrometer

Compton scattering is the dominant process of interactions between atoms and photons, of which the energy is higher than 0.5 MeV. The total energy and momentum of a scattered X ray and a recoil electron are equivalent to the energy of an incident X ray and electron before scattering. The incident X ray energy can be obtained from the energy conservation law by measuring the energy and angle of the recoil electron. Equation (4.1) is the relationship between the energies (MeV) of an incident X ray ($h\nu$) and an electron (E_e) recoiled to the forward direction:

$$E_e = h\nu - \frac{h\nu}{1 + \frac{2h\nu}{0.511}} \tag{4.1}$$

In the Compton X-ray spectrometer, hard X-rays are converted to recoil electrons by Compton scattering in the X ray-electron converter and the energy distribution of the recoil electrons is measured with a magnet-based electron-energy analyzer. In principle, the incident X-ray energy can be calculated directly from the measured energy of the recoil electron, according to Eq.(4.1); however, there are several factors that broaden energy spread of the recoil electrons.

The first factor is the energy spread of the recoil electrons (ΔE_{col}) due to their multiple collisions with bulk electrons in the converter. The other factor is the energy resolution of the electron energy analyzer, which is determined mainly by the finite width of the entrance slit (ΔE_{slit}) of the analyzer. The energy resolution of the recoil electron is given by $\Delta E/E$. Total energy spread ($\Delta E = E_{e2}\ - E_{e1}$) can be approximated as the sum of the squares of the widths of these two energy distributions ($\Delta E_2 = \Delta E_{col2} + \Delta E_{slit2}$). Monte Carlo simulations (MCNP5[65] and GEANT4[66]) of photon-particle-atom interactions were used to obtain the incident X-ray spectrum from the energy distribution of the recoil electrons with the consideration the about factors. To determine the energy resolution of the Compton X-ray spectrometer ($\Delta h\nu/h\nu, \Delta h\nu = h\nu_2 - h\nu_1$), we calculate the values $h\nu_1$ and $h\nu_2$ by substituting E_{e1} and E_{e2} into Eq.(4.1), here E_{e1} and E_{e2} are energies of the electrons recoiled by photons having $h\nu_1$ and $h\nu_2$.

The spectrometer consists of seven parts, as shown in Fig.4-1: the first cleanup magnet, the lead X-ray collimator, the second cleanup magnet, the X ray-electron converter, the electron slit, the magnet-based electron energy analyzer and the lead armors. The first cleanup magnet filters out electrons that enter directly from the target/plasma to the spectrometer. The lead X-ray collimator defines the incident angle of X-rays to the converter. The second cleanup magnet is located between the X-ray collimator and the X ray-electron converter, and this filters out recoil electrons from the X-ray path that are generated at the first cleanup magnet and the X-ray collimator. The collimated X-rays are converted to recoil electrons in the X ray-electron converter. The slit is located in the front of the electron energy analyzer and defines the recoil angle of the recoil electrons. The magnet in the analyzer disperses the recoil electrons according to their kinetic energy, and the dispersed electron signal is recorded on an imaging plate (IP).

The ratio between the number of emitted X-ray photons and the recoil electrons is represented as $\eta = \eta_{collection}\eta_{conversion}\eta_{detection}$. Here $\eta_{collection}$, $\eta_{conversion}$ and $\eta_{detection}$ are, respectively, the collection efficiency of the emitted X rays by the spectrometer, the conversion efficiency from incident X ray photons to forward recoil electrons in the converter, and the detection efficiency of the recoiled electrons by a detector in the electron energy analyzer. More specifically, $\eta_{collection}$ is determined by

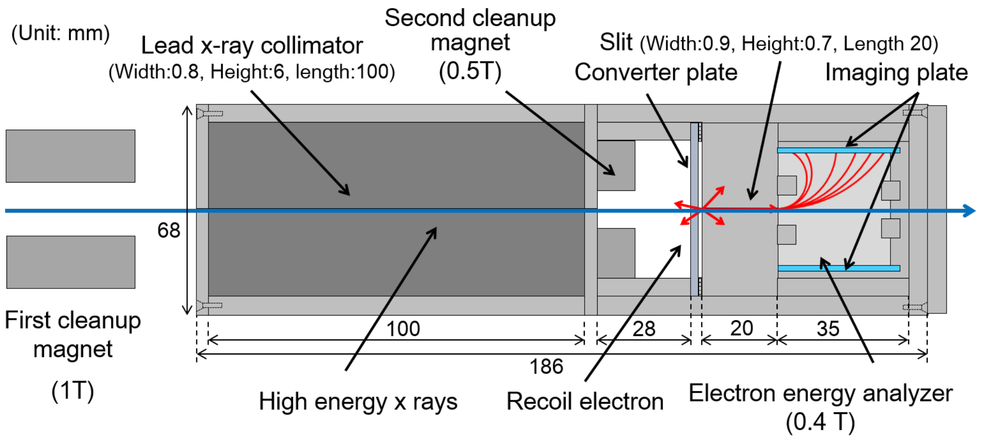

Figure 4-1: Schematic drawing of the Compton X-ray spectrometer. The first cleanup magnet filters out electrons that enter directly from the target to the spectrometer. The lead X-ray collimator defines the incident angle of X-rays to the converter. The second cleanup magnet is located between the X-ray collimator and the X ray-electron converter, and this filters out recoil electrons from the X-ray path that are generated in the first cleanup magnet and the X-ray collimator. The collimated X-rays are converted to recoil electrons in the X ray-electron converter. The slit is located in the front of the electron energy analyzer and defines the recoil angle of the recoil electrons. The magnet in the analyzer disperses the recoil electrons according to their kinetic energy, and the dispersed electron signal is recorded on the imaging plate.

angular distribution of emitted X rays and a cross section of the entrance collimator of the Compton X-ray spectrometer. $\eta_{conversion}$ and $\eta_{detection}$ are calculated by Monte Carlo simulation including converter thickness, geometries of the entrance slit of the recoil electron analyzer and detector size. The dependence of $\eta_{conversion}$ on X-ray energies was calculated by the Monte Carlo simulation. The dependence of $\eta_{detection}$ on electron recoil energies due to the difference of path length in the IP was considered in the Monte Carlo simulation.

4.2.2 | Optimization of X ray-electron converter

The thickness and material of the X ray-electron converter must be optimized to maximize the detection efficiency and energy resolution of the spectrometer. However, there is a trade-off relationship between these features of the spectrometer. A higher detection efficiency can generally be obtained with a thicker converter; however, the energy resolution is reduced because recoil electrons suffer from more collisions with bulk electrons in a thicker converter. The cross-sections for Compton scattering, the photoelectric effect, and the electron-positron pair creation are given as:

$$\mu_{compton} \propto (h\nu)^{-1} \tag{4.2}$$

$$\mu_{photo} \propto (h\nu)^{-\frac{7}{2}} \tag{4.3}$$

$$\mu_{pair} \propto Z(h\nu - 1.02) \tag{4.4}$$

where $h\nu$ and Z are the photon energy of incident X-rays and the atomic number, respectively. The conversion efficiency from an X-ray photon to recoil electrons is dependent on the density (ρ) and thickness (l) of the X ray-electron converter but is not dependent on the converter material

(Z). The energy range in which Compton scattering is dominant over the photoelectric effect and electron-positron pair creation becomes narrower in a higher Z material because those two cross-sections [Eqs.(4.3) and (4.4)] are proportional to Z^4 and Z, respectively. A low-Z converter is preferable to maximize the number of electrons recoiled by Compton scattering.

The conversion efficiency of the X ray-electron converter and the recoil electron energy distribution was calculated with Monte Carlo simulation code (MCNP5). The simulation was performed with Au and SiO_2 converters and mono energetic 1 MeV X-rays, of which the incident angle was normal to the converter. The number and energy distribution of electrons recoiled to $180 \pm 1.3°$ from the X-ray incident axis were measured in the simulation. Figure 4-2 (a) shows the conversion efficiencies from incident 1 MeV photons to electrons that were calculated for Au converter (solid line) and SiO_2 converter (broken line). The conversion efficiency is defined as the ratio between the number of incident photons and the number of recoiled electrons, where the energy loss due to multiple collisions is less than 10% of the initial energy of the recoiled electrons. The conversion efficiency increases linearly with the areal density of the converter and saturates at 0.02 g/cm^2 for both converters. These areal densities are close to one-tenth of the range of recoil electrons in SiO_2 (0.297 g/cm^2) and Au (0.290 g/cm^2). Figure 4-2 (b) shows the energy spread of recoil electrons due to multiple collisions. A 0.015 g/cm^2 areal density was chosen in this study as a converter thickness to obtain less than 0.1 of the energy spread ($\Delta E_{col}/E$).

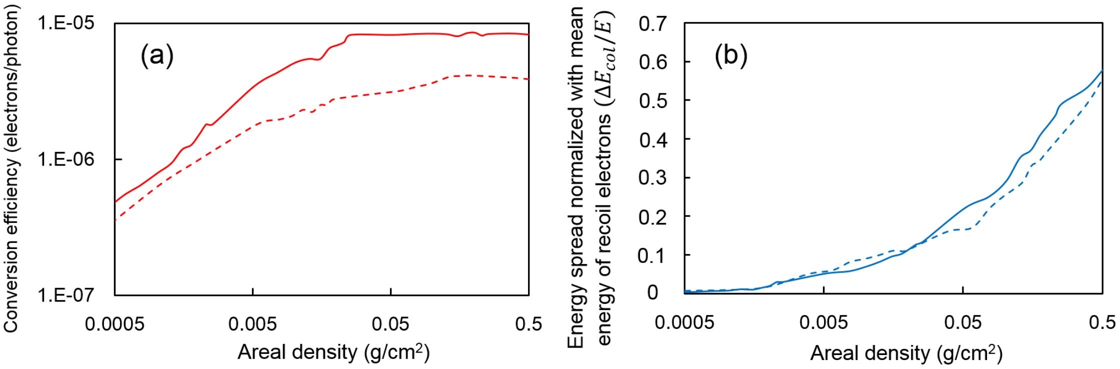

Figure 4-2: (a) Photon-electron conversion efficiency for 1 MeV photons as a function of the areal densities of SiO_2 (solid line) and Au (broken line) converters. The conversion efficiency is defined as the ratio between the number of incident 1 MeV photons and the number of recoil electrons, where the energy loss due to multiple collisions is less than 10% of the initial energy of the recoiled electrons. (b) shows the energy spread of recoil electrons due to multiple collisions. A 0.015 g/cm^2 areal density was chosen as the converter thickness to obtain less than 0.1 of the energy spread ($\Delta E_{col}/E$).

4.2.3 | Electron collimator and electron energy analyzer

A permanent magnet with a magnetic flux density of 0.4 T was used in the electron energy analyzer. Electrons are dispersed by the magnetic field according to their kinetic energies, whereby electrons with different kinetic energies are incident on the IP at different positions. The location of each electron is determined by a Larmor radius, which is dependent on the magnetic flux density and the electron kinetic energy. The electron kinetic energy at the position (l) of the IP is given by:

$$\epsilon(l) = m_0 c\left[\sqrt{\left(\frac{l^2+h^2}{2h}\right)^2\left(\frac{eB}{m_0 c}\right)^2+1}-1\right], \tag{4.5}$$

where ϵ is the electron kinetic energy, h is the height of the entrance slit from the IP surface, e is the elementary charge, B is the magnetic flux density, m_0 is the mass of electron, and c is the speed of light. The entrance slit has a finite width (Δh); therefore, the electron signal has a finite spread on the IP, even with mono-energy electrons[67]. This is the dominant source of uncertainty in determining the electron energy (ΔE_{slit}).

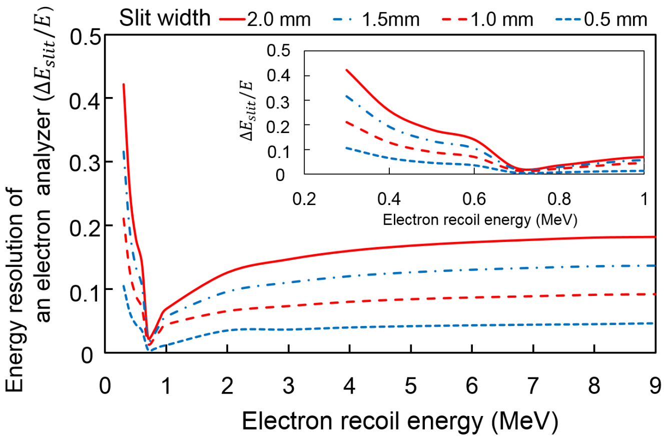

Figure 4-3: Energy resolutions of an electron energy analyzer ($\Delta E_{slit}/E$) are calculated for four different slit widths of 0.5 (dashed line), 1.0 (broken line), 1.5 (dot-dashed line), and 2.0 (solid line) mm. In the developed spectrometer, the slit width was 0.9 mm to obtain less than 0.1 of the energy resolution in the energy range 1-9 MeV.

Figure 4-3 shows energy resolutions of an electron energy analyzer ($\Delta E_{slit}/E$) that are calculated for four slit widths of 0.5 (dashed line), 1.0 (broken line), 1.5 (dot-dashed line), and 2.0 (solid line) mm, respectively. The energy resolution was calculated using Eq.(4.5) with h varied from $h_0 - \Delta h/2$ to $h_0 + \Delta h/2$, where $h_0 = 7$ mm is the height of the entrance slit center from the IP plane. In the developed spectrometer, the slit width was 0.9 mm to obtain less than 0.1 of the energy resolution in the energy range 1-9 MeV. The slit is made of a 20 mm thick aluminum to absorb 99% of the incident 9 MeV electrons. Figure 4 shows energy resolutions of the Compton X-ray spectrometer ($\Delta h\nu/h\nu$) that was calculated by using Eq.(4.1) and energy resolution of recoil electron ($\Delta E/E$). The red solid line and black broken line show energy resolutions for a 5-μm-thickness Au converter and a 200-μm-thickness SiO_2 converter, respectively. Energy resolution of the Compton spectrometer is better than 0.1 within the photon energy range of 0.8-10 MeV. Blue solid dots show experimental data that are discussed in sec.4.3. Experimentally evaluated energy resolutions agree fairly well with the calculated curve.

4.2.4 | Background reduction and subtraction

Background reduction is essential for the Compton X-ray spectrometer due to its low sensitivity. The following four schemes were used in the developed spectrometer to reduce and subtract the background from the signal: the lead armor covering the spectrometer, the first and second cleanup magnets, and the additional IP for recoding background. Because the IP has high sensitivity for

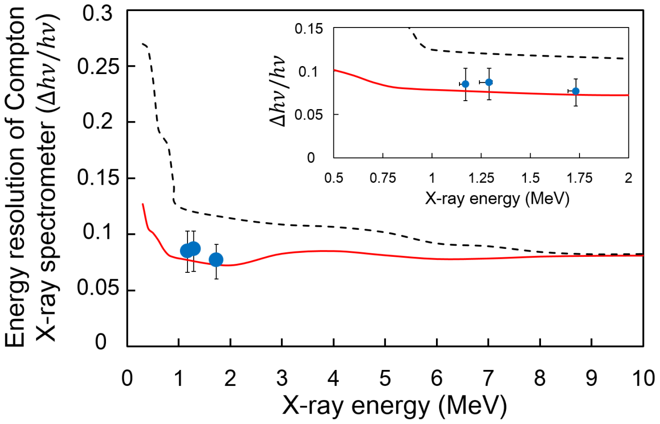

Figure 4-4: Energy resolutions of the Compton X-ray spectrometer ($\Delta h\nu/h\nu$) that was calculated by using Eq.(4.1) for energy resolution of recoil electron ($\Delta E/E$). The red solid line and black broken line show energy resolutions for a 5-μm-thickness Au converter and a 200-μm-thickness SiO_2 converter, respectively. Blue solid dots show experimental data that are discussed in Sec.4.3.

X-rays, background of IP is caused by X-rays scattered in the experimental apparatus surrounding the spectrometer. The spectrometer is covered with lead plates (armor) to exclude the scattered X-rays from the detection area. The thickness of the front plates and side armor is 10 cm and 5 cm, respectively. Fast electrons that enter the spectrometer directly from the target/plasma also generate background in the measured spectrum. The first cleanup magnet with a maximum magnetic flux density of 1 T is located at the head of the spectrometer to exclude fast electrons from the diagnostics line. Electrons generated by X-rays in the X-ray collimator are also a source of background. The second cleanup magnet with a maximum magnetic flux density of 0.4 T is located between the X-ray collimator and the converter to exclude such recoil electrons from the diagnostic line. The other background source is X-rays scattered by the converter and the electron slit. The additional IP is placed on the opposite side of the primary IP to record only the background generated by scattered X-rays. The background recorded on the additional IP is then subtracted from the signal recorded on the primary IP. Signal-to-background ratio was improved to be 1.5-3 in < 5 MeV range and 1.3-1.5 in > 5 MeV range after the implementation of background reduction methods described above as shown in Fig.4-5.

4.3 | Evaluation of energy resolution of Compton X-ray spectrometer

4.3.1 | Energy resolution of electron energy analyzer

The ^{137}Cs radioactive isotope (28.14 kBq, 5 hour) emits mono energetic (0.6246 MeV) electrons by internal conversion as well as broad-energy electrons by β- decay with maximum energies of 0.512 and 1.174 MeV. The absolute response of the IP (BAS-SR) and the IP scanner (GE Typhoon 7000) for electrons was calibrated in a previous experiment.[68]

Figure 4-7 shows a comparison of the measured (red solid circles) and calculated (black solid line) electron spectra taking into account the energy resolution of the analyzer, which was estimated from the 0.9 mm slit width using Eq.(4.5). The calculated electron spectrum was obtained by the convolution of a theoretical electron spectrum of β-decay of ^{137}Cs and an energy resolution of the

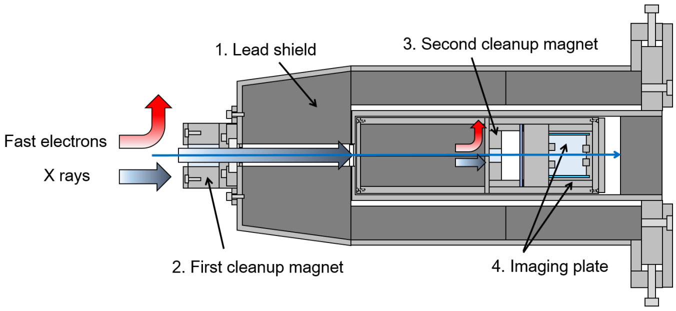

Figure 4-5: Cross-sectional view of the spectrometer. The spectrometer is covered with lead plates (armor) to exclude the scattered X-rays from the detection area. An additional IP is placed on the opposite side of the primary IP to record only background generated by scattered X-rays. The background recorded on the additional IP is then subtracted from the signal recorded on the primary IP.

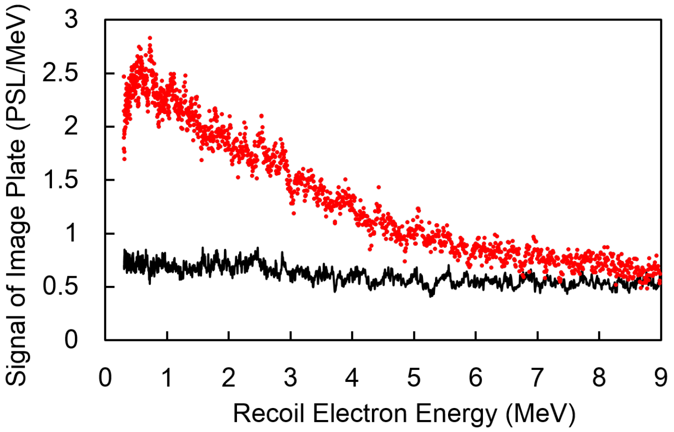

Figure 4-6: Photo stimulated luminescence (PSL) intensities induced by recoil electrons detected by IPs after the implement of background reduction methods. Red dots and black solid line are recoil electron signal recorded on the primary IP and background signal recorded on the additional IP, respectively. The additional IP is placed on the opposite side of the primary IP. Signal-to-background ratio was improved to be 1.5-3 in < 5 MeV range and 1.3-1.5 in > 5 MeV range.

analyzer determined by the slit. Blue broken line and green dotted line show calculated electron spectra with 2 mm and 0.2 mm slit width for reference. The black line fits reasonably well with the measured electron energy distribution, which indicates the energy resolution of the electron energy analyzer is determined predominantly by the slit width. The energy resolution of the electron energy analyzer ($\Delta E_{slit}/E$) was 0.07 at 0.624 MeV, which was evaluated from FWHM of the energy spread of 0.624 MeV mono-energy electrons.

4.3.2 | Energy resolution of the Compton X-ray spectrometer

The energy resolution of the developed Compton X-ray spectrometer was evaluated using two mono energetic γ rays (1.1732 and 1.3325 MeV) emitted from ^{60}Co radioactive isotopes and other γ rays generated by laser-Compton scattering (1.731 MeV). The ^{60}Co source (6.2 TBq) was cylindrical with a 2.5 cm diameter and 15 cm long and was located 52 cm from the spectrometer. In the measurement, a 5 μm thick Au foil was used as the X ray-electron converter. Figure 4-9 shows the

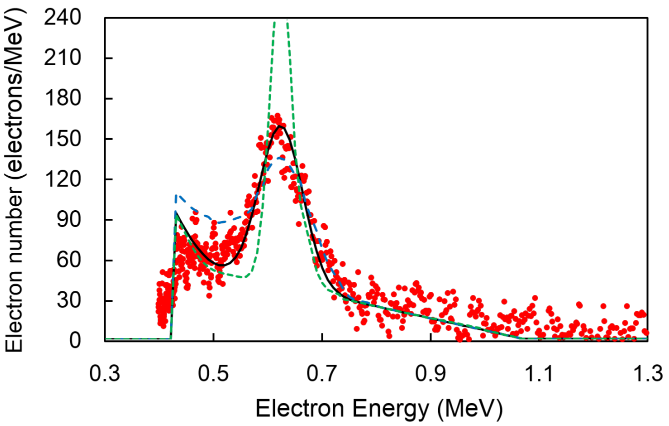

Figure 4-7: Comparison between the measured electron spectrum (red solid circles) and the calculated spectrum (black solid line) taking into account the finite energy resolution of the electron energy analyzer, as estimated from the slit width using Eq.(4.5). The energy resolution of the electron energy analyzer ($\Delta E_{slit}/E$) was 0.07 at 0.624 MeV that was evaluated from the FWHM of the energy spread of 0.624 MeV mono energetic electrons that are emitted by internal conversion in the ^{137}Cs radioactive isotope.

measured spectrum of recoil electrons and that calculated taking into account the energy resolution of the spectrometer. Two peaks appear at 0.963 and 1.118 MeV, which correspond to recoil energies of 1.1732 and 1.3325 MeV γ-rays, respectively. Each peak in the calculated energy distribution agrees well with the sum of the squares of the widths of two energy resolutions ($\Delta E^2 = \Delta E_{col}^2 + \Delta E_{slit}^2$). The energy spectrum (black solid line in Fig.4-9) was calculated as a convolution of a recoil electron spectrum computed by Monte Carlo simulation (MCNP5) and an energy resolution of the electron energy analyzer ($\Delta E_{slit}/E$). Gaussian fitting was performed for the left and right wings of each peak. Centroid energies of each peak were found at 0.94 MeV (-0.03/+0.01 MeV) and 1.07 MeV (-0.034/+0.017 MeV), respectively. Here, errors of centroid energies of each peak were differences of energies where electron number become 90% of the peak number. The energy resolution of the recoil electron ($\Delta E/E$), the ratio between FWHM of the peak and the initial energy of electron recoiled to the forward direction, were estimated to be 0.104 for 1.1732MeV and 0.112 for 1.3325MeV respectively. Incident X-ray energy was calculated by using Eq. (4.1). The energy resolutions of the X-ray spectrometer ($\Delta h\nu/h\nu$) were estimated to be 0.085 at 1.1732 MeV and 0.093 at 1.3325 MeV. Absolute recoil electron number also agrees well with calculated number taking into account the geometrical consideration of the lead collimator ($\eta_{collection} = 2.96 \times 10^{-7}$), conversion ratio from x rays to recoil electrons ($\eta_{conversion}$) and the detection ratio of recoil electrons ($\eta_{detection}$).

Laser-Compton scattering X ray were generated on New SUBARU facility. In the case of head on collision between relativistic electrons and photons, the scattered X-ray energy E_γ is written by

$$E_\gamma = \frac{1 + 4E_L\gamma^2}{1 + \gamma^2\theta^2 + 4E_L\gamma/mc^2} \tag{4.6}$$

where γ is a Lorentz factor, m is the rest mass of electron, c is the speed of light in vacuum, θ is an angle of scattered photon measured from the electron beam axis and E_L is the laser photon energy. A 983 MeV electron beam, circulating in the storage ring, collides with CO_2 laser pulse having 10.59 μm of wavelength to produce laser-Compton scattering X rays [69]. Quasi-mono energetic X-ray beam scattered ($\approx$1.731 MeV) within 0.05 mrad from electron beam axis is obtained by using the 0.8 mm width collimator located at 16 m from the electron-photon collision point. In the measurement,

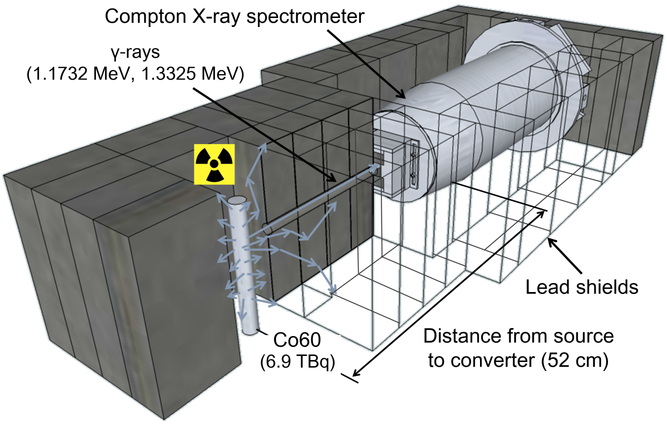

Figure 4-8: Experimental setup. The energy resolution of the developed Compton X-ray spectrometer was evaluated using two mono energetic γ rays (1.1732 and 1.3325 MeV) emitted from ^{60}Co radioactive isotopes and other γ rays generated by laser-Compton scattering (1.731 MeV).

a 5 μm thick Au foil was used as the X ray-electron converter. Figure 4-10 shows the measured spectrum of recoil electrons and that calculated with the energy resolution of the Compton x-ray spectrometer. The strongest peak appears at 1.508 MeV (-0.04/+0.01 MeV), which correspond to 1.731 MeV X ray. The energy resolution of the spectrometer ($\Delta h\nu/h\nu$) was estimated to be 0.077 at 1.731 MeV. The measured spectral resolutions are compared with the calculated ones in Fig.4-10.

4.4 | Accuracy evaluation of a Compton X-ray spectrometer with bremsstrahlung X-rays generated by a 6 MeV electron bunch

The accuracy of Compton X-ray spectrometer on bremsstrahlung X-ray measurement, was evaluated using a quasi-monoenergetic 6 MeV electron bunch that emanates from a linear accelerator. This experiment was performed in a linear accelerator facility, from which a 6 MeV electron bunch emanates. The electron bunch was injected into a 1.5 mm thick tungsten plate, and intense bremsstrahlung X-rays are emitted from the target. The Compton X-ray spectrometer was set at 0° with respect to the incident electrons' axis.

Figure 4-11 shows the comparison between the measured (red dots) and best-fit (black line) spectra of the recoil electrons. X-ray spectrum $f(h\nu)$ is reconstructed from the measured recoil electron energy distribution according to the following processes.

To simplify the reconstruction process, the X-ray spectrum is assumed to be the sum of Boltzmann functions [Eq.(4.7)], as shown in the following equation:

$$f(h\nu) = \sum_{n=1}^{N} R_n \exp\left(-\frac{h\nu}{T_n}\right) \tag{4.7}$$

where $h\nu$, R_n, T_n, and N are the photon energy, relative intensity, slope temperature, and number of Boltzmann functions, respectively. The MCNP5 code, which is a Monte Carlo code, is used to calculate the energy distribution of the recoil electrons [$g(E, T_n)$] that are generated by Boltzmann-spectrum X-rays [$\exp(h\nu/T_n)$] with an arbitrary temperature (T_n). The energy resolution of the electron energy analyzer is considered in this calculation. The X-ray spectrum is reconstructed by

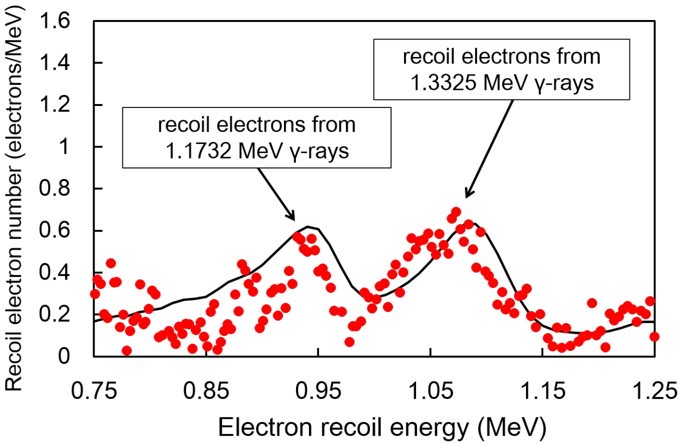

Figure 4-9: Measured recoil electron spectrum (red solid circles) and that calculated (solid line) taking into account the energy resolution of the spectrometer Two peaks appear at 0.963 and 1.118 MeV, which correspond to recoil energies of 1.1732 and 1.3325 MeV γ-rays, respectively, emitted from ^{60}Co isotopes. The energy resolutions of the spectrometer ($\Delta h\nu/h\nu$) were estimated to be 0.085 at 1.1732 MeV and 0.093 at 1.3325 MeV.

finding the best combination of $g(E, T_n)$ in $\sum_{n=1}^{N} R_n g(E, T_n)$ to minimize the sum of the mean-squared deviations between the measured distribution and the combination. T_n and R_n are varied from 0.1 to 10 MeV and from 0.001 to 1000, respectively, in this process, while R_n is fixed at 1. Although the sum of the mean-squared deviations becomes smaller for larger N, we find that the sum approaches an asymptotic value for $N > 4$. To reduce calculation time, the number of Boltzmann functions is set to $N = 5$ in this analysis.

The best-fit combinations (given for $T_1 - T_5$ and $R_1 - R_5$) are 0.3, 0.8, 1, 3, and 6 MeV and 20, 11, 6.6, 1.3, and 1, respectively. The maximum energy of the recoil electrons (at which the ratio between the signal intensity and its deviation is unity) is found to be 5.8±0.5 MeV. With an energy of 5.8±0.5 MeV, a recoil electron is produced when an electron scatters an X-ray photon with an energy of 6.1±0.5 MeV, and this electron recoils at 0° (relative to the incident axis of the X-rays). This finding indicates that the maximum energy of these bremsstrahlung X-rays is 6.1±0.5 MeV. Therefore, the cutoff at 6.1 MeV is artificially introduced in the reconstructed X-ray spectrum.

Bremsstrahlung radiation is calculated by considering the first-order perturbation of the wave function for a free electron in a nuclear Coulomb field, which is partially shielded by orbital electrons. This model is applicable for several-megaelectronvolt electrons. Schiff's formula is recognized to be in good agreement with experimental measurements. This formula is used in the MCNP5 code.

The spectrum of the bremsstrahlung X-rays generated by the interaction between the 6 MeV electron bunch and the tungsten plate is calculated using the MCNP5 code. In the simulation, a monoenergetic electron bunch is injected into a 1.5 mm thick tungsten plate along its normal direction. The energy of the injected electron is varied from 5 to 7 MeV, with a 0.5 MeV step in the calculation.

Figure 4-12 shows computed bremsstrahlung X-ray spectra measured by the spectrometer. The cutoff of the spectrum depends on the injected electron energy. Figure 4-12 shows the comparison between the X-ray spectrum reconstructed from the recoil electron distribution shown in Fig.4-11 and the X-ray spectra computed using the MCNP5 code. The reconstructed X-ray spectrum agrees well with spectra calculated for electron energies of 6.0 and 6.5 MeV. This experiment reveals that

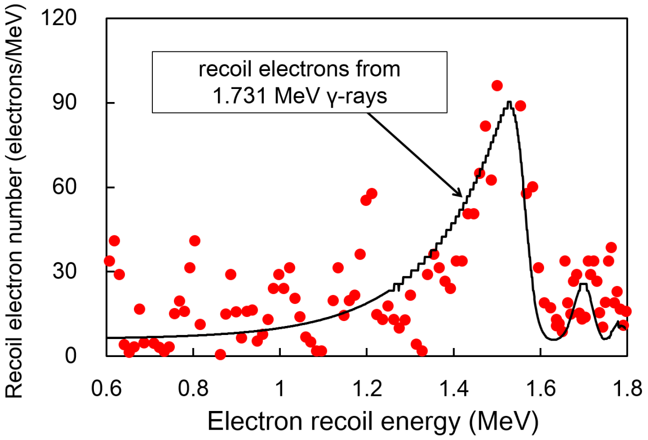

Figure 4-10: Measured recoil electron spectrum (red solid circles) and that calculated (solid line) with the energy resolution of the Compton X-ray spectrometer. The strongest peak appears at 1.508 MeV, which correspond to recoil energy of 1.731 MeV X ray. The energy resolutions of the spectrometer ($\Delta h\nu/h\nu$) was estimated to be 0.077 at 1.731 MeV.

the accuracy of the primary electron energy determination is ±0.5 MeV for 6 MeV electrons.

4.5 | Application of Compton X-ray spectrometer to high-intensity laser-plasma interaction experiment

4.5.1 | Experimental setup

The Compton X-ray spectrometer was used to measure a hard X-ray spectrum generated by high-intensity laser and plasma interactions. Bremsstrahlung X-ray spectroscopy provides quantitative information of the fast electron energy distribution and conversion efficiency. A 200 μm thickness fused silica plate was used as a X ray-electron converter to maximize the detection efficiency. The experiment was performed at the GEKKO-LFEX laser facility at the Institute of Laser Engineering, Osaka University. A Ta cubic block ($1 \times 1 \times 1$ mm^3) was used as a target. An Au cone attached to a hemispherical plastic shell was mounted on the Ta block as shown in Fig.4-13. The distance between the cone tip and the Ta block surface was 50 μm. Three frequency doubled (527 nm of wavelength) GEKKO laser beams that deliver 90 J in total were focused onto the plastic hemispherical shell surface to produce a high-temperature low-density plasma surrounding the Au cone, which mimics the plasma conditions of a fast-ignition integrated experiment. A high intensity pulse from the LFEX laser with 480 J of energy, a wavelength of 1053 nm, a duration of 2 ps was focused at the cone tip to accelerate a fast electron beam. Details of this experimental setup are described in previous paper.[70] A portion of the fast electrons is converted into hard X-rays in the Ta block via the bremsstrahlung process. The hard X-rays were measured simultaneously using the Compton X-ray spectrometer and a DET X-ray spectrometer. Both spectrometers were located at the same angle (20.9°) from the LFEX laser axis. The DET spectrometer consists of a stack of twelve IPs and twelve X-ray filters: 100 μm thick Al, 100 μm thick Ti, 100 μm thick Fe, 100 μm thick Cu, 100 μm thick Mo, 150 μm thick Ag, 500 μm thick Sn, 500 μm thick Ta, 1, 2, 3, and 4 mm thick Pb foils.

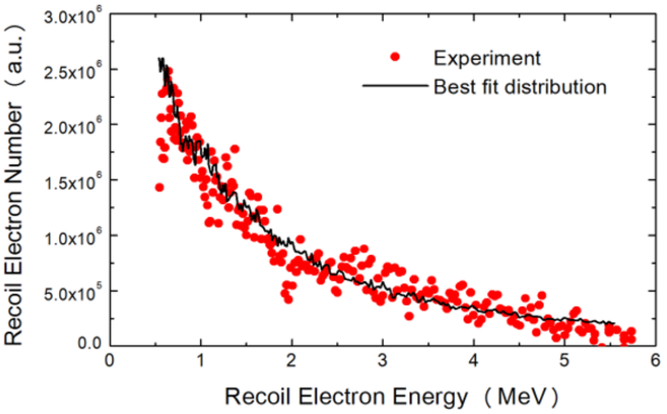

Figure 4-11: Comparison between measured (red dots) and best-fit (black line) spectra of recoil electrons. The X-ray spectrum is reconstructed by finding he best combination of $g(E, T_n)$to fit the measured spectrum of the recoil electrons.

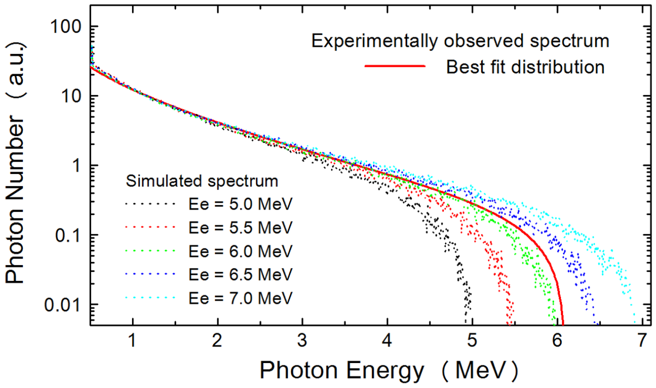

Figure 4-12: Comparison between the X-ray spectrum reconstructed from the re- coil electron distribution and the X-ray spectra computed with the MCNP5 code for 57 MeV monoenergetic electrons. The reconstructed X-ray spec- trum agrees well with spectra calculated for 6.0 and 6.5 MeV electrons.

4.5.2 | Evaluation of absolute x-ray spectrum from recoil electron energy distribution

Figure 4-14 shows the experimental energy distribution of recoil electrons. The error in the electron recoil energy is represented by the energy resolution of the electron energy analyzer. The error of the recoil electron number is represented by a convolution of the statistical fluctuation of the detected electron number (square root of the number of detected photons) and an uncertainty of 17% for the IP response calibration. In this analysis, it was assumed that the X-ray spectrum is a continuum in the energy range between 0.8 and 10 MeV, because electron beams accelerated by laser-plasma interaction generally have a continuum energy distribution. The continuum X-ray spectrum ($f(h\nu)$) was obtained from the measured energy distribution of the recoil electrons. The X-ray spectrum is assumed to be a sum of three Boltzmann distributions (Eq.(4.8)) with three different slope temperatures to simplify the process.

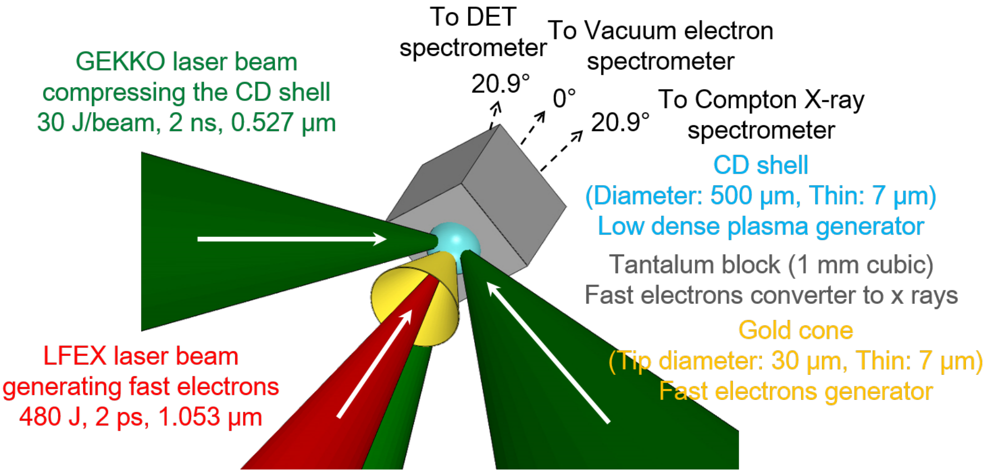

Figure 4-13: Schematic drawing of the laser-plasma interaction experiment. Cone-attached to a hemispherical shell mounted on a Ta block. Fast electrons generated at the cone tip are converted into hard X-rays in the Ta block via the bremsstrahlung process. The hard X-rays were simultaneously observed with the Compton spectrometer and a DET spectrometer, which consists of twelve IPs and twelve X-ray filters. Both spectrometers were installed at the same angle (20.9°) from the picosecond laser pulse axis. The hemispherical shell was irradiated with nanosecond laser beams to generate a high-temperature and low-density plasma surrounding the cone to mimic the plasma conditions of a fast-ignition integrated experiment.

$$f(h\nu) = \sum_{n=1}^{3} R_n \exp\left(-\frac{h\nu}{T_n}\right) \tag{4.8}$$

where $h\nu$, R_n, and T_n are the photon energy, the relative intensity, and the slope temperature, respectively. Possible combinations of R_n and T_n ($n = 1$, 2, and 3) were found to fit $\sum_{n=1}^{3} R_n g(E, T_n)$ with the measured energy distribution of the recoil electrons within the error bars, where $g(E, T_n)$ is an energy distribution of recoil electrons that is produced by Boltzmann spectrum X-ray with a slope temperature of $T_n \ldots g(E, T_n)$ was calculated using the MCNP5 code. All possible X-ray spectra exist in the region bound by the red solid line with circles and the red dashed line with circles shown in Fig.**??**(a). Absolute number of X rays were calculated by taking into account the geometrical consideration of the lead collimator ($\eta_{collection} = 9.94 \times 10^{-7}$), conversion ratio from x rays to recoil electrons ($\eta_{conversion}$) and the detection ratio of recoil electrons ($\eta_{detection}$).

Figure 4-15 shows X-ray doses recorded on each IP layer of the DET spectrometer, where the horizontal axis is the IP order number in the stack. The photostimulated luminescence (PSL) intensities of the IPs are proportional to the energies deposited in the active layer of the IPs. When 1MeV energy deposits in the active layer, the PSL intensity is 0.49±0.13 PSL.23 The dependence of the X-ray doses (PSL unit) on the IP order was compared with Monte Carlo calculations, in which an electron energy distribution $[f(E)]$ is assumed to be the sum of three Boltzmann distributions[Eq. (4.9)].

$$f(h\nu) = \sum_{n=1}^{3} R_n \exp\left(-\frac{h\nu}{T_n}\right) + S\delta(h\nu - 0.511) \tag{4.9}$$

where h_ν, R_n, S and T_n are the photon energy, the relative intensities of continuum X-rays and that of annihilation γ-rays, and the slope temperatures, respectively. $\delta(h\nu)$ in Eq. (4.9) is a delta-like function as $\delta(0) = 1$ and $\delta(h\nu) = 0$ for non-zero values of $h\nu$. The DET detector is

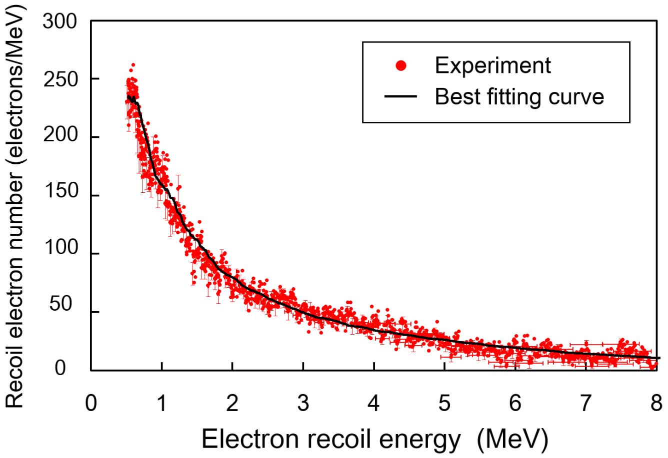

Figure 4-14: Experimental energy distribution (red solid circles) of recoil electrons generated by bremsstrahlung X-rays produced by laser-plasma interactions. The error in the recoil electron energy is represented by the energy resolution of the electron energy analyzer. The error of the recoil electron number is represented by a convolution of the statistical fluctuation of the detected electron number (square root of the number of detected photons) and the IP response calibration uncertainty. The measured distribution from the incident X-ray spectrum was fitted well by the calculated distribution (solid line) within the errors.

sensitive to change of the spectral shape for photon energy below 1 MeV; therefore, annihilation must be considered in this analysis. The GEANT4 code was used to calculate PSL of the N-th IP $[dx(N, T_n)]$ for arbitrary temperature and that of the N-th IP $[(d\gamma(N))$ by annihilation γ-rays. The X-ray spectrum was reconstructed by determining the combination of R_n, S, and T_n to fit the function $[\sum_(n = 1)^3 = R_n d_x(N, T_n) + S d_\gamma(N)(n = 1, 2, 3)]$ within the error of the measured PSL. All possible X-ray spectra were in the region bound by the blue solid lines and triangle marks and blue dashed lines and triangle marks shown in Fig.4-16(b).

From a comparison of the two obtained spectra, the uncertainty of the X-ray spectrum obtained with the Compton X-ray spectrometer is less than that obtained with the DET X-ray spectrometer in the energy range above 5.0 MeV, while the DET spectrometer has less uncertainty in the energy range below 5.0 MeV. The high uncertainty of the Compton X-ray spectrometer is caused predominantly by its low sensitivity.

4.5.3 | Evaluation of absolute energy distribution of fast electrons generated by laser-plasma interaction from absolute Bremsstrahlung x-ray spectrum

Energy conversion efficiency from laser to fast electron after the transport was estimated from the measured absolute number of the bremsstrahlung X-ray photons. The Monte Carlo code (MCNP5) was used to model bremsstrahlung X-ray generation from the fast electron in the 1mm Ta cubic block. Electron beam was injected at 50 μm from block front surface, the electron beam has 30 μm of diameter and 41° of divergence angle (FWHM). Fast electron energy distribution was assumed to have two slope temperatures as

$$F(E) = \sum_{n=1}^{2} A_n \exp\left(-\frac{E}{T_n}\right) \tag{4.10}$$

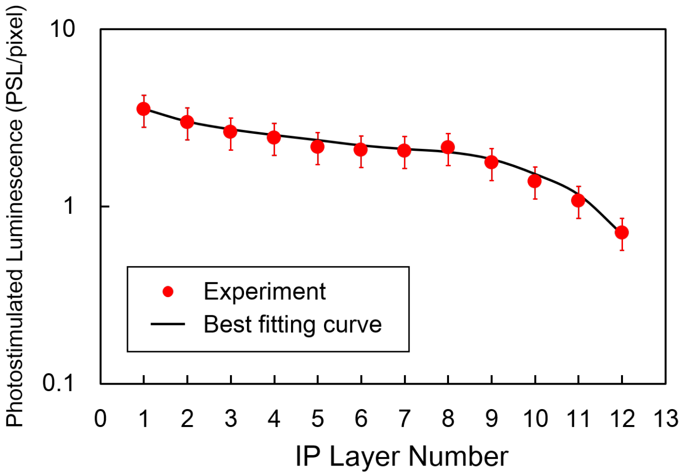

Figure 4-15: Experimental X-ray doses (red solid circles) recorded on IPs in the DET spectrometer with twelve imaging plates and twelve X-ray filters. The solid line represents the calculated doses with best-fits to the measured doses with the values R_1, R_2, R_3, T_1, T_2, T_3, and S.

Combination of A_n and T_n was adjusted to fit a calculate X-ray spectrum with the measured X-ray spectrum within error bars $[\sum_{n=1}^{2} A_n f(E, T_n)]$, here $f(E, T_n)$ is an X-ray spectrum that is produced by fast electron with a slope temperature of T_n. $f(E, T_n)$ was calculated using the MCNP5 code. Slope temperature of high energy component (T_2) was fixed to be 15 MeV that is obtained from the energy distribution of the vacuum electrons in the range of E >10 MeV for reducing indefiniteness of the fitting process.

Figure 4-17 (a) shows evaluated electron energy distributions for the following four cases; [Case A (red solid line)] A_1 = 0.96, A_2 = 0.04, T_1 =1 MeV, T_2 = 15 MeV, and θ_{div} = 41°; [Case B (bule broken line)] A_1 = 0.89, A_2 = 0.11, T_1 =1 MeV, T_2 = 15 MeV, and θ_{div} = 41°; [Case C (green dash-dot line)] A_1 = 0.95, A_2 = 0.05, T_1 =3 MeV, T_2 = 15 MeV, and θ_{div} = 41°; [Case D (purple dot line)] A_1 = 0.95, A_2 = 0.05, T_1 =2 MeV, T_2 = 15 MeV, and θ_{div} = 41°, respectively. The black solid lines shown in Fig. 4-17 (a) represent upper and lower boundaries of possible electron energy spectra. Those four electron energy distributions produce x-ray spectra that agree with the measured bremsstrahlung x-ray spectrum within the error bars as shown in Fig.4-17 (b). The solid black lines in Fig.4-17 (b) represent the upper and lower boundaries of Bremsstrahlung x-ray spectra evaluated with Compton X-ray spectrometer.

Energy conversion efficiencies from laser to fast electrons are summarized in Table I in four example cases. Here, the conversion efficiencies were estimated for all fast electrons (η_{all}) and lower energy component of fast electrons (η_{lower}) were evaluated to be 2.1%-9.7% and 22%-59%, respectively, for $4.7 \times 10^{18}\mathrm{W/cm^2}$ of laser intensity.

4.6 | High Energy X-ray Spectrometer (HEXS)

4.6.1 | Introduction and conversion coefficient

The HEXS spectrometer consists of eight filters of increasing Z, from Al to Ta, then four filters of 1 mm to 4 mm of Pb for differential filtering. And imaging plate (IP) is located in-between each filter HEXS is a stack configuration in which IPs and filters are alternately arranged and superimposed.

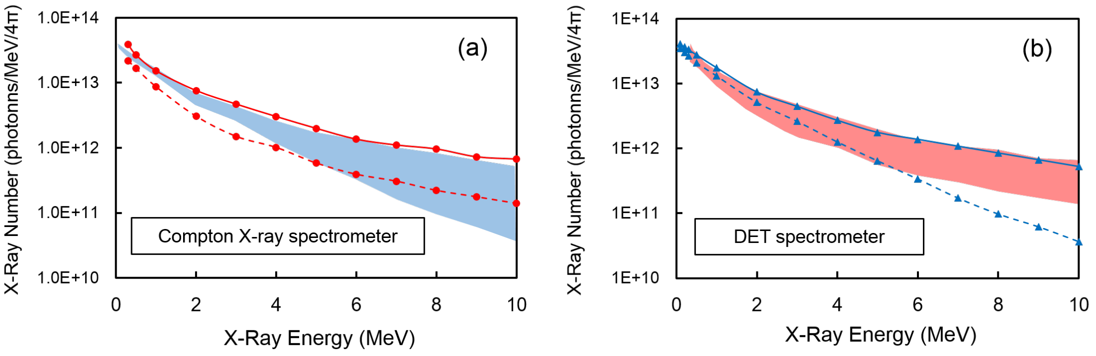

Figure 4-16: X-ray spectra obtained with (a) the Compton X-ray spectrometer and (b) the DET spectrometer. In the photon energy range below 5 MeV, the uncertainty of the spectrum determined with the DET spectrometer is less than that with the Compton X-ray spectrometer, while that determined with the Compton X-ray spectrometer is less than that with the DET spectrometer in the energy range above 5 MeV. The high uncertainty of the Compton X-ray spectrometer is caused predominantly by its low sensitivity.

Table 4.1: Conversion efficiencies into all components electrons and lower energy components electrons for fast electron spectra previously described.

Case	A_1	T_1 (MeV)	η_{all}	η_{lower}
A	0.96	1	39	3.7
B	0.89	1	59	2.1
C	0.95	2	28	7.0
D	0.95	3	22	9.7

Schematic drawing of the HEXS is shown in Fig.4-18(a). Each metal filter has different energy thresholds of X-ray absorption. X-ray sensitivity curves of each IP of HEXS are shown in Fig.4-19. The response of the filter stack, including all configuration (Teflon layer, metal lters, Mylar film, and layer configuration of the IP) was modeled by the GEANT4 Monte Carlo code. As can be seen from the figure, the IP behind a a low-Z filter (such as Al), has wide sensitivity from relatively low energy X-rays of about 10 keV to high energy X-rays.The IP behind a a high-Z filter (such as Pb) responses only high-energy X-rays of several hundred keV or more.

IP has high sensitivity, high spatial resolution and high dynamic range. IP, however, is light sensitive and signals of IP fade with time. The most sensitive type of IP (Fuji BAS-MS) was chosen. A 250 μm thickness of Mylar film taped to both faces of each the filter to minimize the contribution of secondary electrons ($<$ 150 keV) generated at the metal filter.

The LFEX chamber is a high noise environment, with electrons and x-ray coming from other diagnostics, the chamber wall and the experimental room wall. Shielding, collimation, and magnetic deflection are all necessary to prevent background contribution. The stack of IPs and filters is contained in a Teflon container and covered with lead shield (2 cm thickness) with X-ray collimator (10 cm length , 1 cm diameter) (shown in Fig.4-18(b) and (c)). This configuration is possible to shield high-energy X-rays by the lead shield, and to shield secondary electrons by Teflon container. A cleanup magnet with a maximum magnetic flux density of 1 T is located at the head of the spectrometer to exclude fast electrons from the diagnostics line.

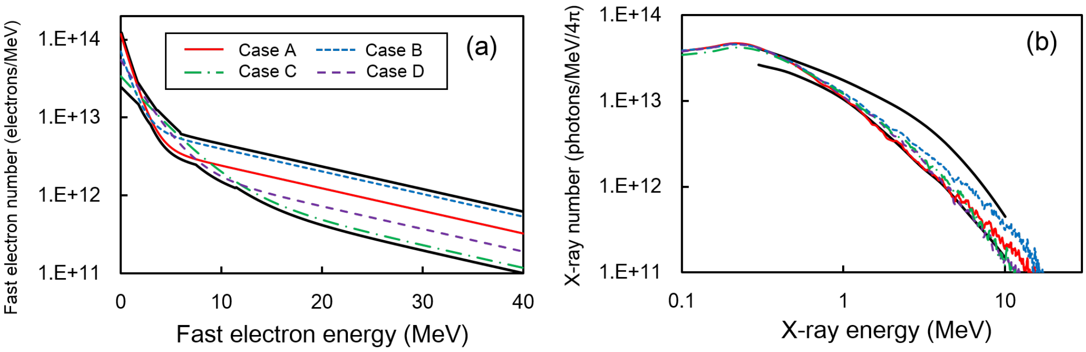

Figure 4-17: Fast electron spectra that reproduces absolute X-ray spectra obtained with Compton X-ray spectrometer represented by black solid lines shown in Fig.4-16 (a). A sample subset of allowed energy distributions are represented by the color lines for the following four cases; [Case A (red solid line)] $A_1 = 0.96$, $A_2 = 0.04$, T_1 =1 MeV, T_2 = 15 MeV, and θ_{div} = 41 °; [Case B (bule broken line)] $A_1 = 0.89$, $A_2 = 0.11$, T_1 =1 MeV, T_2 = 15 MeV, and θ_{div} = 41 °; [Case C (green dash-dot line)] $A_1 = 0.95$, $A_2 = 0.05$, T_1 =3 MeV, T_2 = 15 MeV, and θ_{div} = 41 °; [Case D (purple dot line)] $A_1 = 0.95$, $A_2 = 0.05$, T_1 =2 MeV, T_2 = 15 MeV, and θ_{div} = 41 °, respectively.

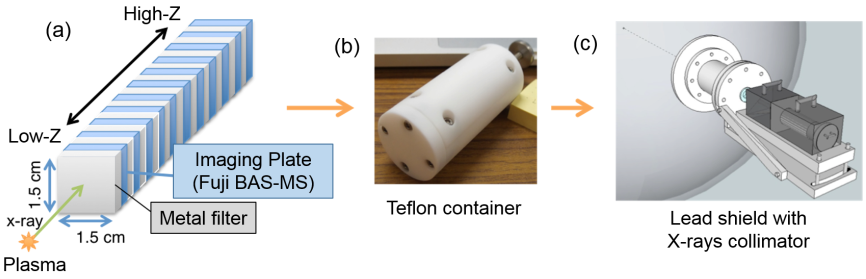

Figure 4-18: (a) Stack configuration (b) The stack is contained in a Teflon container and (c) covered with lead shield with X-ray collimator. Figure taken from Takuya Namimoto, *master's thesis* (2013).

The HEXS was calibrated by bremsstrahlung X-rays generated by quasi mono-energetic electron accelerated by linear accelerator. Figure 4-20(a) shows experimental layout at LINAC facility. One-hundred of electron bunches, irradiated to a 5 mm thickness lead planar target. And emitted X-rays were measured by two HEXSs located at different angles. According to the current signal of the Faraday cup, ten of electron bunches include 185.0 nC of electric charge. The value means that single electron bunch includes 1.155×10^{11} of electrons. Spot size of electron bunch was 4 mm at the target position.

The imaging plates were scanned on the Typhoon FLA-7000 image plate scanner. The scanner parameters were a scan time exactly 40 minutes after the start of exposure, and scanner settings of 25 μm pixel size, 600 V voltage of a PMT, and L5 dynamic range. Figure 4-20(b) shows recored signal on each IP. The signals recorded on the $1\times$ 1 cm^2 portion from the center of the 1.5×1.5 cm^2 imaging plate were extracted. An averaged value per pixel (PSL/pixel) of each IP is shown in Fig.4-20(c) as experimental values.

The response of the filter stack for bremsstrahlung X-rays emitted from target was calculated by the GEANT4 Monte Carlo code. The filter configuration and three dimensional placement of HEXSs and the target, were considered in the simulation. For the electron source in the simulation,

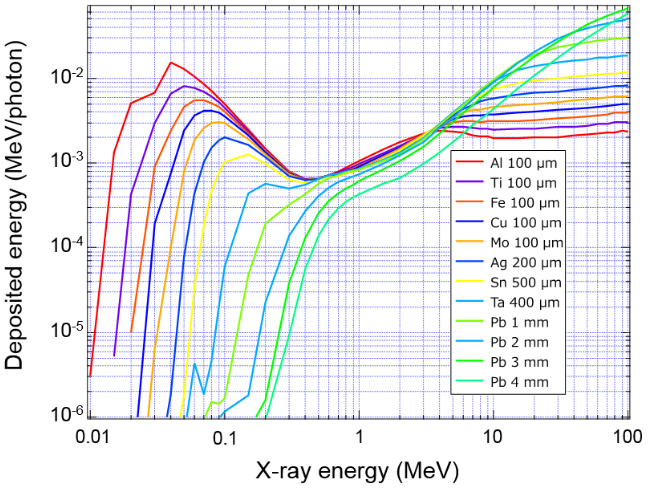

Figure 4-19: X-ray sensitivity curves of each IP of HEXS Figure taken from Takuya Namimoto, *master's thesis* (2013).

energy and the spot diameter of experimental conditions were used in the simulation. However, to shorten the calculation time, the number of electrons was reduced to 1/100 of the number of electrons as the actual. (Thus the output signal was increased to 100 times.) An averaged value per pixel (MeV/pixel) of each IP is shown in Fig.4-20(c) as simulated values.

Table 4.2: Conversion coefficients between the deposited energy [MeV] on the IP on simulation and the signal intensity [PSL] output from the IP reader

IP layer	15 degree	30 degree
IP1	2.03	1.81
IP2	1.84	1.80
IP3	1.95	1.70
IP4	1.88	1.73
IP5	1.91	1.84
IP6	1.94	1.96
IP7	1.93	2.03
IP8	2.00	1.97
IP9	2.01	2.04
IP10	2.51	2.34
IP11	2.53	2.65
IP12	2.58	2.25
Ave.	2.05 ± 0.19	

The simulated values match up quite well with the experimental values. In this Fig.4-20(c) the circle points are the measured dose on the imaging plates and the cross points represent the predictions of the Monte Carlo model. From comparing these two values, the conversion coefficient between the deposited energy [MeV] on the IP on simulation and the signal intensity [PSL] output from the IP reader are estimated. For the measured PSL levels to be proportional to the calculated deposited energy, these conversion coefficients, in units of MeV/PSL, must be the same for every calibration point. These conversion coefficients are shown in Table4.2.

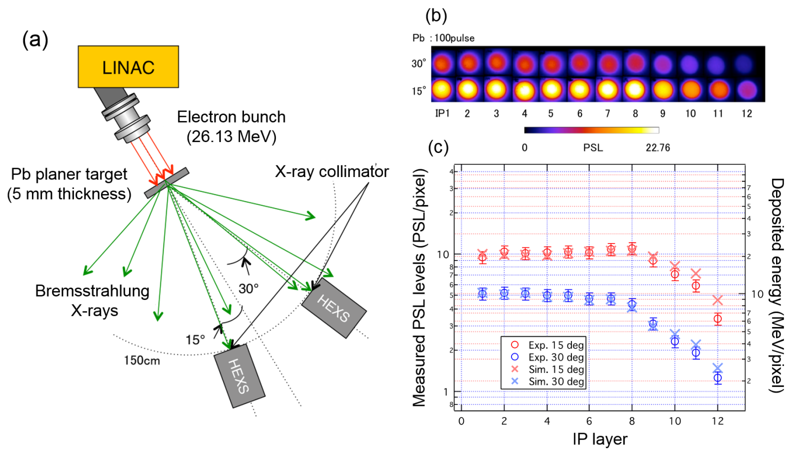

Figure 4-20: X-ray sensitivity curves of each IP of HEXS calculated by GEANT4. Each curve represents the energy deposited on each IP by the photon spectrum. Figure taken from Takuya Namimoto, *master's thesis* (2013).

As shown in Table4.2, the average value of all imaging plates was 2.05 [MeV/PSL]. Moreover, the conversion coefficient calculated from each IP has a distribution centered on 2.05. The center value 2.05 was subtracted from the conversion coefficient calculated from each IP, and calculating the average value of error from its absolute value was 0.19. Thus, 19.4% of the signal value, which is derived by (0.19/2.05 × 100) × 2, will be used as the error bar of the signal. In the this these, we decided to obtain the absolute amount of X-rays using this conversion coefficient of 2.05 ± 0.19 [MeV/PSL].

4.6.2 | Estimation of energy distribution of relativistic electron beam

In this section, we describe a method for estimating the energy efficiency from laser to electron from the signal recorded on twelve IPs of HEXS.

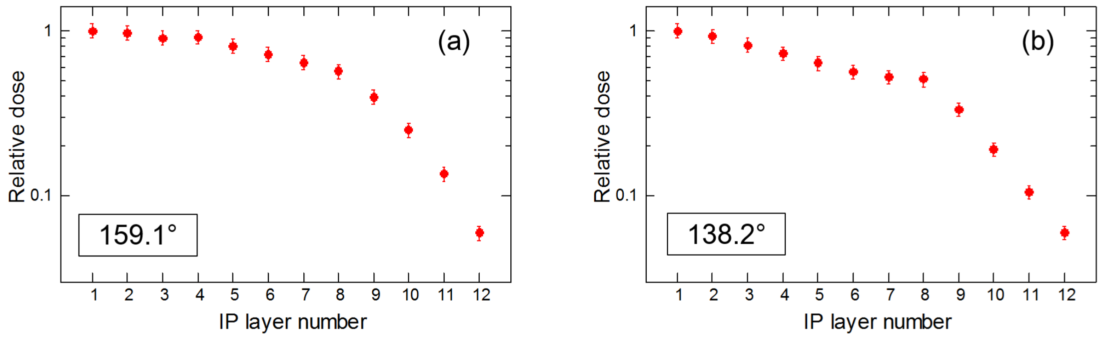

Figure 4-21: Relative x-ray doses recorded on imaging plates in HEXSs located at (a) 159.1°, and (b) 138.2° from REB injecting axis.

Figure 4-21 shows the relative x-ray doses (red solid circles) recorded on imaging plates in HEXSs located at different angles. The signals are normalized so that the signal of the first layer of HEXS is 1. The error bar of the relative x-ray doses was defined as 19.4% of the signal value. The derivation of this error bar was explained in the previous section. This error bar include all the errors to be considered in comparing the experiment and modeling, such as the statistical fluctuation of the detected electron number and the uncertainty of IP response calibration. Here we define the relative x-ray doses experimentally observed as a matrix denoted $D^{exp}_{1,M}$, where M is IP layer number ($M =$ 1, 2,..., 12).

The dependence of the doses on the IP order in the stack was compared with Monte Carlo calculations. In our analysis, it was assumed that the relativistic electron beam (hereinafter referred to as REB) energy distribution is a continuum in the energy range between 0.3 and 10 MeV, because electron beams accelerated by laser-plasma interaction generally have a continuum energy distribution. The electron energy distribution is assumed to be a sum of two Boltzmann distributions (Eq. (4.11)) with two different slope temperatures (T_{REB1}, T_{REB2} and $T_{REB1} < T_{REB2}$) to simplify the process, namely

$$f(E) = A\exp\left(-\frac{E}{T_{REB1}}\right) + (1-A)\exp\left(-\frac{E}{T_{REB2}}\right), \tag{4.11}$$

and a single divergence angle (θ_{div}) of the REB were assumed. Here $A$and E are the relative coefficient and the electron kinetic energy, respectively.

Energy distribution of the vacuum electrons, which escape from the target block into vacuum, was measured with an electron energy analyzer. Slope temperature of higher energy component (T_{REB2}) was obtained by fitting the energy distribution of the vacuum electrons with the function [$\exp(-E/T_{REB2})$] for reducing indefiniteness of the fitting process. The lower energy component (T_{REB1}) cannot be obtained from the vacuum electron distribution, because the sheath field generated at the metal block surfaces affects strongly motion of the low-energy REB. Hard x-ray spectrum was used to obtain T_{REB1} inside the target block.

The dependence of the dose on the IP order in the stack recorded by the hard x ray generated by REBs with different slope temperatures was calculated by Monte Carlo simulation. The computed results were summarized as a lookup table in the energy range between 0.3 and 10 MeV.

Figure4-22 shows a part of this table. This table shows the response of each IP stack of HEXSs to hard x ray generated when REBs with different slope temperature enter the 1 mm cubic gold block. Fig.4-22(a) shows the response observed at 159.1° from the electron incident axis.Fig.4-22(b) and (c) show the response observed at 138.2° and 110.9°, respectively. It can be seen that when REBs with the higher slope temperature are injected, the more signals are recorded on the IPs behind the stack.

Note: these signals were normalized so that the signal of the first layer is 1 in order to compare the difference due to incident electron energy. The value of the actual lookup table used the value before normalization processing. Parameters of the REBs incident into the target in the Monte Carlo simulation are defined by the slope temperature, the divergence angle, and the particle number of REBs. When the particle number and divergence angle are fixed and the slope temperature is increased 5 times, the total energy of REBs increases by 5 times. Therefore, the value of the lookup table increases as the slope temperature increases.

Here we define the value of the lookup table as a matrix denoted $S^{cal}_{N_{REB},M}$, where N_{REB} and M are slope temperatures of REBs ($N_{REB} = 1$ (0.3 MeV), 2 (0.4 MeV),..., 970 (10 MeV)) and IP layer number ($M =$ 1, 2,..., 12).

Using this matrix $S^{\mathrm{cal}}_{N_{REB},M}$ representing the response of the IP stack for REBs with single slope temperature, the response for REB with two slope temperatures $d^{\mathrm{cal}}_{N_{REB},M}$, it can be defined as $d^{\mathrm{cal}}_{N_{REB},M} = AS^{\mathrm{cal}}_{N_{REB},M} + (1-A)S^{\mathrm{cal}}_{N_{REB2},M}$, where N_{REB2} denotes the row number corresponding to the high temperature component T_{REB2} of the electron observed by the electron energy analyzer.

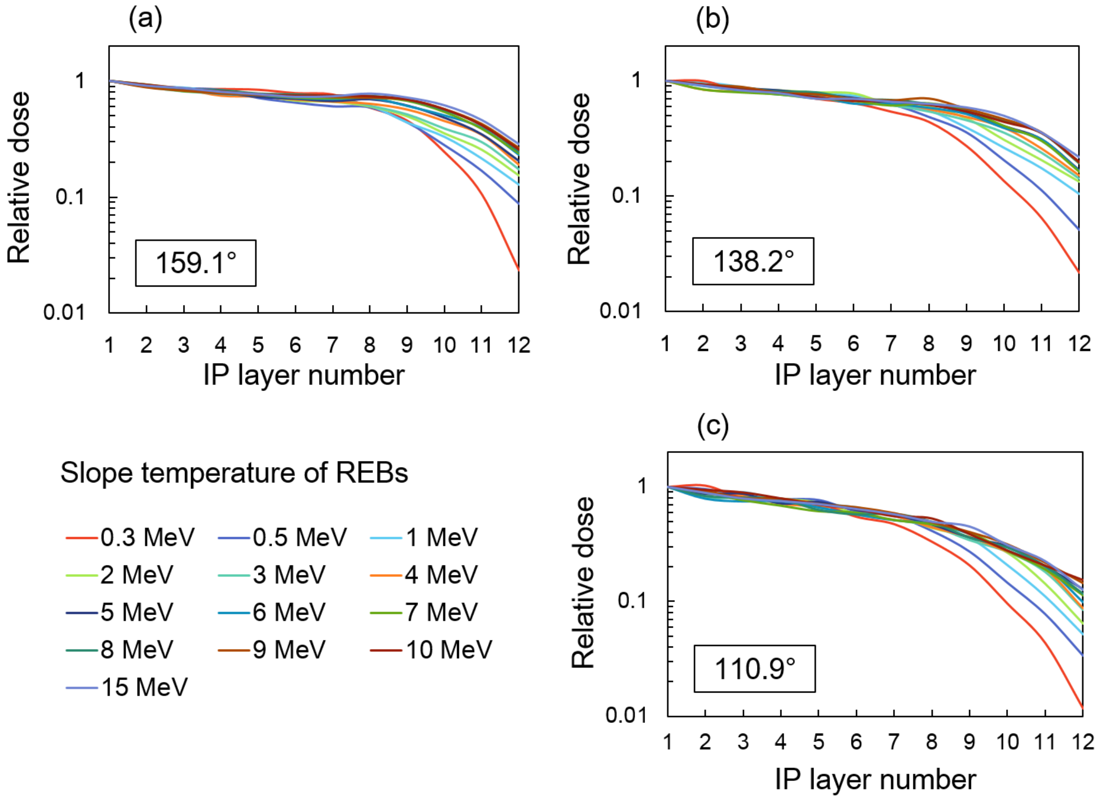

Figure 4-22: Lookup table of dose on the IP order in the stack in the energy range between 0.3 and 15 MeV.

After normalization process, it is deafened as,

$$D^{\text{cal}}_{N_{REB},M} = \frac{AS^{\text{cal}}_{N_{REB},M} + (1-A)S^{\text{cal}}_{N_{REB2},M}}{AS^{\text{cal}}_{N_{REB},1} + (1-A)S^{\text{cal}}_{N_{REB2},1}}. \tag{4.12}$$

In the analysis program, A is changed from 0 to 1 at 0.01 intervals, and N_{REB} is changed from 1 to 970 (This corresponds to changing from 0.3 to 10 MeV at 0.1 MeV intervals.), and the experimental stack response $D^{\text{exp}}_{1,M}$, and the calculated stack response $D^{\text{cal}}_{N_{REB},M}$ are compared. When a calculated stack response was included in the range of the error bar of the experimental stack response, it was judged that both were matched. This judgment condition can be written as

$$(1-0.097)\cdot D^{\text{exp}}_{1,M} \leq D^{\text{cal}}_{N_{REB},M} \leq (1+0.097)\cdot D^{\text{exp}}_{1,M}. \tag{4.13}$$

This judgment process was performed for twelve IPs equipped in single HEXS. If there are more than one HEXSs, these process was performed for all IPs.

Figure4-23 shows results of the judgment process described above. In this case, we had two HEXSs located at 159.1°, and 138.2° from the REB injecting axis. The color map of Fig.4-23 shows number of matching IP. Maximum number was found in the area of $(A, T_{REB1} = (0.8-1, 0.3-0.5)$. In this area, 17 of 24 IPs match.

4.6.3 | Estimation of energy conversion efficiency

In the sec.4.6.2, we described a method to estimate the energy distribution of REB incident on the target. In the this section, we describe a method to estimate the number of REs incident on

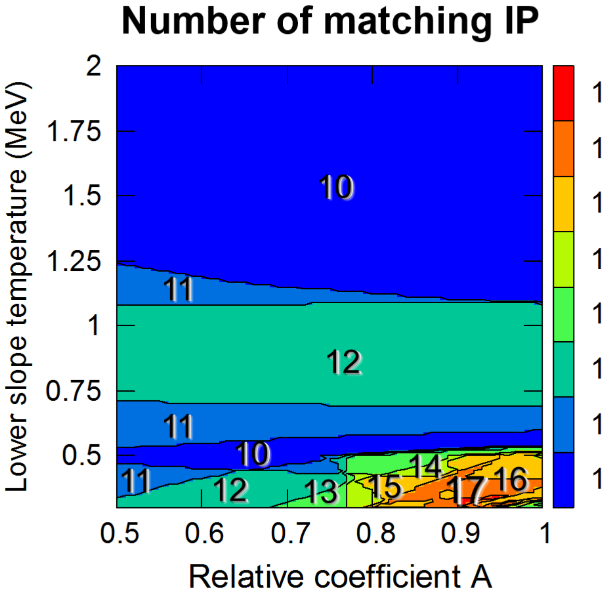

Figure 4-23: Results of the judgment process. The color map shows number of matching IP. Maximum number was found in the area of $(A, T_{REB1} = (0.8-1, 0.3-0.5)$. In this area, 17 of 24 IPs match.

the target by comprehensively analyzing multiple IPs provided from multiple HEXSs. Moreover, we describe a method for estimating energy conversion efficiency from relativistic intensity laser to REB.

Experimental data

When IP obtained by experiment is read by IP scanner, digital data is saved. In this digital data, PSL which is a unit specific to the GE scanning system is used to linearize the image value. This PSL value has dependency on scanner's setting parameter and is represented by

$$\mathrm{PSL} = \frac{Counts^{\mathrm{exp}}}{100000}\left(\frac{R_{\mu m}}{100}\right)^2 h(V) 10^{L/2}, \tag{4.14}$$

where $R_{\mu m}$ is the spatial resolution in μm, L is the dynamic range latitude (either 4 or 5 orders of magnitude), and $Counts^{\mathrm{exp}}$ is the scanned image value (signal value of raw data). The sensitivity function, $h(V)$, is an empirical relation found by solving Eq. (4.14), using the known image plate response in PSL, and it is represented by [68]

$$h(V) = 0.092906 + 1370.8\mathrm{e}^{-0.014874 \cdot V} + 654.24\mathrm{e}^{-0.011026 \cdot V}, \tag{4.15}$$

Since the conversion coefficient between PSL (which is a unit of digital file) and MeV (which is a unit of absorbed dose) is derived, it is not necessary to obtain the signal value of raw data by using the above equations. However, care must be taken that PSL is a value that depends on scanner settings as described above. In this study, the scanner parameters are set as $R = 25$ μm, $V = 600$ V, $L = 5$ at all readings. It should be noted that the conversion coefficient are valid only with these limited parameters.

Since the reading by the reader is 40 minutes after the experiment, true experimental data is obtained by considering the fading of the signal occurring in the time there between (by dividing the value of this matrix by 0.93). [71, 72] Here, we define this experimental data as a matrix that can be represented by $d^{\mathrm{exp}}_{1,N}$. The unit of this matrix data is PSL/pixel. Data obtained by normalizing this matrix by the value of the first IP layer is the matrix of $D^{\mathrm{exp}}_{1,N}$ that used for analysis in the sec.4.6.2

Simulated data

The simulated data $Counts^{\mathrm{cal}}$ can be obtained by Monte Carlo simulation where the three-dimensional arrangement of HEXS with respect to the electron incident axis is considered. In the simulation box, three dimensional angles are consistent with the that of the experiment, but the distance between the target and HEXSs is set to be shorter than the actual distance to reduce calculation time.

Therefore, there is a conversion coefficient that considers these solid angle efficiencies between the value of the lookup table described in the previous section and the value actually obtained in the Monte Carlo simulation, and these relational expression is represented by

$$S^{\mathrm{cal}}_{N_{REB},M} = 2.05 \cdot \left(\frac{0.45}{3.818}\right)^2 \cdot \left(\frac{25 \times 10^{-6}}{1.5 \times 10^{-2}}\right)^2 \cdot Counts^{\mathrm{cal}}, \tag{4.16}$$

2.05 on the right side is the conversion efficiency from MeV to PSL described in the previous section. The rest are coefficients to consider the solid angle efficiency. The first half is a coefficient that takes into consideration the distance between simulation and actual target and HEXS and the second half is a coefficient that converts the energy given to the whole IP into energy per unit pixel of 25 μm × 25 μm.

Using this matrix $S^{\mathrm{cal}}_{N_{REB},M}$ representing the response of the IP stack for REBs with single slope temperature, the response for REB with two slope temperatures $d^{\mathrm{cal}}_{N_{REB},M}$, it was defined as $d^{\mathrm{cal}}_{N_{REB},M} = AS^{\mathrm{cal}}_{N_{REB},M} + (1-A)S^{\mathrm{cal}}_{N_{REB2},M}$.

Total number of REs

By comparing experimental values and simulated values, it is possible to estimate the total number of REs generated by relativistic intensity laser plasma interaction. The total number of REs $Num^{\mathrm{all}}_{N_{REB},M}$ is obtained by

$$Num^{\mathrm{all}}_{N_{REB},M} = \left[\frac{1}{12}\sum_{M=1}^{12}\left(\frac{d^{\mathrm{exp}}_{1,M}}{d^{\mathrm{cal}}_{N_{REB},M}}\right)\right] \times 10^9, \tag{4.17}$$

using the matrix defined so far. The 10^9 on the right side is derived from the 10^9 of electrons that used to obtain simulated data in the Monte Carlo simulation. $\sum$ is derived from taking an average for 12 IPs equipped in single HEXS. If we have c of HEXSs, we take an average for the $12 \times c$ of IPs.

Energy conversion efficiency (CE)

The energy conversion efficiency to the low energy component (T_{REB1}) can be obtained as

$$\mathrm{CE}^{\mathrm{lower}} = \frac{T_{REB1}(\mathrm{MeV}) \cdot Num^{\mathrm{all}}_{N_{REB},M} \cdot F(T_{REB1}, T_{REB2}) \cdot 1.602 \times 10^{-19} \cdot 10^6}{\text{Laser Energy (J)}} \cdot 100, \tag{4.18}$$

by using the formulas so far. Here, the function $F(T_{REB1}, T_{REB2})$ indicates the proportion of energy that is carried by low energy component among the total energy, which is expressed as

$$F(T_{REB1}, T_{REB2}) = \frac{\int_0^\infty A\mathrm{e}^{-E/T_{REB1}}\mathrm{d}E}{\int_0^\infty A\mathrm{e}^{-E/T_{REB1}} + (1-A)\mathrm{e}^{-E/T_{REB2}}\mathrm{d}E}. \tag{4.19}$$

The energy conversion efficiency to the all energy component (T_{REB1} and T_{REB2}) can be obtained as

$$\mathrm{CE}^{\mathrm{both}} = \frac{T_{REB1}(\mathrm{MeV}) \cdot Num^{\mathrm{all}}_{N_{REB},M} \cdot 1.602 \times 10^{-19} \cdot 10^{6}}{\text{Laser Energy (J)}} \cdot 100. \tag{4.20}$$

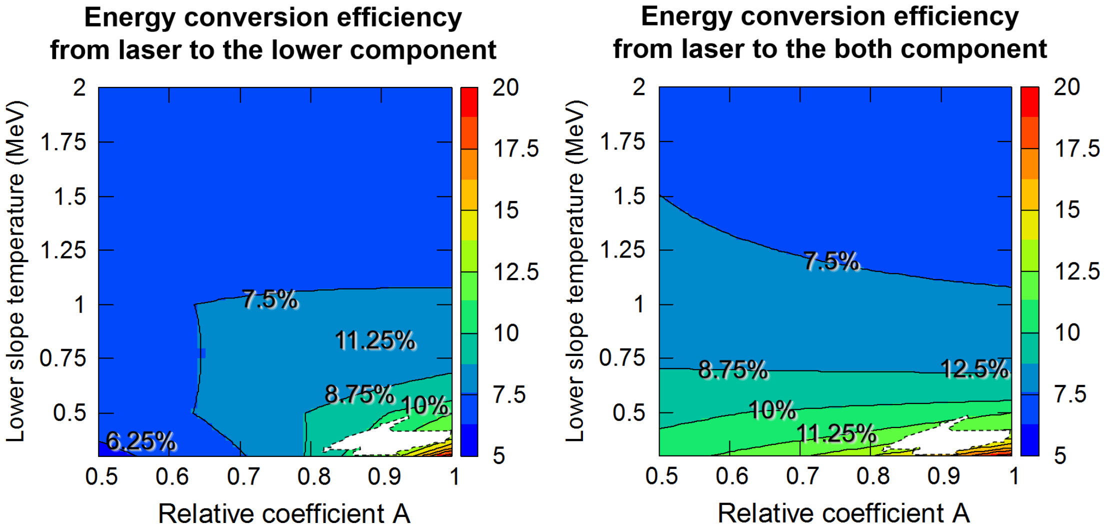

Figure 4-24: (a) energy conversion efficiency from the laser to electrons of lower energy component that obtained by Eq.(4.18). (b) energy conversion efficiency from the laser to the electrons of both components that obtained by Eq.(4.20). The white-painted area in the both figure, shows the area where the coincidence rate between the experimental value and simulation value was high obtained in the previous section .

The color map in Fig.4-24 (a) shows the energy conversion efficiency from the laser to electrons of lower energy component that obtained by Eq.(4.18). The color map in Fig.4-24 (b) shows the energy conversion efficiency from the laser to the electrons of both components that obtained by Eq.(4.20). The white-painted area in the both figure, shows the area where the coincidence rate between the experimental value and simulation value was high obtained in the sec.4-21.

By comparing the white-painted area with the color maps, we can read the conversion efficiency from Fig.4-24. In this experiment, HEXSs' signal indicated that 8.75-12% of the laser energy was converted to REs of lower energy component, and 11-17.5% of energy was converted to REs of both components.

4.7 | Conclusion

First half of this chapter reported the development of the Compton X-ray spectrometer that is applicable to high intensity laser-plasma interaction experiment. A Compton X-ray spectrometer was developed for high energy resolution single-shot high-flux hard X-ray spectroscopy in a high intensity laser-plasma interaction experiment. High energy resolution can be obtained by optimization of the X ray-electron converter thickness and the use of a magnet-based energy analyzer. The conversion efficiency from photons to recoil electrons is proportional to the areal density of the converter. The electron energy distributions increase rapidly when the areal density of the converter is close to 1/10 of the maximum range of the recoil electrons. The energy resolution of the Compton X-ray spectrometer ($\Delta h\nu/h\nu$) was evaluated using mono energetic γ-rays (1.1732 and 1.3325MeV) emitted from a ^{60}Co radioactive isotope and laser-Compton scattering X ray (1.731 MeV). The energy resolution was sufficiently high to resolve the two distinct γ-ray peaks at 1.1732 and 1.3325 MeV. The energy resolution ($\Delta h\nu/h\nu$) was evaluated to be 0.085 at 1.1732 MeV, 0.093 at 1.3325 MeV and 0.077 at 1.731 MeV. The energy resolution of the recoil electron energy analyzer is given by ($\Delta E/E$). ΔE was represented by a convolution of the energy distribution (ΔE_{col}) caused by multiple collisions in the converter and the energy resolution of the electron energy analyzer, which is determined by the slit width of the analyzer (ΔE_{slit}). The Compton X-ray spectrometer was used to measure bremsstrahlung X-rays generated by high intensity laser-plasma interactions, and the spectrum was in reasonable agreement with that obtained using a DET spectrometer. In the photon energy range above 5 MeV, a smaller uncertainty of spectral intensity was obtained with the Compton X-ray spectrometer compared with that obtained with the DET spectrometer. A lower uncertain of spectral intensity could also be obtained by increasing the photon flux. The energy conversion efficiencies from laser to all fast electrons and lower energy component of fast electrons are evaluated to be 2.1%-9.7% and 22%-59%, respectively, for 4.7×10^{18}W/cm^2 of laser intensity.

In second half of this chapter, we described the estimation method of the average energy and the energy conversion efficiency of relativistic electrons by spectral reconstruction of hard x-rays measured by High Energy X-ray Spectrometer which is one of DET X-ray spectrometers. Although this spectrometer is inferior to the Compton spectrometer on energy resolution, it has high sensitivity. The reason for this is that the Compton spectrometer measures via converting X-rays into recoil electrons, while HEXS directly observes x-rays by the IP. Since energy resolution of single HEXS is low, we can not estimate the energy conversion efficiency and the average energy of electrons by only single HEXS. However, hard X-ray spectrum measurement with multiple HEXSs surrounding the target can increase the accuracy of estimation of conversion efficiency and average energy. The signals recorded on the IPs of these HEXSs are comprehensively analyzed using Monte Carlo simulation considering three dimensional hard x-ray radiation distribution. We described a method of estimating the average energy of relativistic electrons and energy conversion efficiency by spectral reconstruction of hard X-rays observed by multiple HEXSs.

CHAPTER 5

Beyond scaling acceleration of relativistic electrons due to LFEX pulse extension

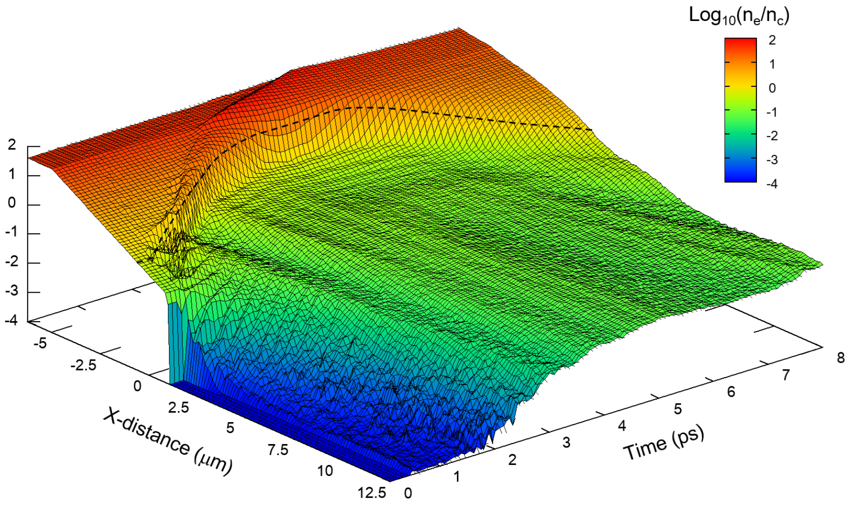

5.1 | Introduction

When a high-intensity laser pulse is irradiated on a material, its surface is instantaneously ionized, and the electrons in the ionized material, namely, plasma, are then accelerated close to the speed of light by the ponderomotive force of the laser light. These energetic electrons are often called relativistic electrons (REs). The energy distribution of REs (dN/dE) is approximated by a Maxwell-Boltzmann distribution function with a slope temperature (T_{RE}) as $dN/dE \propto \exp{(-E/T_{\mathrm{RE}})}$. Several scaling laws of the slope temperatures that depend on laser intensities had been investigated experimentally [73, 29, 31], theoretically, and computationally [8, 74, 75, 76].

These scaling laws are useful to quickly determine laser parameters for high-intensity laser experiments and applications because particle-in-cell (PIC) simulations are computationally expensive. Although the interaction time-scale, namely the pulse duration is not considered in the reported scaling laws, recent computational and theoretical studies [77, 78] have revealed that a slope temperature generated by multi-picosecond laser pulses is much higher than that from the reported scaling laws. We have identified that the following two acceleration mechanisms are essential for generation of the high energy component of the energy distribution of REs in multi-picosecond laser plasma interaction experiments.

Sorokovikova *et al.* [78] reported the generation of energetic REs by the combination of a laser field and a quasi-static electric field. In laser-generated plasmas, the quasi-static electric field is generated spontaneously by the charge separation at the forward edge of the plasma expansion, and the direction of this field is generally parallel to the direction of laser propagation. The quasi-static electric field, which in multi-picosecond laser-plasma interaction, is capable to push electrons along the laser light, so that electrons can stay in the acceleration phase longer, namely, getting higher energy gain.

Krygier *et al.* [79] investigated multiple electron injection in the region where the laser field and quasi-static electric field coexisted due to the cyclotron motion of REs in a self-generated quasi-static azimuthal magnetic field. This distinctive injection mechanism is referred to as loop-injected direct acceleration (LIDA). The quasi-static magnetic field also develops with time during laser-plasma interaction, and the LIDA plays a significant role in the generation of energetic REs around several picoseconds after laser-plasma interaction begins.

5.2 | Experimental and computational results of energy distribution of relativistic electrons

We have experimentally investigated the dependence of RE energy distributions on the pulse durations under the condition that is free from pre-plasma formation. The experiment was conducted using an LFEX laser system at Institute of Laser Engineering, Osaka University. The LFEX consists of four beams. One chirped seed light is divided into four laser beams that are amplified in four amplifier chains. The amplified beams are compressed temporally by four sets of gratings, and they are focused on a target by one $F/10$ off-axis parabolic mirror. The spot diameter of the spatially overlapped LFEX beams on a target was 70 μm of the full width at half maximum (FWHM), and 30% of the laser energy was contained in this spot. One LFEX beam delivered 300 J of 1.053 μm wavelength laser light with a 1.2 ps duration (FWHM), and the peak intensity of one beam was 3.4×10^{18} W/cm^2. LFEX laser pulses can be stacked temporally with arbitrary delays between the beams. In this study, a single beam (Case A: 1.2 ps FWHM of pulse duration and 3.4×10^{18} W/cm^2 of peak intensity) was used and two types of four stacked beams (Case B: 4.0 ps FWHM of pulse envelope and 4.3×10^{18} W/cm^2 of peak intensity, and Case C: 1.2 ps FWHM of pulse duration and 1.36×10^{19} W/cm^2 of peak intensity).

A plasma mirror (PM) was implemented to realize the pre-plasma-free condition to conduct a well-defined experiment. The intensity contrast ratio of the LFEX laser pulse on a target was better than 10^9 at 1 ns before the main pulse irradiation without the PM. This contrast ratio is improved by two orders of magnitude with implementation of the PM [80]. These "clean" pulses were focused on a 1 mm^3 gold cube. A clean intense laser pulse enables the RE acceleration mechanism to be examined with an inherent plasma formed by the main laser pulse itself in the picosecond time range. The density scale length of the preformed plasma was calculated to be 1.5 μm at 10 ps before the

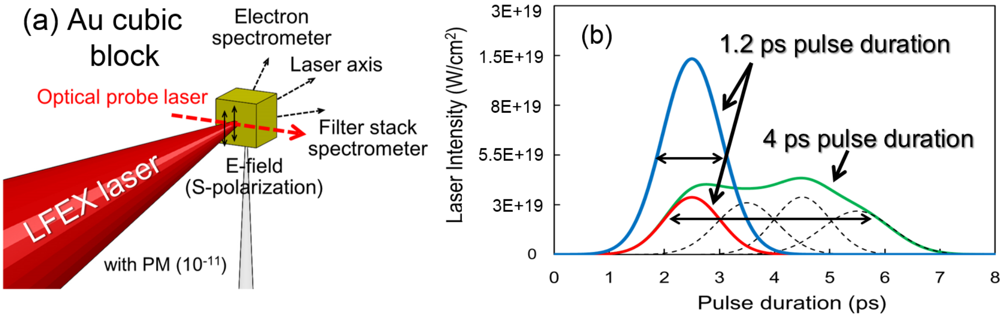

Figure 5-1: (a) Experimental setup. The "clean" LFEX pulses were focused on a 1 mm^3 gold cubic block. One LFEX beam delivered 300 J of 1.053 μm wavelength laser light with a 1.2 ps duration (FWHM), and the peak intensity of one beam was 3.4×10^{18} W/cm^2. (b) Temporal profile of laser pulses. LFEX laser pulses can be stacked temporally with arbitrary delays between the beams.

intensity peak using a two-dimensional radiation hydrodynamics simulation with the PINOCO-2D code [81].

The energy distribution of REs emanated from the target to vacuum was measured with an electron energy analyzer located 20.9° from the incident axis of the LFEX beams. Figure 5-2(a) shows the experimental results of the time-integrated energy distribution. The slope temperatures were 0.65 MeV for case A (red circles) and 1.7 MeV for case B (green triangles). The slope temperature for case B was twice that for case A, even though the peak intensities were the very close. We emphasize here that the energy distributions of REs obtained for case B and case C were almost identical, even though the peak intensities were different by a factor of four. These slope temperatures cannot be explained using the reported scaling laws [8, 29, 74], whereby the dependence of the slope temperature on the pulse duration is not considered.

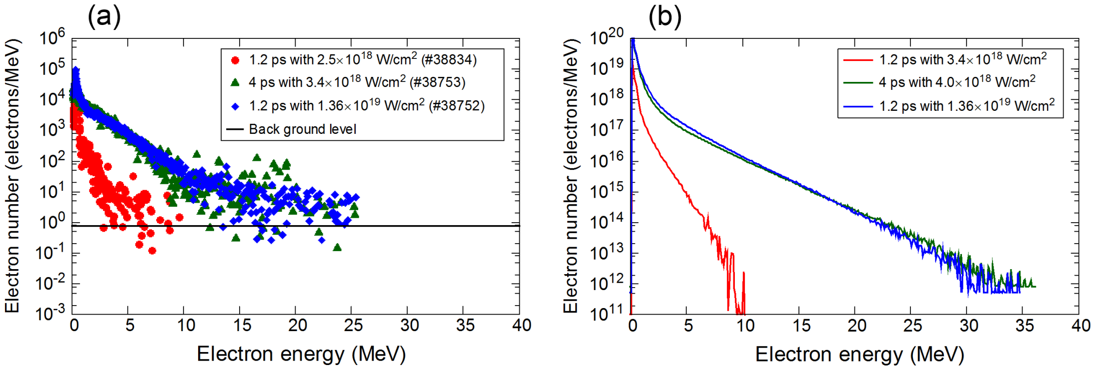

Figure 5-2: (a) RE energy distributions measured experimentally by changing the intensity and duration of laser pulses for cases A (red circles), B (green triangles), and C (blue squires). (b) RE energy distributions computed by two-dimensional particle-in-cell (PICLS-2D) simulations for cases A (red), B (green), and C (blue).

The experimental results were compared with the RE distribution obtained by the two-dimensional PIC simulation code (PICLS-2D; [82]). The calculations were performed with temporal and spatial scales that were comparable to the experimental scales. The gold cube was replaced with a 20 μm planar plasma with a peak density of $40n_{cr}$, where $n_{cr} = 1.0\times10^{21}$ cm^{-3} is the critical electron density for 1.053 μm wavelength light. The surface of the bulk plasma has an exponential density profile from 0.1 to $40n_{cr}$ and a scale length of 1 μm. The initial ionization degree of the plasma was set to +40. The slope temperatures of the REs in the simulation were 0.7, 2.0, and 2.0 MeV for cases A, B, and C, respectively. Thus, the PIC simulation reproduces well the experimentally observation of the slope temperature for the different laser intensities and pulse durations.

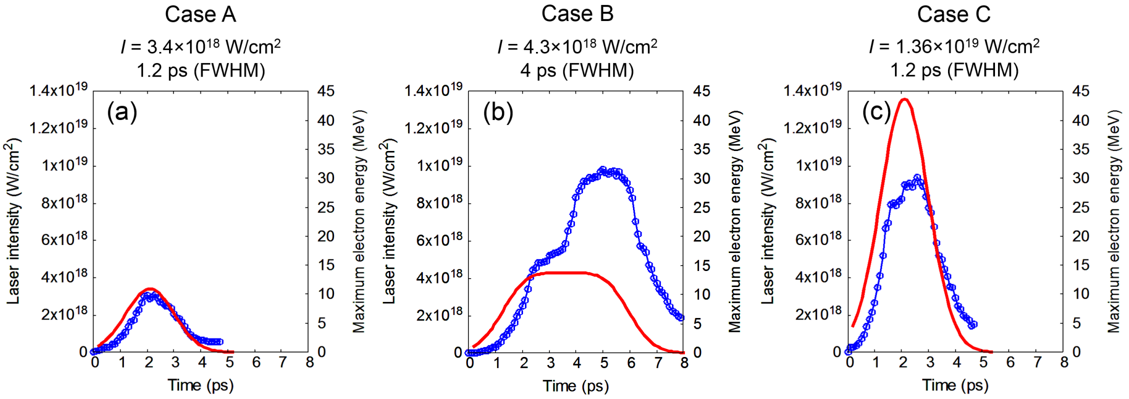

Figure 5-3: Comparisons between laser pulse shapes (red lines) and temporal evolution of the maximum energy of REs in simulations (blue lines between circles) for cases (a) A, (b) B, and (c) C. The temporal evolution of the maximum energy of the REs is similar to the laser pulse shapes for a pulse duration of 1.2 ps (cases A and C). For case B, the maximum energy increases after the timing when the laser intensity reaches a plateau at 2.0 ps, and the most energetic REs are produced at the end of the intensity plateau (5.5 ps).

Figure 5-3 shows comparisons of the simulating pulse shapes (red lines) and the temporal evolution of maximum energy of REs (blue lines between circles) for cases A, B, and C. The temporal evolution of the maximum energy of the REs is similar to the laser pulse shapes for a pulse duration of 1.2 ps (cases A and C). On the other hand, the situation for the pulse duration of 4.0 ps (case B) is completely different from the cases with the pulse duration of 1.2 ps. For case B, the maximum energy increases, even after the timing when the laser intensity reaches a plateau at 2.0 ps. The most energetic REs were produced at the end of the intensity plateau (5.5 ps). The time-integrated energy distributions of the REs for cases B and C seem to be identical; however, the temporal behavior of RE acceleration in case B is completely different from that in case C.

5.3 | Relativistic electrons accelerations during multi-ps laser plasma interaction under quasi-static electric field

The RE acceleration is affected by the temporal evolution of the electric and magnetic fields generated spontaneously in the laser-plasma interaction region by the multi-picosecond laser pulse. When the direction of the self-generated electric field is parallel to the direction of laser propagation (shown as Fig. 5-4), the equation for electron motion in the laser field is expressed as

$$\frac{dp_x}{dt} = \frac{1}{R}\frac{e^2A}{m_ec}\frac{dA}{dt} + e\frac{\partial\phi}{\partial x}, \tag{5.1}$$

$$R = \gamma - \frac{p_x}{m_ec} = 1 - \frac{e}{m_ec}\int\frac{\partial\phi}{\partial x}\left(1 - \frac{v_x}{c}\right)dt. \tag{5.2}$$

Here, e is the elementary charge, m_e is the mass of the electron at rest, c is the speed of light,

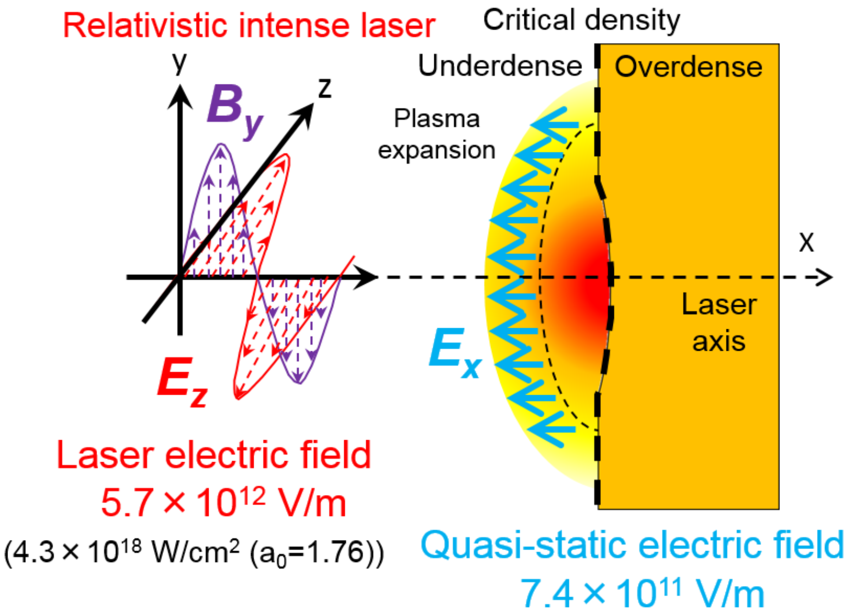

Figure 5-4: RE acceleration is affected by the temporal evolution of the electric and magnetic fields generated spontaneously in front of the target during the multi-picosecond interaction.

and A and ϕ are the vector potential of the laser field and the electrostatic potential, respectively. R represents the dephasing rate of the electron. The first term in Eq.(5.1) represents RE acceleration by the ponderomotive force of the incident laser light. The second term represents the effect of the electric field on the RE acceleration. The effect of the quasi-static electric field not only directly imparts additional energy ($e\frac{\partial \phi}{\partial x}$) to the electrons but also reduces the dephasing rate R [78, 83, 84, 85]. In the case where only the laser field exists ($\phi = 0$) in the interaction region, R is 1, and the maximum energy of the REs is $E_p = m_e c^2 a_0^2/2$. When R tends toward 0, due to the quasi-static field, the velocity of the RE tends toward the phase velocity of the laser field and the RE continues to ride on the acceleration phase, whereby the RE gains energy from the laser field beyond E_p.

Figure 5-5(a) shows increasing momentum with respect to the acceleration length. By adding an quasi-static electric field to the laser field, the kinetic energy of electrons tends to increase depending on the the acceleration length. This trend does not occur in the case of only the laser field. In the case of only the laser field, the maximum kinetic energy is limited by laser intensity (shown in Fig.5-5(b)).

Figure 5-5(c) shows the strength of the laser electric field that electron feels at each position. In the case of only the laser field represented by the red line, the strength of the electric field oscillates many times. This means that the speed of electron is slower than the speed of the laser field, thus the electrons are overtaken by multiple laser fields and interacts with multiple periods of the laser field. During interaction, the electrons alternately undergo acceleration and deceleration by $\boldsymbol{v} \times \boldsymbol{B}$.

On the other hand, in the case of laser field with quasi-static electric field represented by the blue line (shown in Fig.5-5(c)), the strength of laser electric field that electron feels does not oscillate. This means that the speed of the electron is close to the speed of the laser field, and the electron moves together with the laser field. Electron interacts only on one period of the laser field. Therefore, electrons entering to the acceleration phase, continue to be accelerated by $\boldsymbol{v} \times \boldsymbol{B}$ force and as the acceleration length increases, the kinetic energy increase.

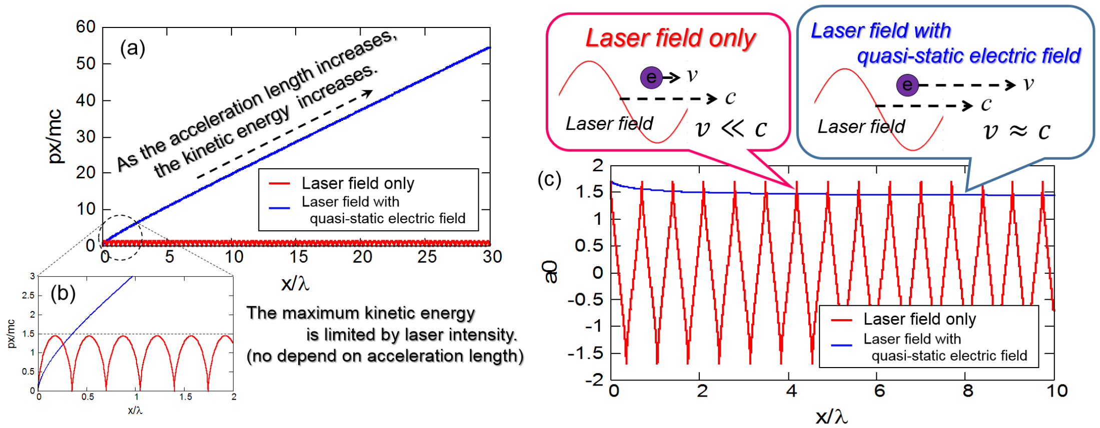

Figure 5-5: (a) increasing of momentum with respect to the acceleration length. By adding an quasi-static electric field to the laser field, the kinetic energy of electrons tends to increase depending on the the acceleration length. (c) the strength of the laser electric field that electron feels at each position. In the case of only the laser field, electron interacts with multiple periods of the laser field. During interaction, the electrons alternately undergo acceleration and deceleration by $\boldsymbol{v} \times \boldsymbol{B}$. On the other hand, in the case of laser field with quasi-static electric field, electron interacts only on one period of the laser field. Therefore, electrons entering to the acceleration phase, continue to be accelerated by $\boldsymbol{v} \times \boldsymbol{B}$ force and as the acceleration length increases, the kinetic energy increase.

These self-generated fields have a significant effect on the trajectories of the energetic REs. Figures 5-6(a)-(f) show three examples of the RE trajectories at two different periods (t = 3.0-3.5 and 5.0-5.5 ps) overlaid on the electron densities [(a) and (b)], self-generated azimuthal magnetic fields [(c) and (d)], and self-generated electric fields [(e) and (f)]. Figures 5-6(a) and (b) are colored using the look-up-table of electron density logarithm normalized according to the critical density (n_c).

In the earlier period (the left panels of Fig.5-6), the REs move around the near-critical density region. The energetic RE source is initially accelerated to 3-4 MeV by reflected laser light in the near-critical density region. 3-4 MeV is close to the kinetic energy (3.5 MeV) obtained by the ponderomotive force from reflected laser light ($a_0 = 1.7$ and $I = 4.3 \times 10^{18}$ W/cm^2) without absorption of the incident light. The electron travels outwardly (the opposite direction of laser propagation) through the magnetic and electric fields that are generated by the Biermann battery effect and charge separation. At this moment, the self-generated magnetic field strength is not sufficient to change the RE motion. The self-generated electric field decelerates the outwardly moving RE, and the RE eventually is accelerated again inwardly by the incident laser field. The RE is thus accelerated efficiently up to 15 MeV with assists of the self-generated quasi-static electric field and the laser field.

In the later period (right panels of Fig.5-6), the self-generated magnetic field is strong enough that some of the REs (blue and green trajectories) are reflected outwardly by $\boldsymbol{v} \times \boldsymbol{B}$ force and they are re-injected to the coexistence region of the self-generated electric field and laser field (second loop). In the second loop, the turning point of the RE is farther from the near-critical density region than that in the first loop because the REs received more kinetic energy before the second loop than that before the first loop. The REs obtain additional energy in the coexistence region after the second loop. This re-injection mechanism is LIDA [79].

The solid lines in Figs.5-7(a) and (b) show energy distributions of REs accelerated in the two

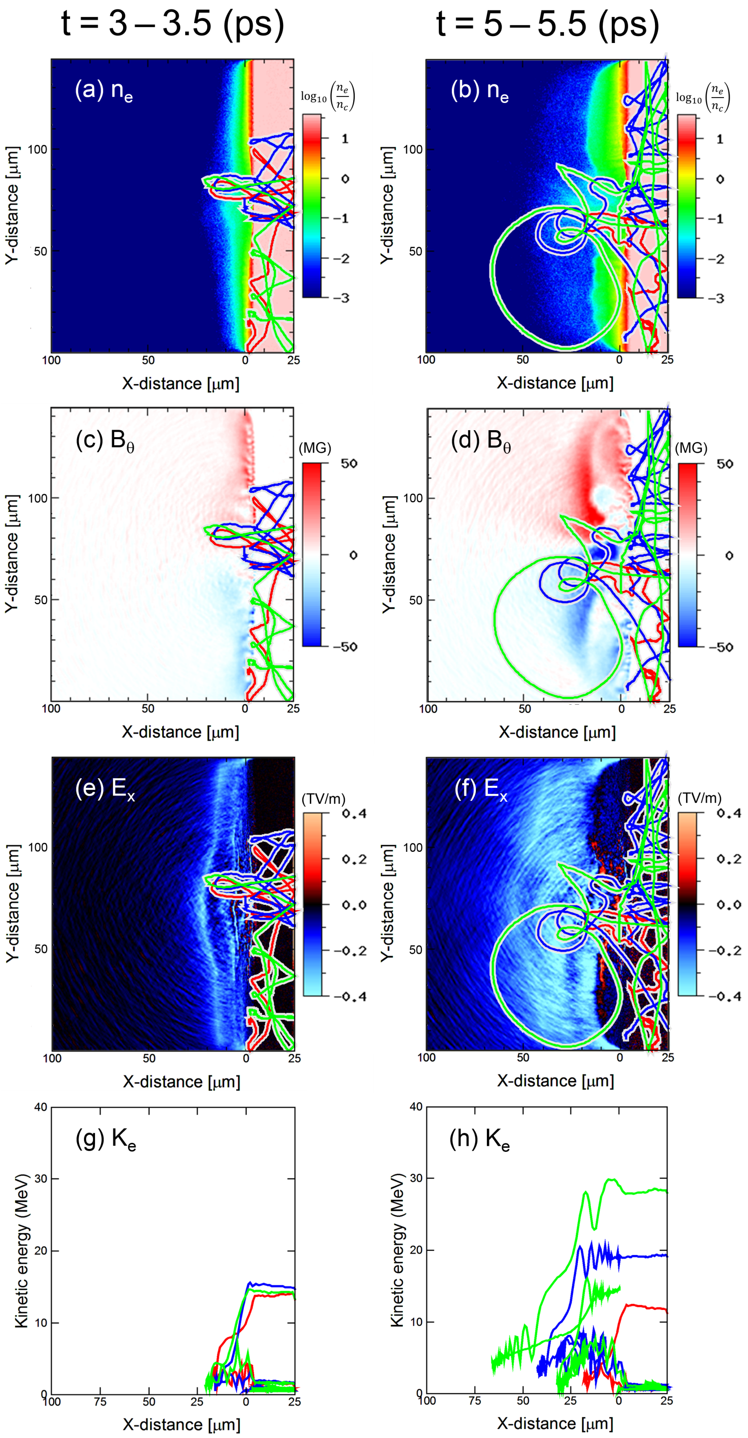

Figure 5-6: Three examples of RE trajectories at two different periods (t = 3.0-3.5 and 5.0-5.5 ps) overlaid on the electron densities [(a) and (b)], self-generated azimuthal magnetic fields [(c) and (d)], and self-generated electric fields [(e) and (f)]. The electron density maps [(a) and (b)] are colored using the look-up-table of electron density logarithm normalized according to the critical density (n_c). (g) and (h) Kinetic energies of REs along the longitudinal position for the two different periods.

periods. The histograms show ratio of RE numbers between two groups: one group (shown as the red bar) consists of REs that experienced single loop-injection and the other (shown as the green bar) consists of REs that experienced multiple loop-injection due to LIDA. Correlation between multiple loop-injections and energetic RE generation is clearly demonstrated.

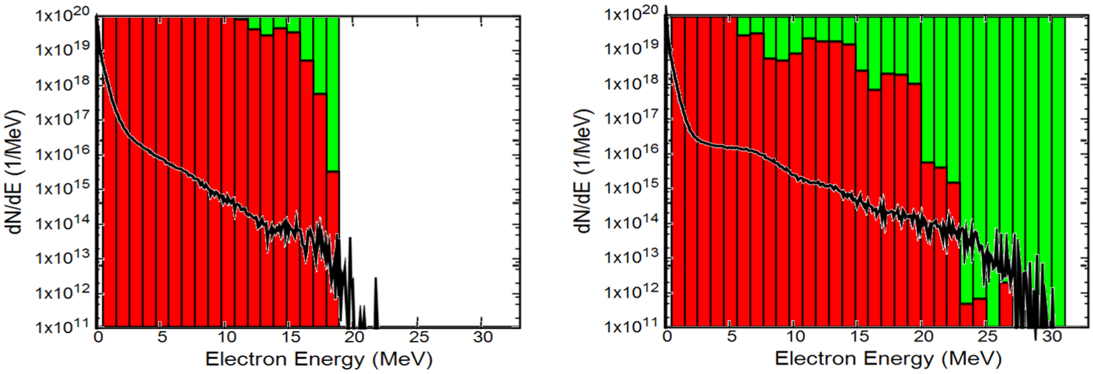

Figure 5-7: (a) and (b) Energy distributions (solid lines) of REs accelerated in the two periods (3.0-3.5 and 5.0-5.5 ps). The histograms show the ratio of RE numbers between the two groups, where one group (red bars) consists of REs that experienced single loop-injection and another group (green bars) consists of REs that experience multiple loop-injections due to LIDA. A correlation between multiple loop-injections and energetic electron generation is clearly evident.

5.4 | Generation of quasi-static magnetic field by multi-ps laser-plasma interaction

The PIC simulation shows that quasi-static magnetic field is generated by three different mechanisms in case B, which are dependent on the time during multi-picosecond laser-plasma interaction.

At the leading edge of the 4 ps flat-top pulse (<2 ps), the ponderomotive force of the incident laser pushes a relativistic critical density (γn_c) plasma into an overdense plasma. The laser-heated underdense plasma expands into vacuum. An azimuthal magnetic field is generated in the overdense plasma due to the $\nabla n \times \nabla I$ effect [86, 87], where n and I are the plasma electron density and the laser intensity, respectively. When the laser intensity reaches a plateau at 2.0 ps, the $\nabla n \times \nabla I$ mechanism becomes relatively small, whereas the $\nabla T \times \nabla n$ (Biermann battery) effect [88, 89, 90, 91] becomes the dominant mechanism for generation of the magnetic field in the underdense plasma (shown in Fig.5-8). Here, T is the plasma electron temperature. The strongest magnetic field is generated at the edge of the laser spot. This magnetic field influences the motion of REs around the bulk plasma surface. Some of REs moved transversely from the laser spot by the $\boldsymbol{E} \times \boldsymbol{B}$ drift. The $\boldsymbol{E} \times \boldsymbol{B}$ drift current heats surface of the bulk plasma via the two-stream instability. Enhancement of energy transfer to transverse direction due to the surface magnetic field is discussed in Ref. [92, 93, 94].

Figure 5-9(a) shows strong electric fields in the longitudinal direction (E_{x}) in three regions. The first electric field, which is generated near the bulk plasma surface, corresponds to the expansion front of the heated bulk plasma. The second electric field is generated around 2 ps, which corresponds to the forward edge of the flat-top. The third electric field is generated at the outer boundary of the expanding plasma. A strong magnetic field is also formed in the vicinity of the first electric field near the bulk plasma surface. Therefore, REs move along the bulk plasma surface by the $\boldsymbol{E} \times \boldsymbol{B}$

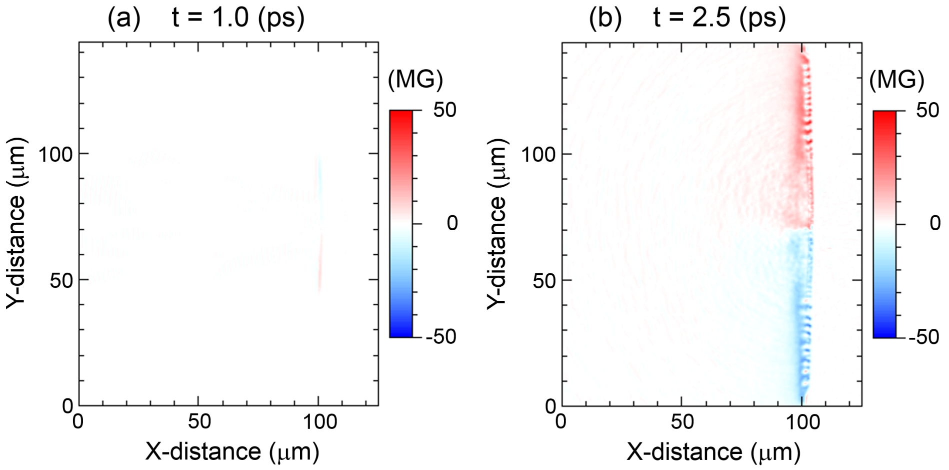

Figure 5-8: Spatial distribution of the azimuthal magnetic field strength at (a) 1 ps and (b) 2.5 ps in the PIC simulation. (a) The azimuthal magnetic field was generated by the $\nabla n \times \nabla I$ effect on the surface of the bulk plasma at 1 ps. (b) The Biermann's battery effect ($\nabla T \times \nabla n$) is the dominant mechanism of the magnetic field generation at 2.5 ps. This magnetic field drives a current along the bulk plasma surface due to the $\boldsymbol{E} \times \boldsymbol{B}$ drift.

drift. Although this drift direction is same as that at 2.0 ps, net drift current is ten times larger than that at 2.0 ps because spatial scale of the magnetic field is much larger than that at 2.0 ps.

Because Larmor radius of a 1 MeV electron in 10 MG magnetic field is 5 μm that is shorter than spatial scale of the magnetic field (10 μm), $<$ 1 MeV electrons are trapped by the self-generated magnetic field. The RE current driven by $\boldsymbol{E} \times \boldsymbol{B}$ drift is localized in the region with strong quasi-static electric and magnetic fields. When the REs flow in a plasma, the return-current is driven to maintain current neutrality in the plasma. Figure 5-9(b) shows the RE drift current in a lower density region and the return-current flow in a higher density region. The current loop produced by the spatial separation between the RE drift current and the return current generates a magnetic field along the outer edge of the plasma expansion (Fig.5-9(c)). This magnetic field (30-50 MG) becomes larger than that generated by the $\nabla T \times \nabla n$ effect (<10 MG).

The positive feedback between the growth of the fields and the field-driven drift current results in the rapid growth of the quasi-static electric and magnetic fields with time (Figs.5-9(d) and 5-9(f)). The maximum energy of the REs increases from 3.8 ps until 5.5 ps, which corresponds to the rapid growth of the self-generated fields.

At trailing edge of laser pulse, quasi-static fields begins to vanish. Collisionless properties of a rarefied and high temperature plasma result in slow diffusion and dissipation of these fields.

5.5 | Transition timing between compression regime and blow off regime of overdense plasma

In the previous section, we reported that quasi-static magnetic field is generate by three different mechanisms, which depend on time during multi-ps laser-plasma interaction. The first two magnetic fields have small spatial scales and these fields do not affect the motion of REs, while the magnetic field generated at last, has large spatial scale and it has large influence on the motion of REs. Maximum energy of the REs increases from 3.8 ps until 5.5 ps corresponding to the rapid growth of the magnetic fields generated at last. Therefore, the timing of magnetic field generation, corresponds

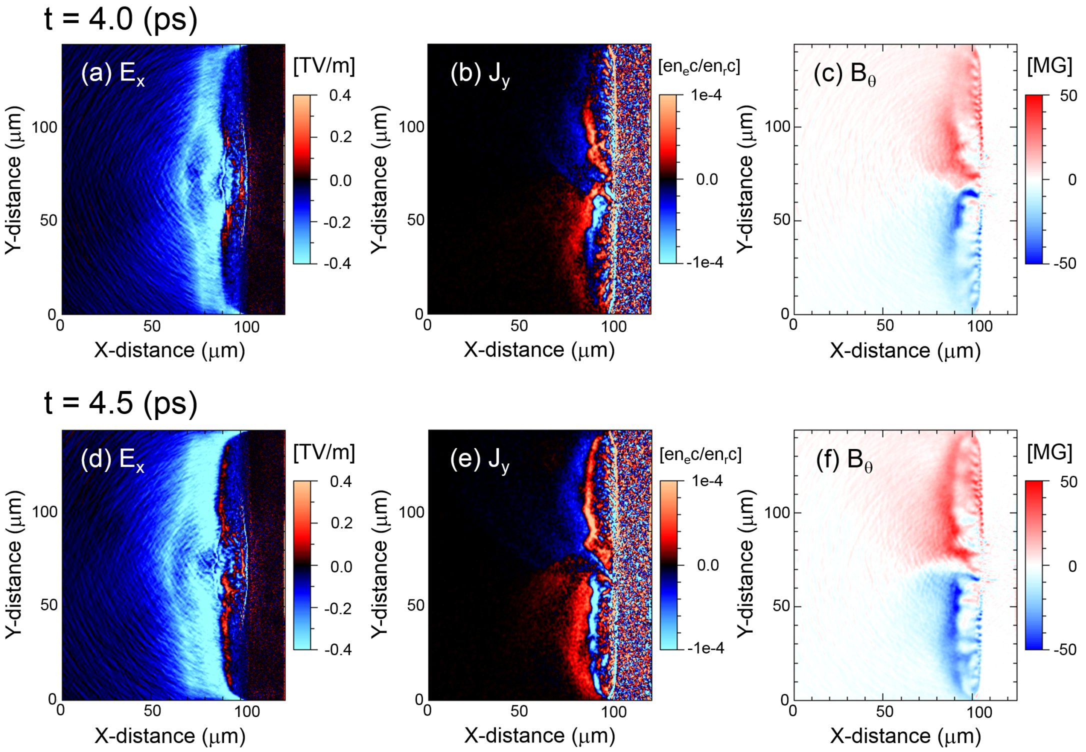

Figure 5-9: Strength of the electric field in the longitudinal direction (E_x), transverse current driven mainly by the $\boldsymbol{E} \times \boldsymbol{B}$ drift (J_y), and the strength of the azimuthal magnetic field (B_z) at 4.0 and 4.5 ps in the simulation. The $\boldsymbol{E} \times \boldsymbol{B}$ drift current and the corresponding return current produce a loop current that rapidly amplifies the magnetic field strength due to the positive feedback between the growth of the field and the field-driven drift current.

to the onset of increasing of the mean energy of electrons that is not desired in the fast ignition fusion research. Two-dimensional particle-in-cell simulation reveals that the magnetic field generation appear at 3.8 ps in which overdense plasma compression stops by laser ponderomotive pressure. In the time earlier than this timing, the electron temperature can be estimated by conventional scalings, however after than the timing, the effect of pulse expansion can not be ignored and modification of scalings is necessary.

Figure 5-10 show time evolution of self-generated magnetic field (a) and time evolution of plasma expansion (b), respectively. The horizontal axis shows space and the vertical axis shows time.

The quasi-static magnetic fields are rapidly growing in the underdense plasma, and grow starts from 3.8 ps indicated by the black dotted line. At the same time, strong expansion of underdense plasma is observed. The magnetic field expands widely according to the expansion of this plasma. The time when the plasama expansion occurred in the under desne region coincided with the stop time of the plasma compression in the overdense region, and the expansion speed of underdense was tripled from 3.8 ps. In this way, compression stopping of overdense plasma caused increase of energy of REB through expansion of underdense plasma, generation of self-generated magnetic field.

In Sec.5.5.1, compression velocity of a high density plasma with an exponential distribution by relativistic intensity laser and relativistic critical interface motion of a plasma that interacts with laser pulse having arbitrary intensity time profile, are explained. In this section, we aim to understand the physics effects that cause the slowing-down of the relativistic critical interface in a simplified one-dimensional approach.

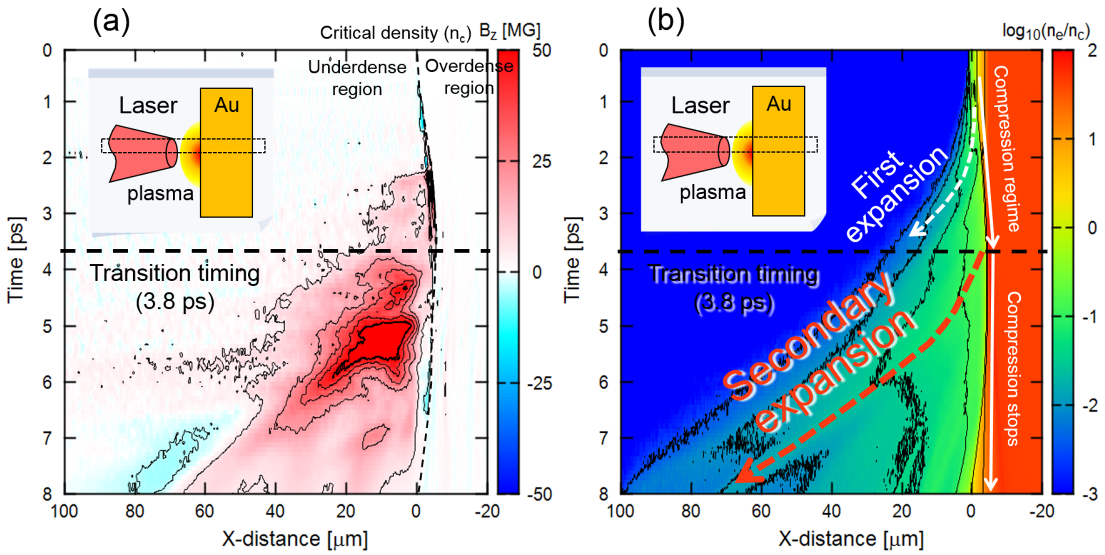

Figure 5-10: (a) Time evolution of self-generated magnetic field and (b) time evolution of plasma expansion. The quasi-static magnetic fields are rapidly growing in the underdense plasma, and grow starts from 3.8 ps indicated by the black dotted line. At the same time, strong expansion of underdense plasma is observed. The magnetic field expands widely according to the expansion of this plasma.

In Sec.5.5.2, the electron density threshold in which the compression of the relativistic critical density plasma terminates, is explained. This threshold is derived by a new model considering the motion of ions and electrons at the interaction surface. The threshold gives us the transition timing between the compression regime of the overcrowded plasma and the blow-off regime.

5.5.1 | Compression of plasma gradient and recession velocity of interaction surface

In the PIC simulation, the relativistic intensity laser propagates beyond the critical density by pushing the plasma. The compression of the high density plasma stops at 3.8 ps after from beginning of laser irradiation, and the position at which compression finally terminated, equals to the position of 17 times the critical density at the initial electron density. The physical phenomenon that a relativistic intensity laser pushes the high density plasma is known as hole-boring. Figure5-11 shows the schematic view of interaction between the laser and plasma components. In the laboratory frame (a), the laser reflects at the interaction surface and the interaction surface moves at velocity v_p. In this frame, electrons and ions of plasma component are initially immobile. REs moves with velocity at v_h.

In a frame moving at velocity v_p (b) (hereinafter referred to as a piston frame), the interaction surface is immobile and electrons and ions of plasma components flow into the interaction surface at velocity v_p. REs flow into the interaction surface at velocity v_h.

In the piston frame, we assume that all ions are reflected elastically (i.e. at velocity $+v_p$), a fraction $(1 - f_e)$ of electrons are reflected elastically (i.e. at velocity $+v_p$), a fraction f_e of electrons are accelerated by the relativistic laser and reflected elastically with a momentum $p_e/m_e c = \gamma_e$ This is a term that corresponds to the pressure of REs. Moreover, we assume that these REs are responsible for an absorption $(1 - R)$ of laser energy. Here, R is reflectivity of the incident laser on the plasma.

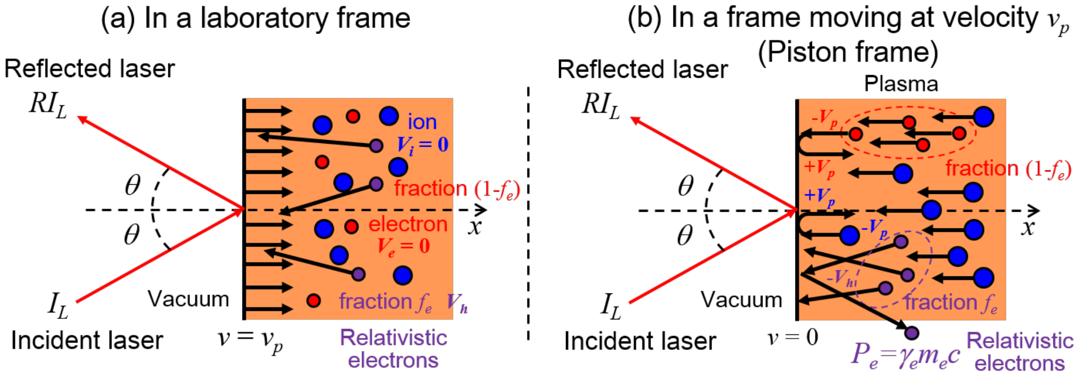

Figure 5-11: Schematic view of interaction between a laser and plasma components. In the laboratory frame (a), the laser reflects at the interaction surface and the interaction surface moves at velocity v_p. In this frame, electrons and ions of plasma component are initially immobile. REs moves with velocity at v_h. In a frame moving at velocity v_p (b) (hereinafter referred to as a piston frame), the interaction surface is immobile and electrons and ions of plasma components flow into the interaction surface at velocity v_p. REs flow into the interaction surface at velocity v_h.

The interaction between laser and plasma mainly occurs at relativistic critical density. Thus, the velocity of this interaction surface can be described using energy and momentum flux balance between laser and plasma components (ions and electrons) at the laser plasma interaction surface. [95],

$$\begin{aligned} \frac{I_+ + I_-}{c}\cos\theta &= f_e P_h + (1-f_e)P_c + P_i, \quad \text{(Momentum balance (Pressure balance))} \\ (I_+ - I_-)\cos\theta &= f_e F_h \quad \text{(Energy flux balance)} \end{aligned} \tag{5.3}$$

where $I_{+/-}$ denotes incident and reflected laser intensity, $P_{h/c}$ is momentum, and F_h is the energy flux density of relativistic electrons, respectively. P_i is the momentum flux density of ions, respectively.

In the case of high reflectivity of the laser at the interaction surface and relativistic laser intensity, the second term and the third term on the right side of the momentum balance equation can be ignored. The momentum transferred from the laser to plasma ions is $P_i \simeq 2I_-/c$, where $P_i = 2M_i n_i v_p^2 = 2M_i n_e v_p^2/Z$.

The velocity of the interaction surface in the unit of c is given by [8]

$$\frac{v_p}{c} = \sqrt{\frac{n_c}{2n_e}\frac{Zm_e}{M}a_0^2} = \sqrt{\frac{n_c}{2n_e}\frac{Zm_e}{M}\frac{I\lambda^2}{1.37\times10^{18}}}. \tag{5.4}$$

In our simulation results, the reflectivity of the laser at the interaction surface was 70-80%. For the case where the reflectivity is low like the our case, the velocity derived by Eq.(5.4) is over estimation, thus it is necessary to use the modified equations.

The equation of the momentum flux conservation that considering reflectivity at the interaction surface is given by

$$(1+R)\frac{I}{c}\cos\theta = 2M_i n_i v_p^2 + (2-f_e)m_e n_e v_p^2 + f_e n_e v_h p_h, \tag{5.5}$$

in the piston frame. Here n_e is number density of bulk electrons. n_h and T_h are number density and the slope temperature of REs, respectively. The first and second terms of the right side are momentum flux of bulk electrons and ions, respectively. The third term is momentum flux of REs.

We assumed that: the plasma is fully ionized (or ionization rate is fixed) so that there is no ionization current that would modify the momentum flux and, the thermal pressure $P_T = n_e k_B T_e$ of the bulk electrons is negligible compared to the radiation pressure $P_r = (1+R)I/c\cos\theta$ of the laser. In typical interaction conditions of this study, (electron density $n_e = 20n_c$, electron temperature $k_B T_e \simeq 1$ keV and laser intensity $I = 3\times10^{18}$ W/cm^2) we get $P_T \simeq 10$ Mbar $\ll P_R \simeq 1$ Gbar.

Here we assume that electrons with relativistic velocity as initial velocity are elastically reflected at the interaction surface, v_p is replaced by c.

Since a ion mass is much heavier than that of an electron ($m_e/m_i \ll 1$), we also can neglect the second term of the right hand side of Eq.(5.5). However, the momentum flux of REs ($f_e\frac{v_h}{c}n_hT_h$) is comparable to the momentum flux of ions ($2M_in_iv_p^2$). In typical parameters, ($M_i/m_e = 1840\times197$, $v_p/c \approx 0.01$, $v_h/c \approx 1$, $Z = 40$, $\gamma_e = 1.7$ and $f_e \approx 0.8$) we get $\frac{2M_in_iv_p^2}{f_em_en_hv_h\gamma_e} \approx 1.5$.

As the result, the equation of the momentum flux conservation can be approximated to

$$(1+R)\frac{I}{c}\cos\theta \approx 2M_in_iv_p^2 + f_en_ev_hp_h,$$

or

$$(1+R)\frac{I}{c}\cos\theta \approx 2M_in_iv_p^2 + f_em_en_ev_h\gamma c, \tag{5.6}$$

or

$$(1+R)\frac{I}{c}\cos\theta \approx 2M_in_iv_p^2 + f_e\frac{v_h}{c}n_eT_h,$$

The equation of the energy flux conservation is given by

$$(1-R)I\cos\theta = f_en_ev_hp_hc,$$

or

$$(1-R)I\cos\theta = f_en_ev_hm_ec^2[\sqrt{1+\gamma^2}-1], \tag{5.7}$$

or

$$(1-R)I\cos\theta = f_en_ev_hT_hc.$$

The left hand side of Eq.(5.7) corresponds to the accelerated electrons kinetic energy flux and the right hand side of Eq.(5.7) corresponds to the laser energy flux which is absorbed. Furthermore, from the comparison of the left and right sides of Eq.(5.7), f_e is equal to the absorption fraction of the laser $(1-R)$.

Subtracting Eq.(5.7) from Eq.(5.6), the velocity of interface in the unit of c is given by [96]

$$\frac{v_p}{c} \approx \sqrt{\frac{n_c}{2n_e}\frac{Zm_e}{M_i}Ra_0^2\cos\theta}, \tag{5.8}$$

This equation was derived considering the reflectivity of the laser at the interaction surface and the momentum flux carried away from the interaction surface by REs.

Reflection and density steepening occur at relativistic critical electron density $\gamma_{os}n_c$ with $\gamma_{os} = \sqrt{1+(1+R)a_0^2(t)/2}$, where a_0 is the normalized amplitude including the reflected light related to the intensity via $I(t)/c = m_ec^2n_ca_0^2(t)/2$ for a laser wavelength of 1μm. Moreover, the initial electron density profile is used $n_e(x) = (\gamma_{os}n_c)\exp[(x-x_c)/l_s]$ with scale length l_s.

Substituting all the above equations into Eq.(5.8), the velocity of the interaction surface in the unit of c is given by

$$\begin{aligned}
\frac{v_p(t)}{c} &= \sqrt{\frac{R\cos\theta}{(1+R)}\frac{Zm_e}{M_i}\left(\frac{\gamma_{os}^2(t)-1}{\gamma_{os}(t)}\right)}\exp\left(\frac{-(x-x_c)}{2l_s}\right),\\
\frac{dx}{dt} &= \sqrt{\frac{R\cos\theta}{(1+R)}\frac{Zm_ec^2}{2M_i}\left(\frac{\gamma_{os}^2(t)-1}{\gamma_{os}(t)}\right)}\exp\left(\frac{-(x-x_c)}{2l_s}\right).
\end{aligned}\tag{5.9}$$

The relativistic critical interface motion of a plasma with an exponential distribution that interacts with laser pulse having arbitrary intensity time profile, is obtained by integrating Eq.(5.9) by time,

$$\begin{aligned}
\int_0^{x_i}\exp\left(\frac{x-x_s}{2l_s}\right)dx &= \int_0^t\sqrt{\frac{R\cos\theta}{(1+R)}\frac{Zm_ec^2}{M_i}\frac{\gamma_{os}^2-1}{\gamma_{os}}}dt,\\
2l_s\left[\exp\left(\frac{x_i-x_s}{2l_s}\right)-\exp\left(\frac{x_c-x_s}{2l_s}\right)\right] &= \sqrt{\frac{R\cos\theta}{(1+R)}\frac{Zm_ec^2}{M_i}}\int_0^t\sqrt{\frac{\gamma_{os}^2-1}{\gamma_{os}}}dt,\\
\frac{x_i-x_c}{2l_s} &= \ln\left[1+\frac{1}{2l_s}\sqrt{\frac{R\cos\theta}{(1+R)}\frac{Zm_ec^2}{M_i}}\int_0^t\sqrt{\frac{\gamma_{os}^2-1}{\gamma_{os}}}dt\right].
\end{aligned}\tag{5.10}$$

When the laser intensity is constant over time,

$$\begin{aligned}
x_i(t) &= x_c+2l_s\ln\left(1+t\frac{u_p(t)}{2l_s}\right)\\
&= x_c+2l_s\ln\left[1+t\frac{c}{2l_s}\sqrt{\frac{R\cos\theta}{(1+R)}\frac{Zm_e}{M_i}\frac{\gamma_{os}^2(t)-1}{\gamma_{os}(t)}}\right].
\end{aligned}\tag{5.11}$$

When the laser intensity is an arbitrary time waveform,

$$x_i(t) = x_c+2l_s\ln\left[1+\frac{1}{2l_s}\sqrt{\frac{R\cos\theta}{(1+R)}\frac{Zm_ec^2}{M_i}}\int_0^t\left(\frac{\gamma_{os}(t)^2-1}{\gamma_{os}(t)}\right)^{1/2}dt\right].\tag{5.12}$$

As first definition of n_c at above, n_c indicates the position where the electron density corresponds with the relativistic critical density. According to this definition, x_c varies in time when laser intensity is an arbitrary time wave form. However, here we substitutes the position of initial critical density into x_c. Because, temporal profile of realistic laser increases from 0 to peak intensity and the laser starts to push plasma, when the intensity reaches at threshold of relativistic interaction (i.e., 1.37×10^{18} W/cm^2). When the laser starts to interact with plasma, the electron density is pilled up at the critical density and the tailing pulse interacts with the steepen interface. Thus, we can substitute the position of critical density into x_c. These behavior was observed in our PIC simulation result.

Sentoku *et al.* derived an equation of the velocity of the interaction surface with considering the momentum of REs. [97] If the laser is perfectly absorbed at the relativistic critical density (i.e., absorption fraction $(1-R)$ is 1), the speed of the interaction front is

$$\begin{aligned}
v_p = \sqrt{\frac{(1+R)I-n_hT_h}{2M_in_i(x)c}} &= \sqrt{\frac{(1+R)m_ec^3n_c(a_0^2/2)-n_hT_h}{2M_in_i(x)c}}\\
&= \sqrt{\frac{m_ec^2n_c(\gamma_{os}^2-1)-n_em_ec^2(\gamma_{os}-1)}{2M_in_i(x)}}
\end{aligned}\tag{5.13}$$

Here we used $T_h \simeq m_e c^2(\gamma_{os}-1)$, $\gamma_{os}=\sqrt{1+(1+R)a_0^2(t)/2}$ and $I(t)/c = m_e c^2 n_c a_0^2(t)/2$.

When laser interacts with an inhomogeneous plasma with density profile $n_i(x) = (\gamma_{os} n_c/Z)\exp[(x-x_c)/l_s]$, the velocity is given by

$$v_p(x) = \frac{dx}{dt} = \sqrt{\frac{m_e c^2 Z}{2M_i}\frac{(\gamma_{os}^2-1)}{\gamma_{os}}\exp\left(\frac{-(x-x_s)}{l_s}\right) - \frac{Zm_e c(\gamma_{os}-1)}{2M_i}} \tag{5.14}$$

The first term of the square root of the right side shows the effect of the momentum flux ions and the second term shows the effect of the newly added the momentum flux of REs.

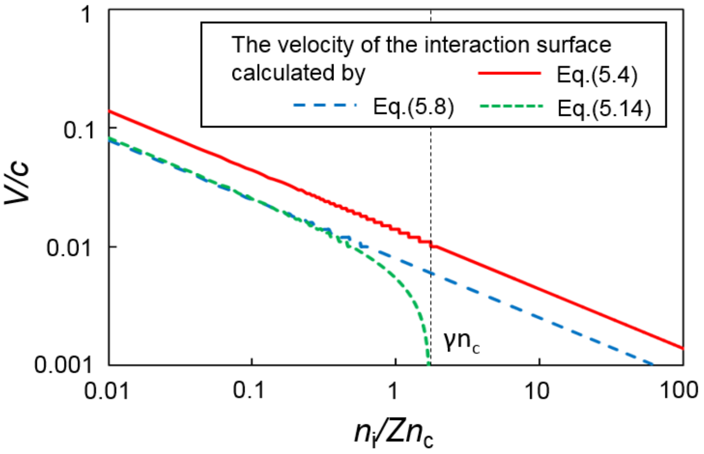

Figure 5-12: The velocity of the interaction surface calculated by the above three equations (Eq.(5.4), Eq.(5.9) and Eq.(5.14)). Equation(5.9), which takes into account the reflectivity to momentum conservation, derives lower velocity than Eq.(5.4). The velocity derived from Eq.(5.14), which takes into account the electron pressure is zero at the relativistic critical density.

The lines shown in Fig.5-12 plot the velocity of the interaction surface calculated by the above three equations (Eq.(5.4), Eq.(5.9) and Eq.(5.14)). The laser intensity was assumed to be 4.3×10^{18} W/cm^2 and the normalized laser intensity corresponding to this intensity is 1.7. Assuming that the laser reflectance at the interaction surface is 70%, the relativistic gamma factor with the modification of the reflectivity is 1.9.

Equation(5.9), which takes into account the reflectivity to momentum conservation, derives lower velocity than Eq.(5.4). The velocity derived from Eq.(5.14), which takes into account the electron pressure is zero at the relativistic critical density. In this equation, all the momentum given by the laser transfers into the relativistic electron momentum at relativistic electron density. From the velocity derived from Eq.(5.14), we can not explain high density plasma compression, with recession of an ion from relativistic critical density, seen in the PIC simulation.

Figure 5-13 depicts the evolution of an initially exponential plasma profile during the interaction with an high intense laser pulse. The color map shows the electron density ($\log_{10}(n_e/n_c)$). The black solid line shows the position of relative critical density surface at each time. Laser propagates toward high density by pushing the plasma. The compression of the high density plasma stops at 3.8 ps after from beginning of laser irradiation, and the position at which compression finally terminated, equals to the position of 17 times the critical density at the initial electron density ($n_e \approx 17n_c$). The dashed lines shown in Fig.5-13 plot the motion of the interaction surface calculated by Eq.(5.11) in the case

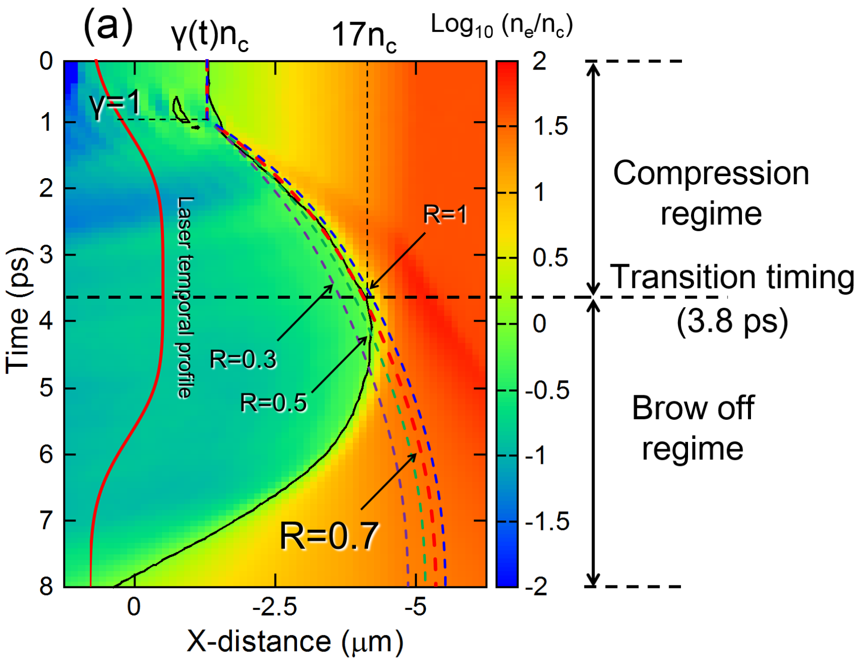

Figure 5-13: The evolution of an initially exponential plasma profile during the interaction with an high intense laser pulse. The motion of interaction surface calculated by Eq.(5.14) (shown as the red dotted line), is good agreement with the motion obtained by the PIC simulation until at 3.8 ps (shown as the black solid line).

of various reflectivity. The red dashed line calculated by substituting 0.7 into the reflectivity, well reproduces the motion obtained by the PIC simulation up to the halfway time. The assumption of reflectivity 0.7 and absorptivity 0.3 is consistent with the results obtained by PIC simulation and experimental measurements.

This result shows that the velocity of the interaction surface at each time can be determined by the momentum balance between the laser and ions, and the integration of the velocity of each time can explain the motion of the interaction surface. Moreover, this result indicated that the slowing-down of the critical surface motion seen in the PIC simulation can be explained by the exponential increase in density of the preformed plasma. However, the Eq.(5.9) can not explain the transition timing between the compression regime of the overcrowded plasma and the blow-off regime.

5.5.2 | Transition timing

In order to estimate the transition timing, it is necessary to consider the momentum transfer process from laser to ions. In previous work, simulations give almost identical results of motion of interaction surface with and without collisions [95, 96]. These results indicates that the laser momentum is transferred to momentum of ions at the interaction surface by a collisionless process (via the electrons, through electrostatic fields). Moreover, the fact that the pulse proceeds only in the limited time in a laser period was reported from detailed observations of pulse front motion in one laser period. [97] The velocity of ion oscillates with the ion local plasma frequency, which is $\tau_s = \sqrt{(M/m_e)(n_c/Z^2 n_i)}\tau$, where τ is one laser oscillation period and $\tau \simeq 3.3$ fs.

We assume that a laser interacts with a vacuum plasma interface at over the relativistic critical density. The electrons and ions have a step like profile along z-axis, respectively. The electron density is n_{e0} assuming charge-neutral ($n_e \approx Zn_i$). The laser can penetrate the plasma scale length l_s, and can make the charge separation in $l_s/2$ by the photon pressure. Note here that the laser intensity decays as $\exp(-x/2l_s)$ so as the photon pressure.

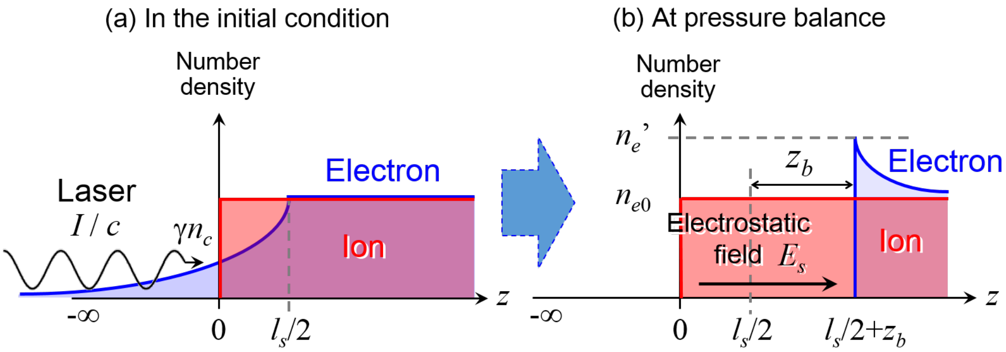

Figure 5-14: Schematic view of vacuum plasma interface. (a) We assume that a laser interacts with a vacuum plasma interface at relativistic critical density. The electrons and ions have an exponential profile and an step like, respectively. (b) When the laser pulse interacts with the plasma surface, electrons are quickly pushed inward by the laser photon pressure. The electrons pile up, leaving behind a charge depletion layer. The charge separation gives an electrostatic field.

When the laser pulse interacts with vacuum plasma interface, electrons are quickly pushed inward by the laser photon pressure. The response time of electrons to the laser field is much smaller than the optical period, while ions react on a longer timescale because of their larger mass [98]. The electrons pile up, leaving behind a charge depletion layer. The charge separation gives an electrostatic field. If the photon pressure exceeds the plasma pressure, the laser can hold the electric static field long enough the ions are moving, namely the interface moves forward. Then the vacuum-plasma interface moves to the position of $l_s/2 + z_b$

The transfer of the momentum flux from laser to electrostatic potential energy can be described as,

$$(1+R)\frac{I}{c} = \frac{E_s^2}{8\pi} + (1-R)n_e T_h, \tag{5.15}$$

where E_s is the electrostatic field at z_b. We can obtain E_s from the Gauss's law, and it is given by

$$\begin{gathered} \nabla \cdot \boldsymbol{E}_s = 4\pi\rho \\ \int_{-\infty}^{\frac{l_s}{2}+z_b} \boldsymbol{E}_s \cdot \boldsymbol{n}\, dS = 4\pi Ze \int_{-\infty}^{\frac{l_s}{2}+z_b} n_{i0}\, dV \\ E_s = 4\pi e n_{e0}\left(\frac{l_s}{2} + z_b\right). \end{gathered} \tag{5.16}$$

By substituting Eq.(5.16), the electrostatic potential energy can be obtained as

$$\frac{E_s^2}{8\pi} = 2\pi e^2 n_{e0}^2 \left(\frac{l_s}{2} + z_b\right)^2. \tag{5.17}$$

By substituting laser wavelength λ_L and critical density $n_c = \omega_L^2 m_e/4\pi e^2 = \pi m_e c^2/e^2\lambda_L^2$, laser intensity can be rewritten as

$$\begin{aligned} I &= c\frac{E_0^2}{4\pi} \\ &= \frac{c}{8\pi}\left(\frac{2\pi m_e c^2 a_0}{e\lambda_L}\right)^2 \\ &= \frac{c}{2\pi}(e\lambda_L n_c a_0)^2, \end{aligned} \tag{5.18}$$

where E_0 is laser electric field and a_0 is normalized laser field amplitude.

By substituting Eq.(5.17) and Eq.(5.18) into Eq.(5.15), the movement of momentum flux from laser to electrostatic potential energy can be written as

$$(1+R)\frac{(e\lambda_L n_c a_0)^2}{2\pi} = 2\pi e^2 n_{e0}^2\left(\frac{l_s}{2}+z_b\right)^2 + (1-R)n_e T_h. \tag{5.19}$$

By solving Eq.(5.19) for z_b, the charge separation distance is obtained as

$$z_b = \sqrt{\frac{1}{2\pi}}\frac{1}{en_{e0}}\left[(1+R)\frac{(e\lambda_L n_c a_0)^2}{2\pi} - (1-R)n_e T_h\right]^{1/2} - \frac{l_s}{2}. \tag{5.20}$$

When the skin depth is zero (i.e., $l_s/2 = 0$), and the plasma is cold ($(1-R)n_e T_h = 0$) because R =1,

$$\begin{aligned} z_b &= \sqrt{\frac{1}{2\pi}}\frac{1}{en_{e0}}\left[\frac{2(e\lambda_L n_c a_0)^2}{2\pi}\right]^{1/2} \\ &= \left(\frac{1}{\sqrt{2}}\frac{a_0/\pi}{N_0/n_c}\sqrt{\cos\theta}\right)\lambda_L. \end{aligned} \tag{5.21}$$

This is consistent with Eq.(9) of previous work (Z.Y.Ge *et al.*, PRE **89**, 033106 (2014) [98]). Solve Eq.(5.19) for n_{e0}:

$$n_{e0} = \sqrt{\frac{1}{2\pi}}\frac{1}{e\left(\frac{l_s}{2}+z_b\right)}\left[(1+R)\frac{(e\lambda_L n_c a_0)^2}{2\pi} - (1-R)n_e T_h\right]^{1/2}. \tag{5.22}$$

Hole boring stops when the charge separation distance becomes zero. (i.e. z_b=0.) By substituting zero for z_b, the initial number density of the electron plateau n_{e0} under the condition that the pushing of ions stops is obtained as

$$\begin{aligned} n_{e0} &= \sqrt{\frac{1}{2\pi}}\frac{2}{el_s}\left[(1+R)\frac{(e\lambda_L n_c a_0)^2}{2\pi} - (1-R)n_e T_h\right]^{1/2} \\ &= \frac{2\sqrt{2\pi}}{e\lambda_L}\sqrt{\frac{n_{e0}}{n_c}}\left[(1+R)\frac{(e\lambda_L n_c a_0)^2}{2\pi} - (1-R)n_e T_h\right]^{1/2}, \end{aligned} \tag{5.23}$$

where, we substituted $c/\omega_p = \lambda_L/2\pi\sqrt{n_c/n_{e0}}$ into the skin depth l_s.

When the plasma is cold (i.e., $(1-R)n_e T_h$ can ignore.),

$$\begin{aligned} \frac{n_{e0}}{n_c} &= \frac{2\sqrt{2\pi}}{e\lambda_L}\sqrt{\frac{n_{e0}}{n_c}}\left[(1+R)\frac{(e\lambda_L a_0)^2}{2\pi}\right]^{1/2} \\ &= \left(\frac{2\sqrt{2\pi}}{e\lambda_L}\right)^2\frac{e^2\lambda_L^2}{\pi}\left[(1+R)\frac{a_0^2}{2}\right] \\ &= 8\left[(1+R)\frac{a_0^2}{2}\right]. \end{aligned} \tag{5.24}$$

This indicates the maximum hole boring density is $n_{emax} = 8a_0^2 n_c$, which simply depends on a_0.

When the plasma is hot (i.e., $(1-R)n_eT_h$ can not ignore.),

$$\begin{aligned} n_{e0} &= \frac{2\sqrt{2\pi}}{e\lambda_L}\sqrt{\frac{n_{e0}}{n_c}}\left[(1+R)\frac{(e\lambda_L n_c a_0)^2}{2\pi} - (1-R)n_eT_h\right]^{1/2} \\ &= \frac{2\sqrt{2\pi}}{e\lambda_L}\sqrt{\frac{n_{e0}}{n_c}}\left[(1+R)\frac{(e\lambda_L n_c a_0)^2}{2\pi} - (1-R)\gamma(\gamma-1)n_c m_e c^2\right]^{1/2}. \end{aligned} \tag{5.25}$$

$$\begin{aligned} \frac{n_{e0}}{n_c} &= \frac{2\sqrt{2\pi}}{e\lambda_L}\sqrt{\frac{n_{e0}}{n_c}}\left[(1+R)\frac{(e\lambda_L a_0)^2}{2\pi} - (1-R)\gamma(\gamma-1)\frac{(e\lambda_L)^2}{\pi}\right]^{1/2} \\ &= \left(\frac{2\sqrt{2\pi}}{e\lambda_L}\right)^2\frac{e^2\lambda_L^2}{\pi}\left[(1+R)\frac{a_0^2}{2} - (1-R)\gamma(\gamma-1)\right] \\ &= 8\left[(1+R)\frac{a_0^2}{2} - (1-R)\gamma(\gamma-1)\right]. \end{aligned} \tag{5.26}$$

Here we assumed that mean energy of REs is determined by ponderomotive energy, and can be substituted that $T_h = m_e c^2(\gamma - 1)$.

From the comparison of Eq.(5.23) and Eq.(5.26), it is found that the first term on the right side of Eq.(5.26) is a term derived from the electrostatic potential energy and the second term is derived from the pressure by REs.

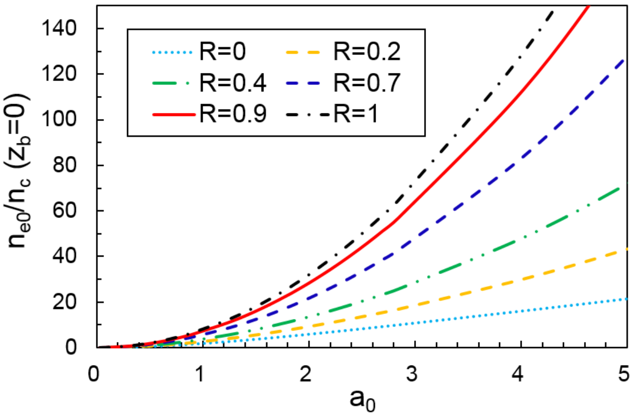

Figure 5-15: Maximum hole boring density at the various reflectivity. When a_0 increases, the maximum hole boring density raises. When the reflectivity of the laser at the interface is high (the laser photon pressure increases), the maximum hole boring density raises.

By substituting a_0 =1.79, R =0.7 and γ =1.9, the initial number density of the electron plateau n_{e0} under the condition that the pushing of ions stops for the our conditions is obtained as

$$\begin{aligned} \frac{n_{e0}}{n_c} &= 8\left[(1+R)\frac{a_0^2}{2} - (1-R)\gamma(\gamma-1)\right] \\ &= 8\left[(1+0.7)\frac{1.79^2}{2} - (1-0.7)1.9(1.9-1)\right] \\ n_{e0} &= Zn_{i0} = 1.76n_c \approx 17n_c. \end{aligned} \tag{5.27}$$

The initial number density of the electron plateau where the hole boring stops obtained from this model is consistent with the result obtained by the PIC simulation. When the hole boring stops the plasma pressure overcome the photon pressure, so that the plasma starts to blow-off.

By combining this condition ($n_e = 17n_c$) with Eq.(5.14) describing the position of the plasma compression front and the initial ion density profile $n_i(x) = (\gamma_{os}n_c/Z)\exp[(x - x_c)/l_s]$, we can estimate the transition timing t between the compression regime of the overdense plasma and the blow off regime to be $t \approx 3.8$ ps

When the laser intensity is constant over time, the transition timing can be described by a simple equation. Substituting Eq.(5.11) describing the position of the interface into $n_e(x) = (\gamma_{os}n_c\exp[(x-x_c)/l_s])$ describing the initial electron density profile yields

$$\frac{n_e}{n_c} = \gamma_{os}\exp\left(\frac{x_c + 2l_s\ln\left[1 + t\frac{c}{2l_s}\sqrt{\frac{R\cos\theta}{(1+R)}\frac{Zm_e}{M_i}\frac{\gamma_{os}^2-1}{\gamma_{os}}}\right] - x_c}{l_s}\right). \tag{5.28}$$

Substituting Eq.(5.26) describing the maximum hole boring density into Eq.(5.28) yields

$$\begin{aligned} 8\left[(1+R)\frac{a_0^2}{2} - (1-R)\gamma_{os}(\gamma_{os}-1)\right] &= \gamma_{os}\left(1 + t\frac{c}{2l_s}\sqrt{\frac{R\cos\theta}{(1+R)}\frac{Zm_e}{M_i}\frac{\gamma_{os}^2-1}{\gamma_{os}}}\right)^2 \\ \sqrt{\frac{8}{\gamma_{os}}\left[(\gamma_{os}^2-1) - (1-R)\gamma_{os}(\gamma_{os}-1)\right]} &= 1 + t\frac{c}{2l_s}\sqrt{\frac{R\cos\theta}{(1+R)}\frac{Zm_e}{M_i}\frac{\gamma_{os}^2-1}{\gamma_{os}}}. \end{aligned} \tag{5.29}$$

The transition timing is given by

$$\begin{aligned} t &= \frac{2l_s}{c}\sqrt{\frac{(1+R)}{R\cos\theta}\frac{M_i}{Zm_e}\frac{\gamma_{os}}{\gamma_{os}^2-1}}\left[\sqrt{8\frac{\gamma_{os}^2-1}{\gamma_{os}} - 8(1-R)\gamma_{os}\frac{(\gamma_{os}-1)}{\gamma_{os}}} - 1\right] \\ t &= \frac{2l_s}{c}\sqrt{\frac{(1+R)}{R\cos\theta}\frac{M_i}{Zm_e}}\left[\sqrt{8}\sqrt{1 - \frac{\gamma_{os}(1-R)}{\gamma_{os}+1}} - \sqrt{\frac{\gamma_{os}}{\gamma_{os}^2-1}}\right]. \end{aligned} \tag{5.30}$$

By substituting $\alpha m_p Z^*$ into ion mass M_i, the transition timing is rewritten by

$$t = \frac{2l_s}{c}\sqrt{\frac{(1+R)}{R\cos\theta}\frac{\alpha m_p Z^*}{Zm_e}}\left[\sqrt{8}\sqrt{1 - \frac{\gamma_{os}(1-R)}{\gamma_{os}+1}} - \sqrt{\frac{\gamma_{os}}{\gamma_{os}^2-1}}\right]. \tag{5.31}$$

Here, m_p is proton mass, Z^* is ion charge number for fully ionized state and α is 1(or 2) for Hydrogen (for the other species).

5.6 | Energy conversion efficiency from laser to relativistic electrons during multi-ps laser plasma interaction

In section 5.5, we explained that the timing of increasing of relativistic electron energy can be estimated by the theoretical model that is based on one-dimensional momentum flux balance. This model depends on the reflectivity of the laser at the interaction surface. In the calculation described at previous section, we could explain the phenomenon obtained by the PIC simulation comprehensively by the model when substituting 0.7 into the reflectivity R. In this section, we describe energy conversion efficiency from laser to electron observed at experiment and PIC simulation. Since absorbed energy of a laser is mostly transfered to electrons, it is assumed that the value obtained by subtracting the electron conversion efficiency from 1 is the laser reflectivity. In Section 5.6.1, we describe that comparison of the time integrated energy conversion efficiencies observed in the experiment and PIC simulation. In section 5.6.2, the time evolution of mean energy of REs observed by PIC simulation is described.

5.6.1 | Comparison of the time integrated energy conversion efficiencies between experiment and PIC simulation

Bremsstrahlung x rays were measured using high energy x-ray spectrometers (HEXSs) (see Sec.3), the spectrometers consist of K-edge and differential x-ray filters and use imaging plates (IPs) as detectors. Two HEXSs were set at 159.1°, and 110.9° from the LFEX laser axis. The dependence of the doses on the IP order in the stack was compared with Monte Carlo calculations. The electron energy distribution is assumed to be a sum of two Boltzmann distributions (Eq. (5.32)) with two different slope temperatures (T_{REB1}, T_{REB2} and $T_{REB1} < T_{REB2}$) to simplify the process, namely

$$f(E) = A\exp\left(-\frac{E}{T_{REB1}}\right) + (1-A)\exp\left(-\frac{E}{T_{REB2}}\right), \tag{5.32}$$

and a single divergence angle (θ_{div}=41°(FWHM)) of the REB were assumed. Here A and E are the relative coefficient and the electron kinetic energy, respectively. Slope temperature of higher energy component was obtained by fitting the energy distribution of the vacuum electrons for reducing indefiniteness of the fitting process.

Case A: 1.2 ps of pulse duration and 3.4×10^{18} W/cm^2 of peak intensity

Firstly, we report energy conversion efficiency of the single beam (Case A: 1.2 ps FWHM of pulse duration and 3.4×10^{18} W/cm^2 of peak intensity). Figure 5-17 shows the relative x-ray doses (red solid circles) recorded on imaging plates in HEXSs observed in the case of A (1.2 ps). The signals are normalized so that the signal of the first layer of HEXS is 1.

The judgment process described in the Chapter 3 was performed for twenty-four IPs equipped in two HEXS. Figure 5-16 shows number of matching IP. Maximum number was found in the area of $(A, T_{REB1} = (0.8-1, 0.3-0.5)$. In this area, 17 of 24 IPs match.

In this case, we could not find an area where all of IP signals could be reproduced. This may be caused by fluctuation of photon statistics on IP is large because the amount of x rays is small.

The curves shown in Fig.5-17 were calculated for three cases of REB energy distribution; [Case A (blue solid line)] A=0.91, T_{REB1}=0.3 MeV,and T_{REB2}=0.65 MeV; [Case B (orange solid line)] A=1, T_{REB1}=0.3 MeV; [Case C (green solid line)] A=1, T_{REB2}=0.65 MeV, respectively. The error bar of the relative x-ray doses was defined as 19.4% of the signal value. The derivation of this error bar was explained in the Chapter 3.

The orange line (the green line) shows contribution of lower energy component (higher energy component) to the doses of the IP. In the case of considering only the lower energy component, it was impossible to reproduce the doses recoreded on the 9th to 12th IPs lined in the latter half of the IP stack. On these IPs, the calculated doses have a smaller signal value than the experimental doses. This result suggests the existence of unconsidered higher energy components. In contrast, when considering only the high energy component, the calculated doses have a larger signal value than the experimental doses. This result suggests the existence of unconsidered lower energy components. As the result, about 90% of the lower energy component and about 10% of the higher energy component are necessary for comprehensively reproducing the experiment signal recorded in the IP stack.

The color map in Fig.5-18 (a) shows the energy conversion efficiency from the laser to electrons of lower energy component that obtained by Eq.(4.18). The color map in Fig.5-18 (b) shows the energy conversion efficiency from the laser to the electrons of both components that obtained by

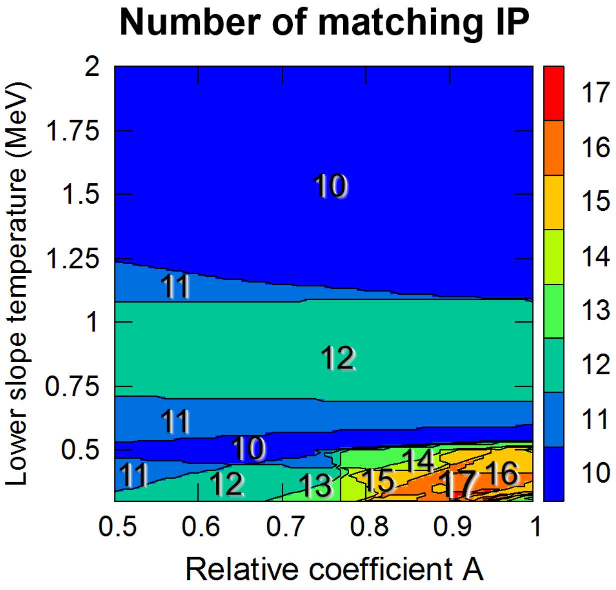

Figure 5-16: Results of the judgment process. The color map shows number of matching IP. Maximum number was found in the area of (A, T_{REB1} = (0.8-1, 0.3-0.5). In this area, 17 of 24 IPs match.

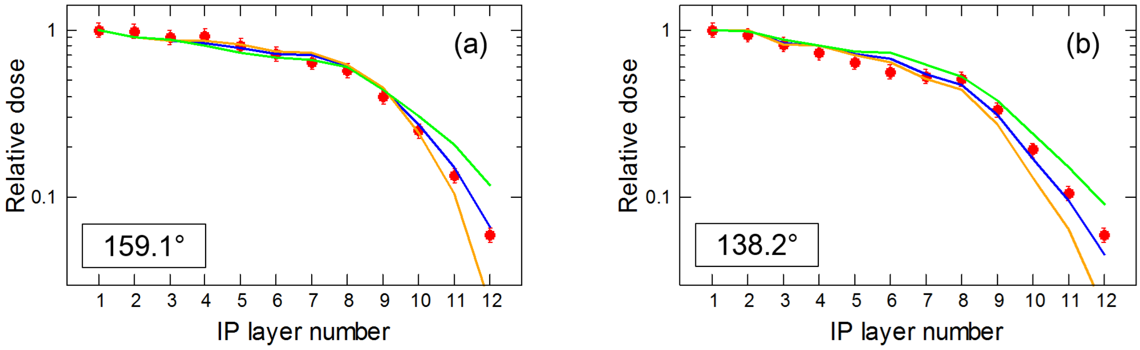

Figure 5-17: Relative x-ray doses recorded on imaging plates in HEXSs located at (a) 159.1°, and (b) 138.2° from the LFEX laser incident axis. The curves were calculated for three cases of REB energy distribution; [Case A (blue solid line)] A=0.91, T_{REB1}=0.3 MeV,and T_{REB2}=0.65 MeV; [Case B (orange solid line)] A=1, T_{REB1}=0.3 MeV; [Case C (green solid line)] A=1, T_{REB2}=0.65 MeV, respectively.

Eq.(4.20). The white-painted area in the both figure, shows the area where the coincidence rate between the experimental value and simulation value was high shown in the Fig.5-16.

By comparing the white-painted area with the color maps, we can read the conversion efficiency from Fig.5-18. In this experiment, HEXSs' signal indicated that 8.75-12% of the laser energy was converted to REs of lower energy component, and 11-17.5% of energy was converted to REs of both components.

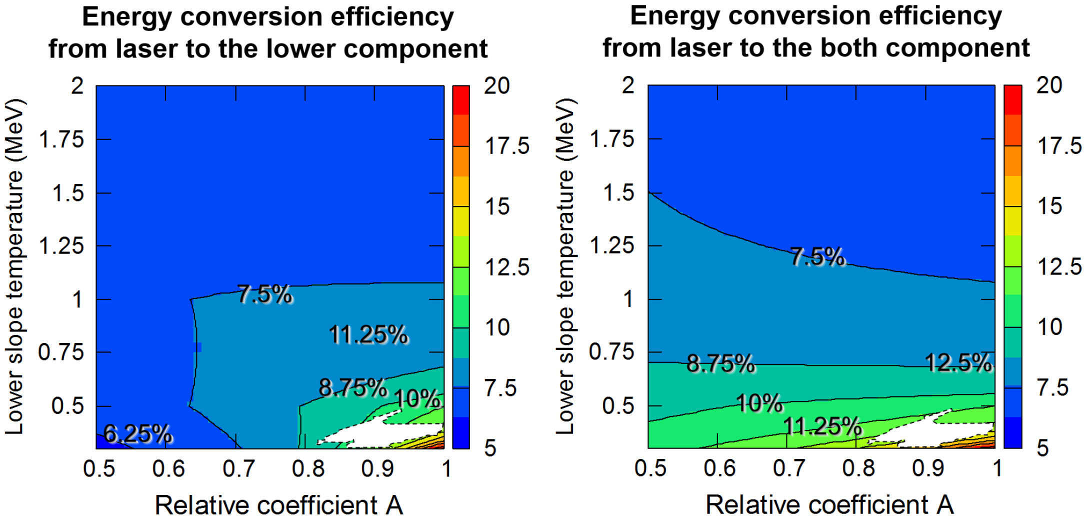

Figure 5-18: (a) energy conversion efficiency from the laser to electrons of lower energy component that obtained by Eq.(4.18). (b) energy conversion efficiency from the laser to the electrons of both components that obtained by Eq.(4.20). The white-painted area in the both figure, shows the area where the coincidence rate between the experimental value and simulation value was high shown in the Fig.5-16.

Case B: 4.0 ps of pulse duration and 4.3×10^{18} W/cm^2 of peak intensity

Figure 5-20 shows the relative x-ray doses (red solid circles) recorded on imaging plates in HEXSs observed in the case of B (4.0 ps). The signals are normalized so that the signal of the first layer of HEXS is 1. Figure 5-16 shows number of matching IP. Maximum number was found in the area of $(A, T_{REB1} = (0.8 - 0.9, 0.4 - 0.6)$. In this area, 20 of 24 IPs match.

The curves were calculated for three cases of REB energy distribution; [Case A (blue solid line)] A=0.85, T_{REB1}=0.4 MeV,and T_{REB2}=2.0 MeV; [Case B (orange solid line)] A=1, T_{REB1}=0.4 MeV; [Case C (green solid line)] A=1, T_{REB2}=2.0 MeV, respectively.

The color map in Fig.5-18 (a) shows the energy conversion efficiency from the laser to electrons of lower energy component that obtained by Eq.(4.18). The color map in Fig.5-18 (b) shows the energy conversion efficiency from the laser to the electrons of both components that obtained by Eq.(4.20). The white-painted area in the both figure, shows the area where the coincidence rate between the experimental value and simulation value was high shown in the Fig.5-16.

By comparing the white-painted area with the color maps, we can read the conversion efficiency from Fig.5-18. In this experiment, HEXSs' signal indicated that 12.5-17.5% of the laser energy was converted to REs of lower energy component, and 22.5-30% of energy was converted to REs of both components.

5.6.2 | Time evolution of mean energy of REs during multi-ps laser plasma interaction

Figure 5-22 shows the time evolution of the lower slope temperature of REs obtained by PIC simulation. The red lines show the result of a 4 ps long pulse (labeled as LP) and the blue lines show the result of a 1.2 ps short pulse (labeled as SP). Time evolution of mean energy was obtained by recording the number and energy distribution of REs at intervals of 0.1 ps. The dotted lines show

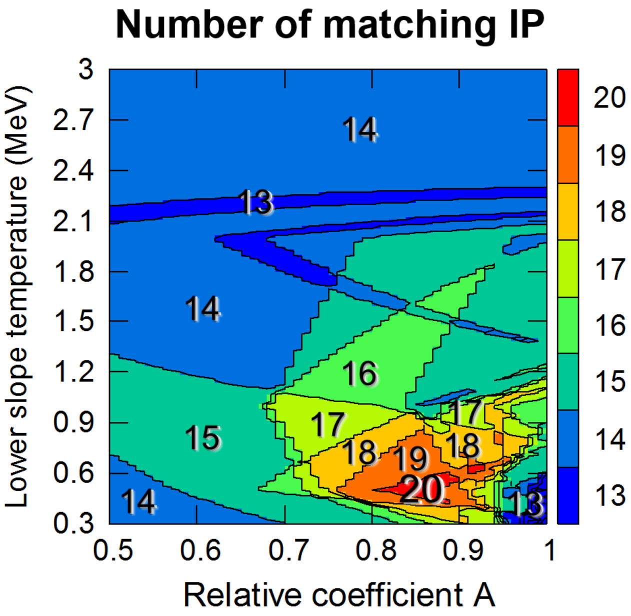

Figure 5-19: Results of the judgment process. The color map shows number of matching IP. Maximum number was found in the area of (A, T_{REB1} = (0.8-0.9, 0.4-0.6). In this area, 20 of 24 IPs match.

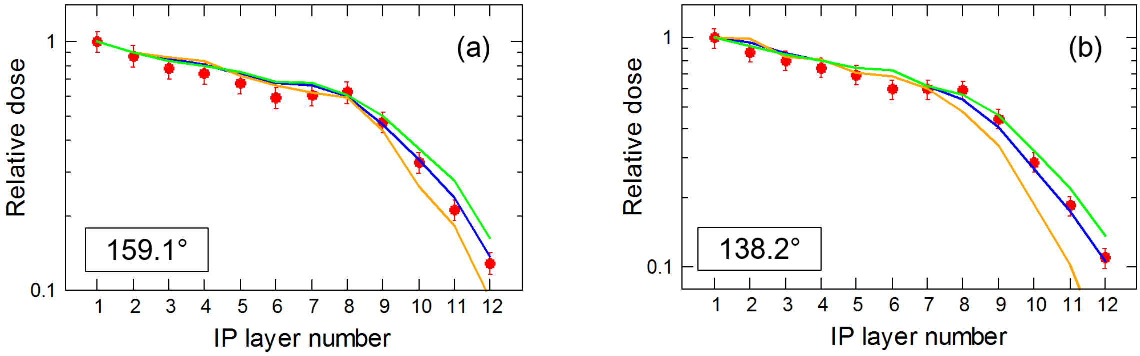

Figure 5-20: Relative x-ray doses recorded on imaging plates in HEXSs located at (a) 159.1°, and (b) 138.2° from the LFEX laser incident axis. The curves were calculated for three cases of REB energy distribution; [Case A (blue solid line)] A=0.85, T_{REB1}=0.4 MeV,and T_{REB2}=2.0 MeV; [Case B (orange solid line)] A=1, T_{REB1}=0.4 MeV; [Case C (green solid line)] A=1, T_{REB2}=2.0 MeV, respectively.

the ponderomotive energy estimated from the laser intensity at each time. Ponderomotive energy is expressed as $T_e = 0.511(\sqrt{1+a_0^2/2}-1)$ using normalized laser intensity a_0. The mean energy of the relativistic electrons obtained by the PIC simulation showed good agreement with the laser ponderomotive energy.

This result shows that REs of the lower energy component are generated when the laser interacts with the relativistic critical density plasma (shown is Fig.5-24). Since the laser electric field exponentially decreases in the plasma above the relativistic critical density, electrons are strongly

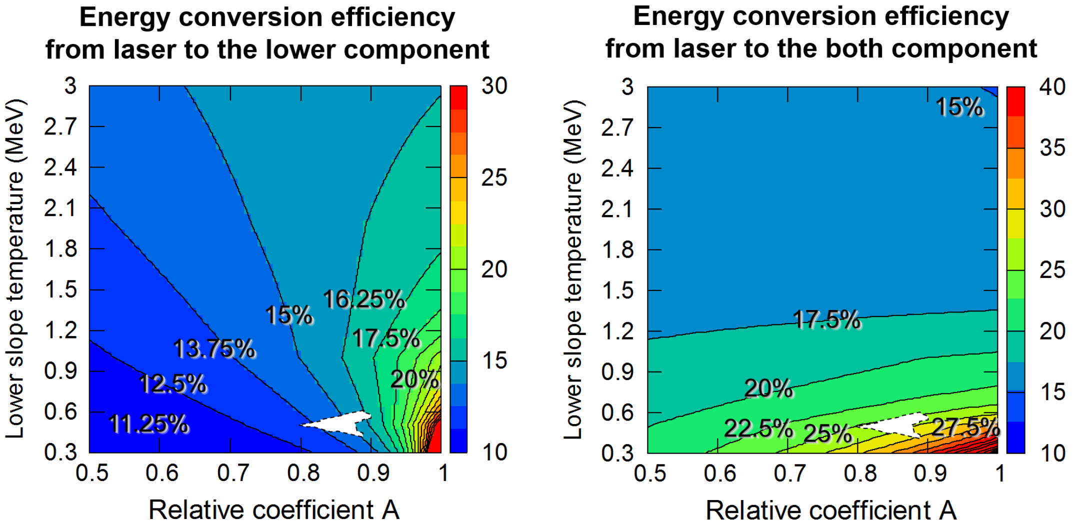

Figure 5-21: (a) energy conversion efficiency from the laser to electrons of lower energy component that obtained by Eq.(4.18). (b) energy conversion efficiency from the laser to the electrons of both components that obtained by Eq.(4.20). The white-painted area in the both figure, shows the area where the coincidence rate between the experimental value and simulation value was high shown in the Fig.5-16.

Table 5.1: Relative coefficient, slope temperatures and energy conversion efficiencies

Case A: 1.2 ps of pulse duration					
	A	T_{REB1}	T_{REB2}	$\mathrm{CE}^{\mathrm{lower}}$	$\mathrm{CE}^{\mathrm{both}}$
Simulation	0.99	0.3 MeV	0.7 MeV	22%	23%
Experiment	0.8-1	0.3-0.5 MeV	0.65 MeV	8.75-12%	11-17.5%
Case B: 4 ps of pulse duration					
	A	T_{REB1}	T_{REB2}	$\mathrm{CE}^{\mathrm{lower}}$	$\mathrm{CE}^{\mathrm{both}}$
Simulation	0.99	0.3 MeV	2.4 MeV	45%	49%
Experiment	0.8-0.9	0.4-0.6 MeV	2.0 MeV	12.5-17.5%	22.5-30%

accelerated in the laser traveling direction by the ponderomotive force determined by the space variation of the square of the electric field. As shown in Fig.5-14, even in the interaction of long pulses, the relativistic critical density surface is pushed to the high density side by laser hole boring at most of the time during interaction, thus the relativistic critical density surface never expands. Therefore, the slope temperature of electrons observed at the long pulse is simply depend on the ponderomotive energy of the laser as similar as the case of the short pulse.

Moreover, REs are also observed at the time after the laser intensity decreases. These electrons are trapped by the quasi-static magnetic field formed on the relativistic critical density surface, and they are released from the interaction region at the time when the strength of the fields decreases. Since the quasi-static magnetic field generated on the critical density surface, can grow during short pulse duration, this trend was observed in both 1.2 ps and 4 ps duration pulses.

The effect of plasma blow off described in the previous section, clearly appears in the slope temperature of higher energy component of RE spectra (shown in Fig.5-23). After the transition timing (3.8 ps), the slope temperature of higher energy component rises sharply by 1.3 MeV. REs

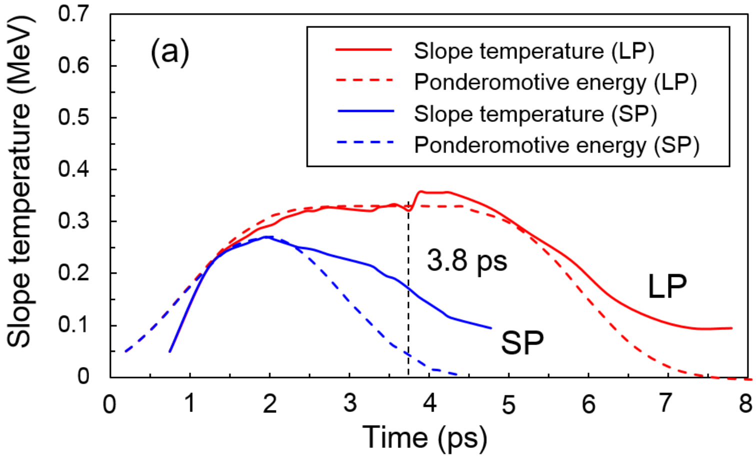

Figure 5-22: Time evolution of the lower slope temperature of REs obtained by PIC simulation. The red lines show the result of a 4 ps long pulse (labeled as LP) and the blue lines show the result of a 1.2 ps short pulse (labeled as SP). The dotted lines show the ponderomotive energy estimated from the laser intensity at each time. The mean energy of the relativistic electrons obtained by the PIC simulation showed good agreement with the laser ponderomotive energy.

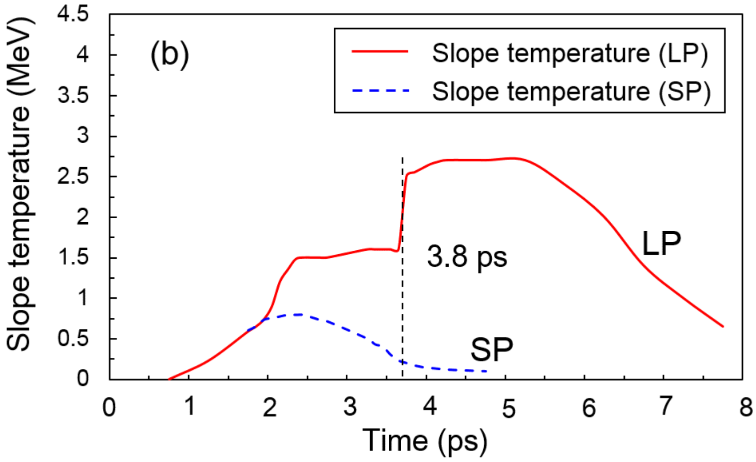

Figure 5-23: Time evolution of the higher slope temperature of REs obtained by PIC simulation. The red lines show the result of a 4 ps long pulse (labeled as LP) and the blue lines show the result of a 1.2 ps short pulse (labeled as SP). After the transition timing (3.8 ps), the slope temperature of higher energy component rises sharply by 1.3 MeV.

of the higher energy component are accelerated in the underdense plasma and the acceleration mechanism was explained in Sec5.3 (shown is Fig.5-24).

Since the quasi-static magnetic field generated in the underdense plasma, takes time to grow, the effect that the REs are trapped by the magnetic field is only observed in 4 ps duration pulse.

Figure 5-25 shows the energy carried by the REB. The red line shows the energy carried by REs with energy less than 3 MeV contributing to fuel heating in fast ignition fusion. The green line shows the energy carried by REs with energy above 3 MeV. After the transition timing, energy of REB contributing to fuel heating decreases by about 13%, while energy of REB having energy

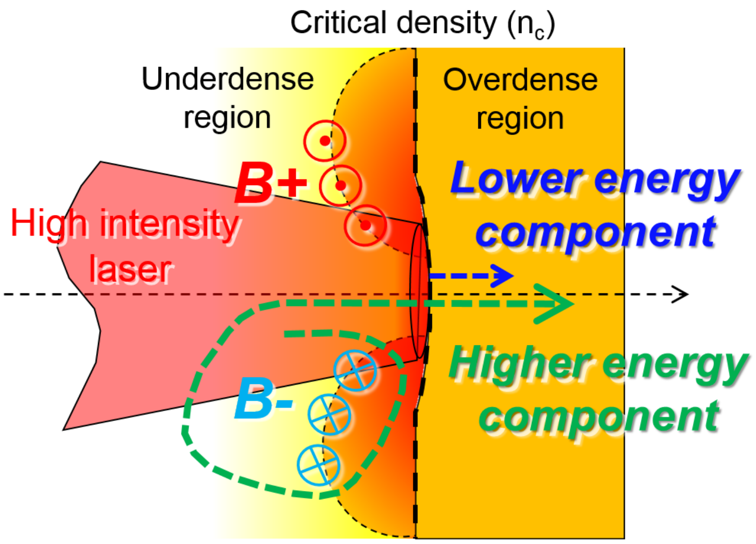

Figure 5-24: REs of the lower energy component are accelerated when the laser interacts with the relativistic critical density plasma. REs of the higher energy component are accelerated in the underdense plasma and the acceleration mechanism was explained in Sec5.3.

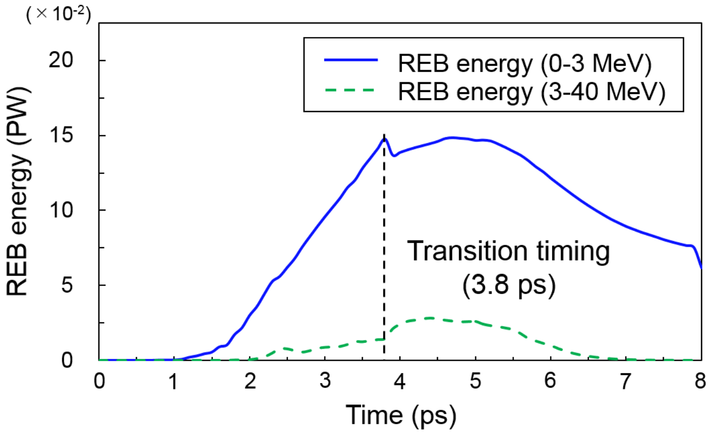

Figure 5-25: Energy carried by the REB. The red line shows the energy carried by REs with energy less than 3 MeV contributing to fuel heating in fast ignition fusion. The green line shows the energy carried by REs with energy above 3 MeV. After the transition timing, the energy of the REB contributing to the heating decreases while energy of the REB having energy above 3 MeV increases.

above 3 MeV increases. However, this reduction is not so significant problem because this loss is filled as soon as the energy conversion efficiency is increased. Thus, the scheme of reducing the laser intensity by extending the pulse duration is effective for the generation of REB with the optimum slope temperature for fuel heating.

5.7 | Conclusions

In the summary, the REs are accelerated efficiently above the reported scaling values by a laser field in a quasi-static electric field because dephasing of the RE from the laser field is reduced by this electric field. This electric field is generated by the charge separation at the forward edge of an expanding plasma. The quasi-static magnetic field is generated spontaneously near the bulk plasma surface by the $\nabla n \times \nabla I$ effect at the beginning of the laser irradiation, the $\nabla T \times \nabla n$ effect becomes a dominant mechanism of the magnetic field generation around a few ps after the laser irradiation, and finally $\boldsymbol{E} \times \boldsymbol{B}$ drift current and its return current produce a current loop to amplify rapidly the magnetic field strength owing to the positive feedback between the field growth and the field-driven drift current. When the self-generated magnetic field grows strong enough to reflect REs coming from the laser plasma interaction region back again there, the reflected REs gain additional energy by the laser field in the quasi-static electric field. Therefore, the timing of magnetic field generation, corresponds to the onset of increasing of the slope temperature of higher component of REs that is not effective to fuel heating in the fast ignition fusion research. Two-dimensional particle-in-cell simulation reveals that the magnetic field generation appear at 3.8 ps in which overdense plasma compression stops by laser ponderomotive pressure. A magnetic field rapidly grow in the expanding underdense plasma. The timing when the expansion of the underdense plasma occurred coincided with the transition timing of the plasma compression and blow off, and the expansion velocity of underdense is tripled from 3.8 ps.

The electron density threshold in which the compression of the relativistic critical density plasma terminates, can be derived by a new model considering the motion of ions and electrons at the interaction surface. By combining this density threshold with Eq.(5.14) describing the position of the plasma compression front and the initial ion density profile $n_i(x) = (\gamma_{os} n_c/Z)\exp[(x - x_c)/l_s]$, we can estimate the transition timing between the compression regime and the blow off regime. After the transition timing, the energy of the REB contributing to the heating decreases while energy of the REB having energy above 3 MeV increases.

In a time earlier than this timing, the electron temperature can be estimated by conventional scalings, however in a time later than the timing, the effect of pulse expansion can not be ignored and modification of scalings is necessary. However, this reduction of energy transfer to the lower energy component, is not so critical problem because this loss is filled as soon as the energy conversion efficiency is increased. Thus, the scheme of reducing the laser intensity by extending the pulse duration is effective for the generation of REB with the optimum slope temperature for fuel heating.

Furthermore, the acceleration mechanism of REs beyond ponderomotive energy reported in this chapter, is useful in applications such as ion acceleration and the laboratory astrophysics. Yogo *et al.* reported that the maximum proton energy is improved more than twice (from 13 to 33 MeV) by extending the pulse duration from 1.5 to 6 ps with fixed laser intensity of 10^{18} W/cm^2. The proton energies observed are discussed using a plasma expansion model newly developed that takes the electron temperature evolution beyond the ponderomotive energy in the over picoseconds interaction into account. The present results are quite encouraging for realizing ion-driven fast ignition and novel ion beamlines.

CHAPTER 6

Conclusion

This study has experimentally demonstrated the effect of the pulse duration of the heating laser on the relativistic electron acceleration. In carrying out this research, it was necessary to suppress generation of preplasma by foot pulse, pedestal and prepulse, which is irradiated to the target before reaching the main pulse of the heating laser. Because the preceding pulses create a preplasma with a scale length which is longer than that of a plasma generated by the main pulse. Therefore, 2 inch spherical plasma mirror was implemented in the LFEX system to improve laser pulse contrast. We measured a plasma mirror reflectivity of about 50% using a laser fluence of about 50 Jcm^2 on the mirror surface, limiting focal spot distortions. The transmission of the laser light energy through the plasma mirror was equal to $3.5\% \pm 2\%$, allowing us to estimate that the plasma mirror was triggered after a time of 2±1ps from the main peak. An improvement in the laser pulse contrast by a factor of 100 (and up to 10^{11}) was demonstrated on a kJ-class laser system. A significant reduction of the preplasma was observed by optical interferometry. This technique is very promising, not only for fast ignition but also for opening very broad applications, such as ion acceleration or setting up a configuration of two counter-propagating laser beams. This technique can also be applied as beam transportation in a highly complex large-energy laser facility, such as OMEGA-EP, ORION, PETAL, and NIF-ARC with 1 ps operation. High contrast laser pulse is possible to extract only the influence of the pulse duration of the main pulse on the electron acceleration. Furthermore, in carrying out this research, it was necessary to establish a new measurement method for average energy of REs and energy conversion efficiency. In this study, we converted relativistic electrons into bremsstrahlung x-rays that dose not be trapped by the field. Average energy of REs and energy conversion efficiency were obtained by a reconstruction of energy spectrum of bremsstrahlung x ray. In order to measure the energy spectrum of bremsstrahlung x ray, we developed Compton x-ray spectrometer, and it obtained higher spectral resolution than that of conventional bremsstrahlung x-ray spectrometers.

The above two improvements enabled us to study REs acceleration mechanism in an inherent plasma formed by the main laser pulse itself in 1-4 ps time range. Experimentally measured slope temperatures are far beyond the reported intensity scaling laws, which has no dependence of pulse durations. Experimental results were analyzed using two-dimensional particle-in-cell simulation. We revealed that the increasing of average energy of REs due to the long pulse irradiation causes not only to the long scale plasma generated by the main pulse itself but also to the quasi-static electric field and magnetic field spontaneously generated in the plasma. The REs are accelerated efficiently above the reported scaling values by a laser field in a quasi-static electric field because dephasing of the RE from the laser field is reduced by this electric field. This electric field is generated by the charge separation at the forward edge of an expanding plasma. The quasi-static magnetic field is generated spontaneously near the bulk plasma surface by the $\nabla n \times \nabla I$ effect at the beginning of the laser irradiation, the $\nabla T \times \nabla n$ effect becomes a dominant mechanism of the magnetic field generation around a few ps after the laser irradiation, and finally $\boldsymbol{E} \times \boldsymbol{B}$ drift current and its return current produce a current loop to amplify rapidly the magnetic field strength owing to the positive feedback between the field growth and the field-driven drift current. When the self-generated magnetic field grows strong enough to reflect REs coming from the laser plasma interaction region back again there, the reflected REs gain additional energy by the laser field in the quasi-static electric field. Therefore, the timing of magnetic field generation, corresponds to the onset of increasing of the average energy of electrons that is not desired in the fast ignition fusion research. Two-dimensional particle-in-cell simulation reveals that the magnetic field generation appear at 3.8 ps in which overdense plasma compression stops by laser ponderomotive pressure. A magnetic field rapidly grow in the expanding underdense plasma. The timing when the expansion of the underdense plasma occurred coincided with the transition timing of the plasma compression and blow off, and the expansion velocity of underdense is tripled from 3.8 ps.

The electron density threshold in which the compression of the relativistic critical density plasma terminates, can be derived by a new model considering the motion of ions and electrons at the interaction surface. By combining this density threshold with equation describing the position of the plasma compression front, we can estimate the transition timing between the compression regime and the blow off regime. After the transition timing, the energy of the REB contributing to the heating decreases while energy of the REB having energy above 3 MeV increases.

In a time earlier than this timing, the electron temperature can be estimated by conventional scalings, however in a time later than the timing, the effect of pulse expansion can not be ignored and modification of scalings is necessary. However, this reduction of energy transfer to the lower energy component, is not so critical problem because this loss is filled as soon as the energy conversion efficiency is increased. Thus, the scheme of reducing the laser intensity by extending the pulse duration is effective for the generation of REB with the optimum slope temperature for fuel heating.

Furthermore, the acceleration mechanism of REs beyond ponderomotive energy reported in this chapter, is useful in applications such as ion acceleration and the laboratory astrophysics.

The relation between the pulse duration of the laser and the time scale of the quasi-static electric field and the growth of the magnetic field was examined, and guidelines for determining the optimum laser parameters for fast ignition laser fusion were obtained.

CHAPTER 7

Appendix

7.1 | Appendix A: Nomarski-type interferometer

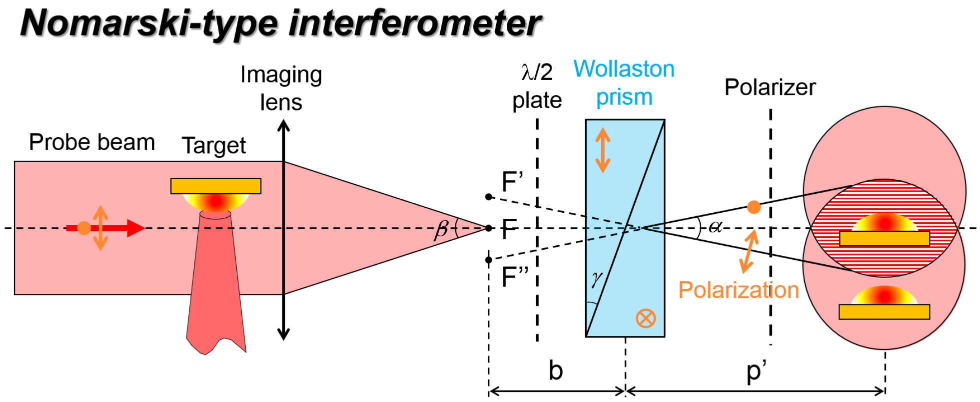

Figure 7-1: Schematic view of Nomarski-type interferometer. The peculiarity of this interferometric technique is that the reference beam is extracted from the same probe beam by splitting the orthogonal components of the electromagnetic wave polarization vectors using a birefringent Wollaston prism.

In our experiment, Nomarsky interferometry was used as an optical probing of the plasma generated by the prepulse. The peculiarity of this interferometric technique is that the reference beam is extracted from the same probe beam by splitting the orthogonal components of the electromagnetic wave polarization vectors using a birefringent Wollaston prism. It is therefore ideally suited for illumination with very short pulses with their inherently low temporal coherence. (In interferometers in which reference beams pass through different optical paths like Michelson type and Mach-Zehnder type interferometer, it is difficult to adjust the optical path between the two beams.) The spatial resolution of the system is determined only by the quality of the imaging lens and can therefore reach high values. (In Michelson type and Mach-Zehnder interferometers, the difference in the refractive index of the optical path between the reference beam and the object beam, affects the spatial resolution.) Wollaston prism is a polarizing beam splitter. It consists of two birefringent wedges (usually calcite, quartz or α-BBO crystal) put together to form a plane parallel plate. At the plane of separation between the two wedges, the one part of the incident ray is deflected to one direction, the other ray is deflected to the other direction by approximately the same angle. Since separated rays need to overlap in space, a Wollaston prism with a small separation angle is used (1-2°). The two separated beams have perpendicular polarizations and thus cannot interfere. Therefore, we use a polarizer to limit the polarization direction. When a polarizer rotated by 45° with respect to both polarizations is inserted behind the Wollaston prism, the polarizer reduces the intensities of both beams by a factor of 2, but they have parallel polarizations afterwards and can interfere in the overlapping region. A typical set up for the Nomarsky interferometer for plasma density measurement is reported in Fig.7-1. The distance of the interference fringes, i, in the plane of the CCD is given by

$$i = \frac{\lambda_L}{\alpha}\frac{p'}{b}. \tag{7.1}$$

7.2 | Appendix B: Pulse duration compression

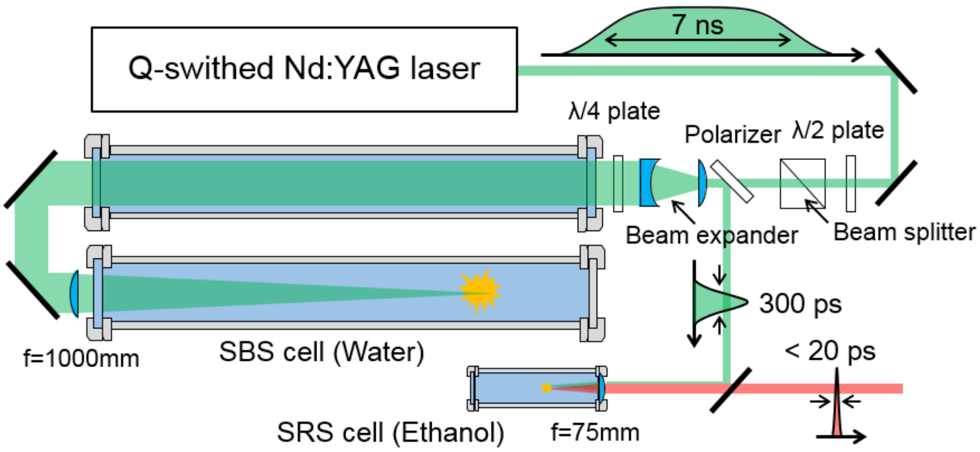

Figure 7-2: Schematic view of pulse compressor. The pulse compressor was composed of a pump source and the three cells filled by liquid. Cells for stimulated Brillouin scattering (SBS) were filled with pure water, which has favorable properties for SBS pulse compression. The cell for stimulated Raman scattering (SRS) was filled with ethanol.

Figure 7-2 shows the schematic view of pulse compressor. The pulse compressor is composed of a pump source and the cells filled by liquid. The compression cells are stainless steel pipes with windows at both ends. The pump source is a linearly polarized Q-switched Nd:YAG laser (7 ns, 532 nm), and it delivers pulse energy of 250 mJ. Input energy of pump laser into SBS cells, is controlled by the combination of a half-wave plate and a beam splitter. The pump laser (532 nm, 7 ns, 250 mJ) is expanded to 70 mm diameter to keep laser intensity below the stimulated Brillouin scattering (SBS) threshold in the amplifier cell (first SBS cell). Then, the laser is focused on the liquid of the second SBS cell after passing through the first SBS cell by a lens with 1000 mm focal length. The lens is placed in front of the input window of the second cell. Two SBS cells (1500 mm-long each) are arranged in parallel. They are filled with pure water, which has favorable properties for

SBS pulse compression. ex., short phonon lifetime (295 ps at 532 nm), moderate SBS gain (2.9 at 532 nm) and chemical stability. The cell length is determined by considering matching between the interaction length and the spatial pulse length (τ_p) of the pump laser ($c \times \tau_p \simeq n$), to accomplish high conversion efficiency. Here, c and n are speed of light and the refractive index of water, respectively. In our case ($\tau_p = 7$ ns), 1500 mm length cell is appropriate. When the energy of the pumping beam is about 250 mJ, about half of energy was returned as the energy of the compressed beam. [99, 100, 101, 102, 103, 104] The pulse after SBS compression goes through a quarter wave isolator and it is focused by a 90 mm focal length lens into ethanol to obtain a reflected pulse with shorter pulse duration. Focal length of the lens is chosen for efficient compression by SRS. Efficient compression by SRS requires following conditions; $\tau_p v 2 Z_R < 20$ and $\tau_p = 2Lv$. Here, L is the distance between the entry to the nonlinear medium and the focus, Z_R is the Rayleigh length, and v is the velocity of light in the medium. Estimates indicate that under our experimental conditions all these requirements are satisfied when the pump beam was focused by lens with $f=$ 90 mm. The wavelength of backward light by SRS is shifted to 630 nm. It is shifted by interaction with 3 C-H stretching vibration bands of ethanol molecule. In the pulse compression by backward SRS, generation of the concurrent scattering pulses (second pulse, third pulse etc.) is reported. Concurrent scattering pulses increase pulse duration. i.e., they reduce temporal resolution of interferometer. The strong parametric coupling reduces the efficiency of concurrent SRS when the normalized detuning is small so that $\gamma = \Delta(2\pi g I_p)$. Here, Δ is the linear detuning, g is the gain, and I_p is the pump intensity at the focus. Therefore, generation of concurrent SRS can control by adjustment of the energy of probe pulse. [105, 106] The temporal profiles of compressed pulses are measured using an optical streak camera when 3 mJ or 250 mJ pulse were injected to SRS cell.

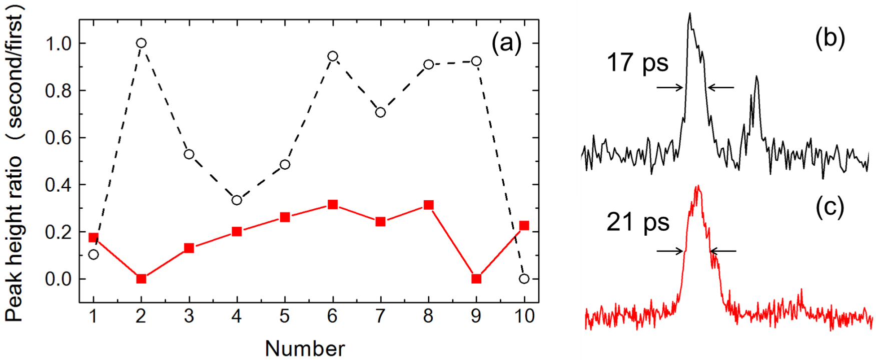

Figure 7-3: Peak height ratio between the first and the second concurrent SRS signal measured by using an optical streak camera. Concurrent SRS pulses are reduced by adjusting of the pump energy.

Figure 7-3(a) shows peak height ratio between the first and the second concurrent SRS signal measured by using an optical streak camera. Concurrent SRS pulses are reduced by adjusting of the pump energy. In the case of 250 mJ pump energy, the strong Stokes and anti-Stokes components of SRS concurrent was observed. Averaged peak height ratio (second/first) of ten data was calculated to be 0.59 (dashed line) with large deviation. While, for 3 mJ pump energy, single peak pulse was stably generated. Averaged peak height ratio (second/first) of ten data was calculated to be 0.2 (solid line) with small deviation. Full width at half maximum (FWHM) of average pulse duration was 21 ps. Figure 7-3(b) and (c) show the typical concurrent SRS signals in the case of (b) 250 mJ and (c) 3 mJ pump energy. In this paper, we have demonstrat-ed high-ratio (1:540) pulse compression by stimulated Brillouin scattering (SBS) in pure water and stimulated Raman scattering (SRS) in liquid ethanol. It can become an alternative approach to make the short pulse probe laser. Pulse compression from 7 ns (at 532 nm) to 21 ps (at 630 nm), was achieved by two stage compression system. This scheme using cells fulfilled liquid, provides potentially low cost and damage-less. Single peak pulse realize high temporal resolution, and enough brightness for the interferometry.

7.3 | Appendix C: GeV Electron Spectrometer (GESM)

A fraction of relativistic electrons (REs) accelerated by a laser pulse leave the target. The remaining positive charge creates strong sheath field that re-inject REs into the target. However a small fraction of REs with a sufficiently high energy can escape the target and propagate into vacuum. Energy distribution of escaping REs are characterized by an electron spectrometer (ESM). The basic principle of ESM is as follows. REs enter the spectrometer through a small slit. They are deflected in a static magnetic field created by permanent magnets. They are consequently dispersed along circular trajectories (Larmor motion) whose radius is determined by the electron energy. The detector records the arrival position of the REs.

This section describes ESM for electron up to 1 GeV (GeV electron spectrometer: GESM). The magnetic circuit used in the GESM, needs to have strong magnetic flux density to observe 1 GeV energetic electrons. In addition, to enhance accuracy of modeling of electron trajectory in the magnetic field, high spatial uniformity of magnetic flux density is necessary by suppressing leakage of the magnetic flux. For this purpose, it is common to cover the periphery of a powerful neodymium magnet with a yoke made of pure iron. The yoke is used to confine the magnetic flux in the magnetic circuit. Thus, we can design a more compact magnetic circuit.

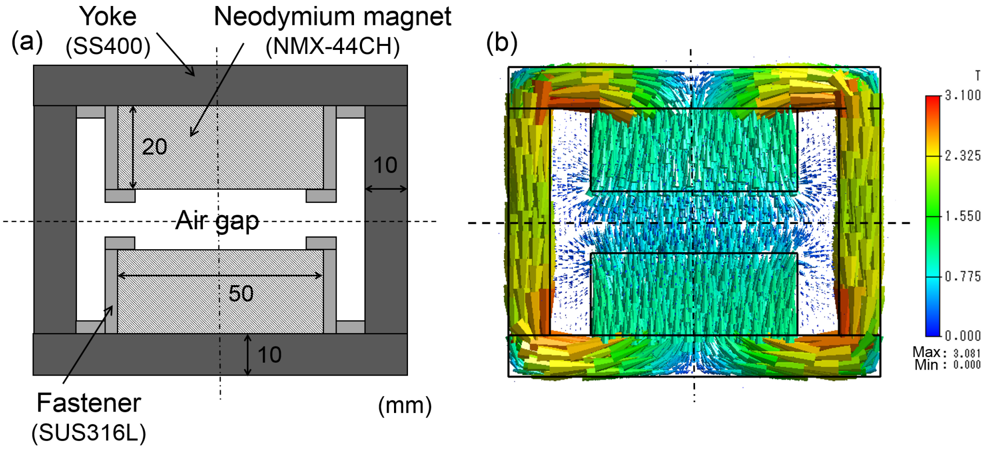

Figure 7-4: (a) Dipole magnet with hollow square yoke. (b) Magnetic flux density map calculated by Femet code.

Figure 7-4 (a) shows schematic view of the magnetic circuit of GESM. The design of the magnetic circuit of the dipole neodymium magnet with hollow square yoke was carried out using three-dimensional static magnetic field calculation software Femet distributed by Murata software. In this software, the parameters of the permanent magnet are defined as a magnetic hysteresis curve (BH curve). Figure 7-4 (b) shows spatial distribution of the magnetic flux density produced by the dipole magnet with a hollow square yoke. In this calculation, NMX-44CH, the neodymium magnet with high magnetic susceptibility (residual magnetic flux density Br = 1.33 T, coercive force Hcb = 1000 kA/m), of NEOMAX Inc. was used.

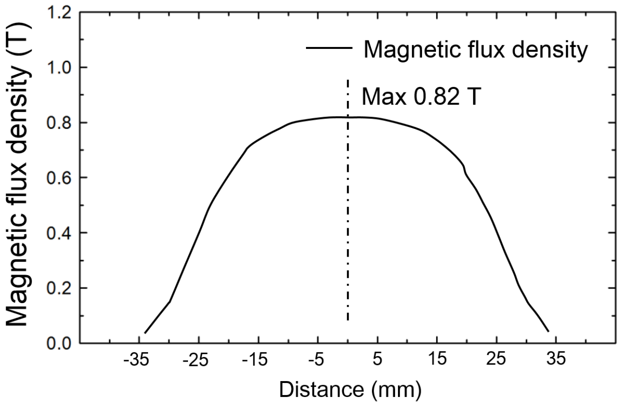

Figure 7-5: Spatial distribution of the magnetic flux density produced by the dipole magnet with a hollow square yoke. In this calculation, NMX-44CH, the neodymium magnet with high magnetic susceptibility (residual magnetic flux density Br = 1.33 T, coercive force Hcb = 1000 kA/m), of NEOMAX Inc. was used.

To make the magnetic circuit compact, thickness of the yoke was minimized. 1 cm thickness is found that the magnetic field can be transmitted efficiently without diverging the magnetic field to the vacuum region. The simulation results shows the magnetic flux density between the two magnets reaches a maximum of 0.82 T. The variation of magnetic field strength is less than 10% of the maximum value at 1.5 cm from center of the two magnets. The design drawing of a magnetic circuit and spatial distribution of magnetic flux density of this magnetic circuit are attached at the end of this section. The length of the magnetic circuit was designed to deflect 1 GeV electrons. To reduce the influence of a leakage magnetic field generated at both ends of the magnetic circuit, a 25-mm length of the magnetic-field-controlled plate was installed. When the magnetic field leakage outside the yoke, lower energy electrons are deflected in the electron collimator. And they collides with the inner wall of the collimator and is absorbed.

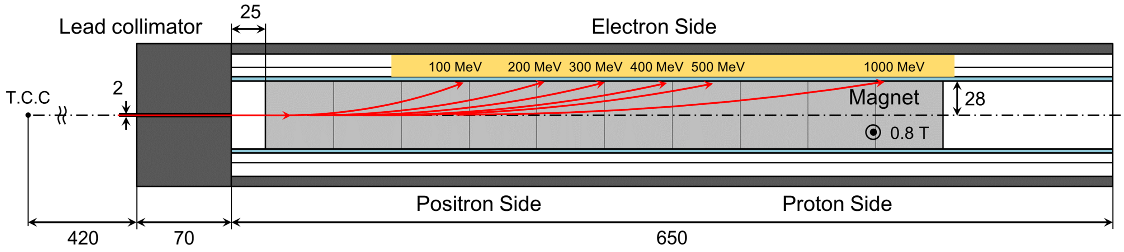

Figure 7-6: A cross section of the GESM core. In the traveling direction of electrons, ten pair of diepole magnet are arranged, and the length of the magnetic circuit reaches 500 mm.

A cross section of the GESM core is shown in Fig.7-6. In the traveling direction of electrons, ten pair of diepole magnet (shown in Fig.7-4) are arranged, and the length of the magnetic circuit reaches 500 mm. The energy coverage of the spectrometer varies for the mass and charge of the incident particle where electrons and positrons can be measured between 0.5-1000 MeV and protons between 1-100 MeV.

GESM was calibrated using a quasi-monoenergetic electron bunch accelerated by L-band Linac at ISIR, Osaka University. In the calibration experiment, kinetic energy of the linear accelerator was adjusted to 16.4 MeV or 26.1 MeV, and trajectories of electrons with each kinetic energy in the magnetic circuit were calibrated. Figure 7-6 (a) shows the signals observed by the electron side IP and by the positron side IP when 16.4 MeV electron bunch is injected. Comparison of both signals shows that quasi-monoenergetic electron signal is observed by only the electron side IP. The noise signal due to hard X-rays is relatively smaller than the electron signal. The diameter of signal is about 2.5 mm on the IP, and it shows that the electron collimator with the diameter of 2 mm works effectively. Almost all electrons that pass through the collimator, are detected within 9 mm of the effective observation width of IP (the distance between the magnets). As a result, it was found that the number of electrons can be accurately measured by integrating all the signals on the IP. Figure 7-6 (b) shows the relationship between the kinetic energy of electrons and the arrival position of electrons.

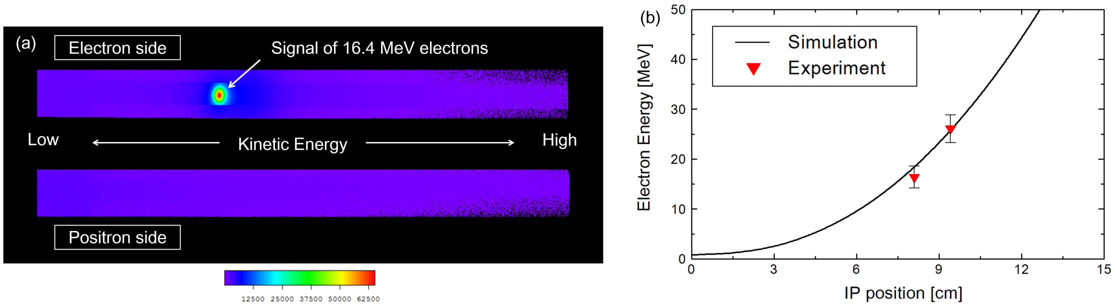

Figure 7-7: (a) The signals observed by the electron side IP and by the positron side IP for 16.4 MeV electron bunch. (b) The relationship between the kinetic energy of electrons and the arrival position of electrons.

7.4 | Appendix D: Equations

Maxwell equations

cgs-Gaussian units

Gauss's law	$\nabla \cdot \boldsymbol{D} = 4\pi\rho_e$
Gauss's law for magnetism	$\nabla \cdot \boldsymbol{B} = 0$
Faraday's law	$\nabla \times \boldsymbol{E} = -\frac{1}{c}\frac{\partial \boldsymbol{B}}{\partial t}$
Ampère's law with Maxwell's extension	$\nabla \times \boldsymbol{H} = \frac{4\pi}{c}\boldsymbol{J} + \frac{1}{c}\frac{\partial \boldsymbol{D}}{\partial t}$

SI (MKS) units

Gauss's law	$\nabla \cdot \boldsymbol{D} = \rho_e$
Gauss's law for magnetism	$\nabla \cdot \boldsymbol{B} = 0$
Faraday's law	$\nabla \times \boldsymbol{E} = -\frac{\partial \boldsymbol{B}}{\partial t}$
Ampère's law with Maxwell's extension	$\nabla \times \boldsymbol{H} = \boldsymbol{J} + \frac{\partial \boldsymbol{D}}{\partial t}$

Conversion from SI to cgs-Gaussian units

S I	cgs-Gaussian
$\boldsymbol{E} \Rightarrow \boldsymbol{E}$	$\epsilon_0 \Rightarrow 1/(4\pi)$
$\boldsymbol{D} \Rightarrow \boldsymbol{D}/(4\pi)$	$\mu_0 \Rightarrow 4\pi/c^2$
$\boldsymbol{H} \Rightarrow c\boldsymbol{H}/(4\pi)$	$\rho_e \Rightarrow \rho_e$
$\boldsymbol{B} \Rightarrow \boldsymbol{B}/c$	$\boldsymbol{J} \Rightarrow \boldsymbol{J}$

Other equations

cgs-Gaussian units

Lorentz force	$\boldsymbol{F} = q\left(\boldsymbol{E} + \frac{\boldsymbol{v} \times \boldsymbol{B}}{c}\right)$
Electromagnetic energy density	$q_{EM} = \frac{1}{8\pi}(\boldsymbol{E} \cdot \boldsymbol{D} + \boldsymbol{H} \cdot \boldsymbol{B})$
Poynting vector	$I_L = \frac{c}{4\pi}(\boldsymbol{E} \times \boldsymbol{H})$
Wave equation	$\nabla^2 \boldsymbol{E} - \frac{\epsilon\mu}{c^2}\frac{\partial^2 \boldsymbol{E}}{\partial t^2} - \nabla(\nabla \cdot \boldsymbol{E}) = \frac{4\pi\mu}{c^2}\frac{\partial \boldsymbol{J}}{\partial t}$
Wave equation	$\nabla^2 \boldsymbol{H} - \frac{\epsilon\mu}{c^2}\frac{\partial^2 \boldsymbol{H}}{\partial t^2} = \frac{4\pi}{c}\nabla \times \boldsymbol{J}$
Vector potential	$\boldsymbol{B} = \nabla \times \boldsymbol{A}$
Scalar potential	$\boldsymbol{E} = -\nabla\phi - \frac{1}{c}\frac{\partial \boldsymbol{A}}{\partial t}$

SI (MKS) units

Lorentz force $\boldsymbol{F} = q(\boldsymbol{E} + \boldsymbol{v} \times \boldsymbol{B})$

Electromagnetic energy density $q_{EM} = \frac{1}{2}(\boldsymbol{E} \cdot \boldsymbol{D} + \boldsymbol{H} \cdot \boldsymbol{B})$

Poynting vector $I_L = \boldsymbol{E} \times \boldsymbol{H}$

Wave equation $\nabla^2 \boldsymbol{E} - \frac{\epsilon\mu}{c^2}\frac{\partial^2 \boldsymbol{E}}{\partial t^2} - \nabla(\nabla \cdot \boldsymbol{E}) = \mu_0 \mu \frac{\partial \boldsymbol{J}}{\partial t}$

Wave equation $\nabla^2 \boldsymbol{H} - \frac{\epsilon\mu}{c^2}\frac{\partial^2 \boldsymbol{H}}{\partial t^2} = \nabla \times \boldsymbol{J}$

Vector potential $\boldsymbol{B} = \nabla \times \boldsymbol{A}$

Scalar potential $\boldsymbol{E} = -\nabla\phi - \frac{\partial \boldsymbol{A}}{\partial t}$

cgs-Gaussian units

Electron ion collision frequency

$$\nu_{ei} = \frac{4(2\pi)^{1/2} Z^2 e^4 n_i \ln\Lambda}{3\sqrt{m_e}(k_B T_e)^{3/2}} \approx 2.9 \times 10^{-6} \frac{Z^2 n_i \ (\mathrm{cm}^{-3}) \ln\Lambda}{[T_e \ (\mathrm{keV})]^{3/2}} \quad [s^{-1}]$$

Electric conductivity $\sigma_E = \frac{n_e e^2}{m_e \nu_{ei}} \approx 2.7 \times 10^{17} Z \left(\frac{T_e}{\mathrm{keV}}\right)^{3/2} \quad [s^{-1}]$

Debye length $\lambda_{De} = \left(\frac{k_B T_e}{4\pi e^2 n_{0e}}\right)^{1/3} \approx 743 Z \left(\frac{T_e \ (\mathrm{eV})}{n_{0e}\mathrm{cm}^{-3}}\right)^{1/2} \quad [\mathrm{cm}]$

Larmor radius	$r_e = \frac{m_e v_e c}{eB} \approx 2.38 \frac{T_e\ (\text{eV})^{1/2}}{B(\text{gauss})}$ [cm]
Plasma frequency	$\omega_{pe} = \left(\frac{4\pi e^2 n_e}{m_e}\right)^{1/2} \approx 5.64 \times 10^4 \sqrt{n_e}$ [rad/s]
Dielectric function	$\epsilon = 1 - \frac{\omega_{pe}^2}{\omega(\omega + i\nu)} = 1 + \frac{i4\pi\sigma_E}{\omega}$
Dispersion relation	$\omega^2 = \omega_{pe}^2 + k^2c^2 \qquad k^2 = \frac{\omega^2\epsilon}{c^2}$
Electric field	$E_{max}(\text{V/cm}) \approx 2.75 \times 10^9 \left(\frac{I_L}{10^{16}\ (\text{W/cm}^2)}\right)^{1/2}$
Magnetic field	$B_{max}(\text{Gauss}) \approx 9.2 \times 10^6 \left(\frac{I_L}{10^{16}\ (\text{W/cm}^2)}\right)^{1/2}$
Critical density	$n_c(\text{cm}^{-3}) \approx 1.1 \times 10^{21} \left(\frac{1\ \mu\text{m}}{\lambda_L}\right)^2$
Sound speed	$C_s(\text{cm/s}) = \left(\frac{Zk_BT_e}{m_i}\right)^{1/2} \approx 3 \times 10^7 \left[\left(\frac{Z}{A}\right)^{1/2} \left(\frac{T_e}{\text{keV}}\right)^{1/2}\right]$
Skin depth	$\delta = \frac{c}{\omega_p} \approx 1.68 \times 10^{-6} \left(\frac{10^{23}\ \text{cm}^{-3}}{n_e}\right)^{1/2}$ [cm]
Laser frequency	$\omega_L = \frac{2\pi c}{\lambda_L} \approx 1.88 \times 10^{15} \left(\frac{\mu\text{m}}{\lambda_L}\right)$ [s^{-1}]
Lamor frequency	$\omega_{ce} = \frac{eB}{m_e c} \approx 1.76 \times 10^{13} \left(\frac{B}{\text{MGauss}}\right)$ [s^{-1}]
Photon pressure	$P_L = \frac{I_L}{c}(1+R) \approx 3.3 \left(\frac{I_L}{10^{16}\ \text{W/cm}^2}\right)(1+R)$ [Mbar]
Plasma pressure	$P_e = n_e k_B T_e \approx 1.6 \left(\frac{n_e}{10^{21}\ \text{cm}^{-3}}\right)\left(\frac{T_e}{\text{keV}}\right)$ [Mbar]
Relativistic gamma	$\gamma \approx \left(1 + \frac{I_L\lambda_L^2}{1.37 \times 10^{18}(\text{W/cm}^2)\mu\text{m}^2}\right)^{1/2}$
Ponderomotive force	$\boldsymbol{f}_e = -\frac{\omega_{pe}^2}{16\pi\omega_L^2}\nabla E_s^2 = -\frac{\omega_{pe}^2}{8\pi\omega_L^2}\nabla < E^2 >$

CHAPTER 8

List of works

8.1 | Publications

First author

1. **Sadaoki Kojima**, Takahito Ikenouchi, Yasunobu Arikawa, Shohei Sakata, Zhe Zhang, Yuki Abe, Mitsuo Nakai, Hiroaki Nishimura, Hiroyuki Shiraga, Tetsuo Ozaki, Shuji Miyamoto, Masashi Yamaguchi, Akinori Takemoto, Shinsuke Fujioka, Hiroshi Azechi, *Development of Compton X-ray spectrometer for high energy resolution single-shot high-flux hard X-ray spectroscopy*, Review of Scientific Instruments, **87**, 4 043502 (2016).

2. **Sadaoki Kojima**, Yasunobu Arikawa, Yasuhiko Nishimura, Hiromi Togawa, Zhe Zhang, Takahito Ikenouchi, Tetsuo Ozaki, Alessio Morace, Takahiro Nagai, Yuki Abe, Shouhei Sakata, Hiroaki Inoue, Masaru Utsugi, Mitsuo Nakai, Hiroaki Nishimura, Hiroyuki Shiraga, Ryukou Kato, Shinsuke Fujioka, Hiroshi Azechi, *Accuracy evaluation of a Compton X-ray spectrometer with bremsstrahlung X-rays generated by a 6 MeV electron bunch*, Review of Scientific Instruments, **85**, 11 11D634 (2014).

3. **Sadaoki Kojima**, Yasunobu Arikawa, Alessio Morace, Masayasu Hata, Hideo Nagatomo, Tetsuo Ozaki, Shohei Sakata, Seung Ho Lee, Kazuki Matsuo, King Fai Farley Law, Shota Tosaki, Akifumi Yogo, Tomoyuki Johzaki, Atsushi Sunahara, Hitoshi Sakagami, Mitsuo Nakai, Hiroaki Nishimura, Hiroyuki Shiraga, Shinsuke Fujioka and Hiroshi Azechi, *Energy distribution of fast electrons accelerated by high intensity laser pulse depending on laser pulse duration*, Journal of Physics: Conference Series, **717**, 012102 (2016).

4. **Sadaoki Kojima**, Yasunobu Arikawa, Takahito Ikenouchi, Takahiro Nagai, Yuki Abe, Shouhei Sakata, Hiroaki Inoue, Takuya Namimoto, Shinsuke Fujioka, Mitsuo Nakai, Hiroyuki Shiraga, GEKKO-XII & LFEX Team, Tetsuo Ozaki, Makoto R Asakawa, Ryukou Kato, Hiroshi Azechi, *Development of Compton X-Ray Spectrometer for Fast Ignition Experiment*, Plasma and Fusion Research: Regular Articles, **9**, 4405109 (2014).

Coauthor

1. Yasunobu Arikawa, **Sadaoki Kojima**, Alessio Morace, Shohei Sakata, Takayuki Gawa, Yuki Taguchi, Yuki Abe, Zhe Zhang, Xavier Vaisseau, Eeung Ho Lee, Kazuki Matsuo, Shota Tosaki, Masayasu Hata, Koji Kawabata, Yuhei Kawakami, Masato Ishida, Koichi Tsuji, Satoshi Matsuo, Noboru Morio, Tetsuji Kawasaki, Shigeki Tokita, Yoshiki Nakata, Takahisa Jitsuno, Noriaki Miyanaga, Junji Kawanaka, Hideo Nagatomo, Akifumi Yogo, Mitsuo Nakai, Hiroaki Nishimura, Hiroyuki Shiraga, Shinsuke Fujioka, FIREX group, LFEX group, Hiroshi Azechi, Atsushi Sunahara, Tomoyuki Johzaki, Tetsuo Ozaki, Hitoshi Sakagami, Akito Sagisaka, Koichi Ogura, Alexander S. Pirozhkov, Masaharu Nishikino, Kiminori Kondo, Shunsuke Inoue, Kensuke Teramoto, Masaki Hashida, and Shuji Sakabe, *Ultrahigh-contrast kilojoule-class petawatt LFEX laser using a plasma mirror*, Applied Optics, **55**, 25 (2016).

2. Shinsuke Fujioka, Yasunobu Arikawa, **Sadaoki Kojima**, Tomoyuki Johzaki, Hideo Nagatomo, Hiroshi Sawada, Seung Ho Lee, Takashi Shiroto, Naofumi Ohnishi, Alessio Morace, Xavier Vaisseau, Shohei Sakata, Yuki Abe, Kazuki Matsuo, King Fai Farley Law, Shota Tosaki, Akifumi Yogo, Keisuke Shigemori, Yoichiro Hironaka, Zhe Zhang, Atsushi Sunahara, Tetsuo Ozaki, Hitoshi Sakagami, Kunioki Mima, Yasushi Fujimoto, Kohei Yamanoi, Takayoshi Norimatsu, Shigeki Tokita, Yoshiki Nakata, Junji Kawanaka, Takahisa Jitsuno, Noriaki Miyanaga, Mitsuo Nakai, Hiroaki Nishimura, Hiroyuki Shiraga, Kotaro Kondo, Mathieu Bailly-Grandvaux, Claudio Bellei, Joeao Jorge Santos, and Hiroshi Azechi, *Fast Ignition Realization Experiment with High-Contrast Kilo-Joule Peta-Watt Laser LFEX and Strong External Magnetic Field*, Physics of Plasmas, **23**, 056308 (2016).

3. K.F.F. Law, M. Bailly-Grandvaux, A. Morace, S. Sakata, K. Matsuo, **S. Kojima**, S. Lee, X. Vaisseau, Y. Arikawa, A. Yogo, K. Kondo, Z. Zhang, C. Bellei, J.J. Santos, S. Fujioka, and H. Azechi, *Direct measurement of kilo-tesla level magnetic field generated with laser-driven capacitor-coil target by proton deflectometry* Appl. Phys. Lett. **108**, 1 (2016).

4. A. Yogo, K. Mima, N. Iwata, S. Tosaki, A. Morace, Y. Arikawa, S. Fujioka, T. Johzaki, Y. Sentoku, H. Nishimura, A. Sagisaka, K. Matsuo, N. Kamitsukasa, **S. Kojima**, H. Nagatomo, M. Nakai, H. Shiraga, M. Murakami, S. Tokita, J. Kawanaka, N. Miyanaga, K. Yamanoi, T. Norimatsu, H. Sakagami , S. V. Bulanov, K. Kondo, and H. Azechi, *Boosting laser-ion acceleration with multi-picosecond pulses*, Scientific Reports, Accepted (2017).

5. Hui Chen, M Nakai, Y Sentoku, Y Arikawa, H Azechi, S Fujioka, C Keane, **S Kojima**, W Goldstein, B R Maddox, N Miyanaga, T Morita, T Nagai, H Nishimura, T Ozaki, J Park, Y Sakawa, H Takabe, G Williams and Z Zhang, *New insights into the laser produced electronpositron pairs* New J. Phys., **15**, 065010 (2013).

6. J.J. Santos, M. Bailly-Grandvaux, L. Giuffrida, P. Forestier-Colleoni, S. Fujioka, Z. Zhang, Ph. Korneev, R. Bouillaud, S. Dorard, D. Batani, M. Chevrot, J. Cross, R. Crowston, J.-L. Dubois, J. Gazave, G. Gregori, E. d'Humires, S. Hulin, K. Ishihara, **S. Kojima**, E. Loyez, J.-R. Marqus, A. Morace, Ph. Nicola, O. Peyrusse, A. Poy, D. Raffestin, J. Ribolzi, M. Roth, G. Schaumann, F. Serres, V.T. Tikhonchuk, Ph. Vacar, N. Woolsey, *Laser-driven platform for generation and characterization of strong quasi-static magnetic fields*, New J. Phys., **17**, 083051 (2015).

7. Z. Zhang, H. Nishimura, T. Namimoto, S. Fujioka, Y. Arikawa, H. Nagatomo, M. Nakai, T.

Ozaki, M. Koga, T. Johzaki, A. Sunahara, H. Chen, J. Park, G.J. Williams, H. Shiraga, **S. Kojima**, M. Nishikino, T. Kawachi, H. Hosoda, Y. Okano, N. Miyanaga, J. Kawanaka, Y. Nakata, T. Jitsuno, H. Azechi, *Quantitative measurement of hard X-ray spectra from laser-driven fast ignition plasma*, High Energy Density Physics, **9**, 435438 (1013).

8. G. Jackson Williams, Brian R. Maddox, Hui Chen, **Sadaoki Kojima** and Matthew Millecchia, *Calibration and equivalency analysis of image plate scanners* Rev. Sci. Instrum., **85**, 11E604 (2014)

9. Y. Arikawa, T. Nagai, H. Hosoda, Y. Abe, **S. Kojima**, S. Fujioka, N. Sarukura, M. Nakai, H. Shiraga, T. Ozaki and H. Azechi, *The photonuclear neutron and gamma-ray backgrounds in the fast ignition experiment* Rev. Sci. Instrum., **83**, 10D909 (2012)

10. Y. Abe, H. Hosoda, Y. Arikawa, T. Nagai, **S. Kojima**, S. Sakata, H. Inoue, Y. Iwasa, K. Iwano, K. Yamanoi, S. Fujioka, M. Nakai, N. Sarukura, H. Shiraga, T. Norimatsu and H. Azechi, *Characterizing a fast-response, low-afterglow liquid scintillator for neutron time-of-flight diagnostics in fast ignition experiments* Rev. Sci. Instrum., **85**, 11E126 (2014)

11. Y. Arikawa, T. Nagai, Y. Abe, **S. Kojima**, S. Sakata, H. Inoue, M. Utsugi, Y. Iwasa, T. Murata, N. Sarukura, M. Nakai, H. Shiraga, S. Fujioka and H. Azechi, *Development of multichannel low-energy neutron spectrometer* Rev. Sci. Instrum., **85**, 11E125 (2014)

12. S. Sakata, Y. Arikawa, **S. Kojima**, T. Ikenouchi, T. Nagai, Y. Abe, H. Inoue, A. Morace, M. Utsugi, R. Kato, H. Nishimura, M. Nakai, H. Shiraga, S. Fujioka and H. Azechi, *Photonuclear reaction based high-energy x-ray spectrometer to cover from 2 MeV to 20 MeV* Rev. Sci. Instrum., **85**, 11D629 (2014)

13. T Ozaki, A Sunahara, H Shiraga, Y Arikawa, S Fujioka, H Sakagami, Z Zhang, H Nagatomo, T Johzaki, T Namimoto, M Taga, **S Kojima**, Y Abe, K Ishihara, T Nagai, S Sakata, S Hattori, Y Sakawa, H Nishimura, H Azechi and FIREX Group, *Hot electron spectra in hole-cone shell targets and a new proposal of the target for fast ignition in laser fusion* Phys. Scr., **T161**, 014025 (2014)

14. T. Ozaki, **S. Kojima**, Y. Arikawa, H. Shiraga, H. Sakagami, S. Fujioka and R. Kato, *An electron/ion spectrometer with the ability of low energy electron measurement for fast ignition experiments*, Rev. Sci. Instrum., **85**, 11E113 (2014)

15. Hiroaki INOUE, Yasunobu ARIKAWA, Sinya NOZAKI, Shinsuke FUJIOKA, Takahiro NAGAI, **Sadaoki KOJIMA**, Yuki ABE, Shohei SAKATA, Atushi KINJO, Mitsuo NAKAI, Hiroyuki SHIRAGA and Hiroshi AZECHI, *The Neutron Imaging Diagnostics and Reconstructing Technique for Fast Ignition* Plasma and Fusion Research, **9**, 4404108 (2014).

16. Takahiro NAGAI, Mitsuo NAKAI, Yasunobu ARIKAWA, Yuki ABE, **Sadaoki KOJIMA**, Shohei SAKATA, Hiroaki INOUE, Shinsuke FUJIOKA, Hiroyuki SHIRAGA, Nobuhiko SARUKURA, Takayoshi NORIMATSU and Hiroshi AZECHI, *The Development of the Neutron Detector for the Fast Ignition Experiment by using LFEX and Gekko XII Facility*, Plasma and Fusion Research, **9**, 4404105 (2014).

17. Yuki ABE, Hirokazu HOSODA, Yasunobu ARIKAWA, Takahiro NAGAI, **Sadaoki KOJIMA**, Shohei SAKATA, Hiroaki INOUE, Yuki IWASA, Keisuke IWANO, GEKKO-XII&LFEX Team, Shinsuke FUJIOKA, Hiroyuki SHIRAGA, Mitsuo NAKAI, Takayoshi NORIMATSU and Hiroshi AZECHI, *Development of Multichannel Time-of-Flight Neutron Spectrometer for the Fast Ignition Experiment* Plasma and Fusion Research, **9**, 4404110 (2014).

18. Yasunobu ARIKAWA, Masaru UTSUGI, Morace ALESSIO, Takahiro NAGAI, Yuki ABE, **Sadaoki KOJIMA**, Shohei SAKATA, Hiroaki INOUE, Shinsuke FUJIOKA, Zhe ZHANG, Hui CHEN, Jaebum PARK, Jackson WILLIAMS, Taichi MORITA, Yoichi SAKAWA, Yoshiki NAKATA, Junji KAWANAKA, Takahisa JITSUNO, Nobuhiko SARUKURA, Noriaki MIYANAGA, Mitsuo NAKAI, Hiroyuki SHIRAGA, Hiroaki NISHIMURA and Hiroshi AZECHI, *High-Intensity Neutron Generation via Laser-Driven Photonuclear Reaction* Plasma and Fusion Research, **10**, 2404003 (2015).

19. Zhe ZHANG, Hiroaki NISHIMURA, Shinsuke FUJIOKA, Yasunobu ARIKAWA, Mitsuo NAKAI, Hideo NAGATOMO, Hiroyuki SHIRAGA, **Sadaoki KOJIMA**, Alessio MORACE, Noriaki MIYANAGA, Junji KAWANAKA, Yoshiki NAKATA, Takahisa JITSUNO, Hiroshi AZECHI, Tetsuo OZAKI, Hui CHEN, Jaebum PARK, Gerald Jackson WILLIAMS, Tomoyuki JOHZAKI and Atsushi SUNAHARA, *Energy Transportation by MeV Hot Electrons in Fast Ignition Plasma Driven with LFEX PW Laser* Plasma and Fusion Research **9**, 1404118 (2014).

20. Shinsuke Fujioka, Tomoyuki Johzaki, Yasunobu Arikawa, Zhe Zhang, Alessio Morace, Takahito Ikenouchi, Tetsuo Ozaki, Takahiro Nagai, Yuki Abe, **Sadaoki Kojima**, Shohei Sakata, Hiroaki Inoue, Masaru Utsugi, Shoji Hattori, Tatsuya Hosoda, Seung Ho Lee, Keisuke Shigemori, Youichiro Hironaka, Atsushi Sunahara, Hitoshi Sakagami, Kunioki Mima, Yasushi Fujimoto, Kohei Yamanoi, Takayoshi Norimatsu, Shigeki Tokita, Yoshiki Nakata, Junji Kawanaka, Takahisa Jitsuno, Noriaki Miyanaga, Mitsuo Nakai, Hiroaki Nishimura, Hiroyuki Shiraga, Hideo Nagatomo, and Hiroshi Azechi, *Heating Efficiency Evaluation with Mimicking Plasma Conditions of Integrated Fast-Ignition Experiment* Physical Review E, **91**, 063102 (2015).

Bibliography

[1] J. Nuckolls, L. Wood, A. Thiessen, and G. Zimmerman, Nature **239**, 139 (1972).

[2] M. Tabak *et al.*, Physics of Plasmas **1**, 1626 (1994).

[3] D. STRICKLAND and G. MOUROU, **56**, 219 (1985).

[4] S. Atzeni, Physics of Plasmas **6**, 3316 (1999).

[5] S. Atzeni and M. Tabak, Plasma Physics and Controlled Fusion **47**, B769 (2005).

[6] J. Honrubia and J. Meyer-ter Vehn, Nuclear Fusion **46**, L25 (2006), 0605249.

[7] R. P. J. Town *et al.*, Nuclear Instruments and Methods in Physics Research, Section A: Accelerators, Spectrometers, Detectors and Associated Equipment **544**, 61 (2005).

[8] S. Wilks, W. Kruer, M. Tabak, and A. Langdon, Physical Review Letters **69**, 1383 (1992).

[9] C. K. Li and R. D. Petrasso, Physics of Plasmas **13** (2006).

[10] S. Atzeni, A. Schiavi, and C. Bellei, Physics of Plasmas **14** (2007).

[11] A. A. Solodov, R. Betti, J. A. Delettrez, and C. D. Zhou, Physics of Plasmas **14** (2007).

[12] S. Rand, PHYSICAL REVIEW **136** (1964).

[13] T. V. George, L. Slama, M. Yokoyama, and L. Goldstein, Physical Review Letters **11**, 403 (1963).

[14] V. L. Ginzburg, *The Propagation of Electromagnetic Waves in Plasmas* .

[15] R. M. More, Z. Zinamon, K. H. Warren, R. Falcone, and M. Murnane, Journal de Physique **49**, 43 (1988).

[16] E. G. Camalii and V. T. Tikhonchunk, JETP Letters **48**, 453 (1988).

[17] T. Y. B. Yang, W. L. Kruer, R. M. More, and A. B. Langdon, Physics of Plasmas **2**, 3146 (1995).

[18] T. Y. B. Yang, W. L. Kruer, a. B. Langdon, and T. W. Johnston, Physics of Plasmas **3**, 2702 (1996).

[19] F. Brunel, PHYSICAL REVIEW LETTERS **59**, 6 (1987).

[20] D. W. Forslund, J. M. Kindel, L. Kenneth, E. L. Lindman, and R. L. Morse, Physical Review A **11** (1975).

[21] W. L. Kruer, *The Physics of Laser Plasma Interactions* (Addison-Wesley).

[22] E. Lefebvre and G. Bonnaud, Physical Review E **55**, 1011 (1997).

[23] G. Malka and J. Miquel, Physical Review Letters **77**, 75 (1996).

[24] W. L. Kruer and K. Estabrook, Physics of Fluids **28**, 430 (1985).

[25] D. Patin, A. Bourdier, and E. Lefebvre, Laser and Particle Beams , 297 (2005).

[26] D. Patin, E. Lefebvre, A. Bourdier, and E. D. Humières, Laser and Particle Beams , 223 (2006).

[27] S. Guerin *et al.*, Physics of Plasmas **2**, 2807 (1995).

[28] J. F. Drake *et al.*, Physics of Fluids **17**, 778 (1974).

[29] F. N. Beg *et al.*, Physics of Plasmas **4**, 447 (1997).

[30] H. U. I. Chen and S. C. Wilks, p. 411 (2005).

[31] T. Tanimoto *et al.*, Physics of Plasmas **16**, 062703 (2009).

[32] M. G. Haines, Can. J. Phys. **64**, 912 (1985).

[33] G. Malka *et al.*, Physical Review Letters **79**, 2053 (1997).

[34] B. Chrisman, Y. Sentoku, and a. J. Kemp, Physics of Plasmas **15**, 056309 (2008).

[35] A. J. Kemp, Y. Sentoku, and M. Tabak, Physical Review E - Statistical, Nonlinear, and Soft Matter Physics **79**, 1 (2009).

[36] J. Myatt *et al.*, Physics of Plasmas **14** (2007).

[37] P. M. Nilson *et al.*, Physical Review Letters **105**, 235001 (2010).

[38] K. Yasuike, M. H. Key, S. P. Hatchett, R. a. Snavely, and K. B. Wharton, Review of Scientific Instruments **72**, 1236 (2001).

[39] K. B. Wharton *et al.*, Physical Review Letters **81**, 17 (1998).

[40] C. D. Chen *et al.*, Physics of Plasmas **16** (2009).

[41] T. Ma *et al.*, Physics of Plasmas **16**, 112702 (2009).

[42] P. Kaw and J. Dawson, Physics of Fluids **13**, 472 (1970), arXiv:1011.1669v3.

[43] S. Ohira *et al.*, Journal of Applied Physics **112** (2012).

[44] I. Ross, P. Matousek, M. Towrie, a.J Langley, and J. Collier, Optics Communications **144**, 125 (1997).

[45] A. Sunahara, T. Johzaki, H. Nagatomo, and K. Mima, Laser and Particle Beams **30**, 95 (2012).

[46] K. H. Hong, B. Hou, J. A. Nees, E. Power, and G. A. Mourou, Applied Physics B: Lasers and Optics **81**, 447 (2005).

[47] J. Itatani, J. Faure, M. Nantel, G. Mourou, and S. Watanabe, Optics Communications **148**, 70 (1998).

[48] M. P. Kalashnikov *et al.*, AIP Conference Proceedings **1462**, 108 (2012).

[49] Y. Hama *et al.*, Springer Series in Optical Sciences **132**, 527 (2007).

[50] D. Hillier *et al.*, Applied optics **52**, 4258 (2013).

[51] G. Doumy *et al.*, Physical Review E - Statistical, Nonlinear, and Soft Matter Physics **69**, 1 (2004).

[52] B. Dromey, S. Kar, M. Zepf, and P. Foster, Review of Scientific Instruments **75**, 645 (2004).

[53] C. Ziener *et al.*, Journal of Applied Physics **93**, 768 (2003).

[54] T. Jitsuno *et al.*, Journal of Physics: Conference Series **112**, 032002 (2008).

[55] R. Nolte, R. Behrens, and P. Ambrosi, Radiation protection dosimetry **84**, 367 (1999).

[56] C. D. Chen *et al.*, Review of Scientific Instruments **79**, 2006 (2008).

[57] M. M. Gnther *et al.*, Physics of Plasmas **18**, 0 (2011).

[58] S. Sakata *et al.*, Review of Scientific Instruments **85**, 11D629 (2014).

[59] R. M. Malone *et al.*, IEEE International Conference on Plasma Science **032052**, 1 (2009).

[60] F. J. VERBINSKI, V. VICTOR, YOUNG, C. JACK, SAZAMA, Nuclear Instruments and Methods **37**, 243 (1976).

[61] G. L. Morgan *et al.*, Nuclear Instruments and Methods in Physics Research Section A: Accelerators, Spectrometers, Detectors and Associated Equipment **308**, 544 (1991).

[62] S. Kojima *et al.*, Review of Scientific Instruments **87**, 1 (2016).

[63] S. Kojima *et al.*, Plasma and Fusion Research **9**, 1 (2014).

[64] Sadaoki Kojima *et al.*, Review of Scientific Instruments **85**, 1 (2014).

[65] J. F. Briesmeister, MCNP - A General Monte Carlo N-Particle Transport Code Version 4C, 2000.

[66] S. Agostinelli *et al.*, Nuclear Instruments and Methods in Physics Research, Section A: Accelerators, Spectrometers, Detectors and Associated Equipment **506**, 250 (2003).

[67] T. Iwawaki *et al.*, The Review of scientific instruments **81**, 10E535 (2010).

[68] G. Jackson Williams, B. R. Maddox, H. Chen, S. Kojima, and M. Millecchia, Review of Scientific Instruments **85**, 11 (2014).

[69] S. Miyamoto *et al.*, Radiation Measurements **41**, 179 (2006).

[70] S. Fujioka *et al.*, Physical Review E **91**, 063102 (2015).

[71] K. A. Tanaka *et al.*, Citation: Review of Scientific Instruments Sci. Instrum **76**, 13507 (2005).

[72] H. Chen *et al.*, Review of Scientific Instruments **79** (2008).

[73] G. Malka and J. Miquel, Physical Review Letters **77**, 75 (1996).

[74] M. Haines, M. Wei, F. Beg, and R. Stephens, Physical Review Letters **102**, 045008 (2009).

[75] T. Kluge *et al.*, Physical Review Letters **107**, 1 (2011).

[76] A. Pukhov, Z.-M. Sheng, and J. Meyer-ter Vehn, Physics of Plasmas **6**, 2847 (1999).

[77] A. J. Kemp and L. Divol, Physical Review Letters **109**, 1 (2012).

[78] A. Sorokovikova *et al.*, Physical Review Letters **116**, 1 (2016).

[79] A. G. Krygier, D. W. Schumacher, and R. R. Freeman, Physics of Plasmas **21** (2014), 1311.0910.

[80] Y. Arikawa *et al.*, Applied Optics **55**, 6850 (2016).

[81] H. Nagatomo *et al.*, Physics of Plasmas **14** (2007).

[82] Y. Sentoku and a. J. Kemp, Journal of Computational Physics **227**, 6846 (2008).

[83] A. P. L. Robinson, A. V. Arefiev, and D. Neely, Physical Review Letters **111**, 1 (2013), arXiv:1303.0233v2.

[84] A. P. L. Robinson, A. V. Arefiev, and V. N. Khudik, Physics of Plasmas **22**, 083114 (2015).

[85] B. S. Paradkar, S. I. Krasheninnikov, and F. N. Beg, Physics of Plasmas **19**, 0 (2012).

[86] R. N. Sudan, Physical Review Letters **70**, 3075 (1993).

[87] R. J. Mason and M. Tabak, Physical Review Letters , 1 (1998).

[88] J. a. Stamper *et al.*, Physical Review Letters **26**, 1012 (1971).

[89] M. Borghesi *et al.*, Physical Review Letters **80**, 5137 (1998).

[90] M. Borghesi, a. MacKinnon, a. Bell, R. Gaillard, and O. Willi, Physical Review Letters **81**, 112 (1998).

[91] C. E. Max, W. M. Manheimer, and J. J. Thomson, Physics of Fluids **21**, 128 (1978).

[92] P. A. Jaanimagi, N. A. Ebrahim, N. H. Burnett, and C. Joshi, Applied Physics Letters **38**, 734 (1981).

[93] B. S. Paradkar *et al.*, Plasma Physics and Controlled Fusion **52**, 125003 (2010).

[94] D. W. Forslund and J. U. Brackbill, Physical Review Letters **48**, 1614 (1982).

[95] Y. Ping *et al.*, Physical Review Letters **109**, 1 (2012).

[96] H. Vincenti *et al.*, Nature communications **5**, 3403 (2014), 1312.1908.

[97] Y. Sentoku, W. Kruer, M. Matsuoka, and A. Pukhov, FUSION SCIENCE AND TECHNOLOGY **49**, 278 (2006).

[98] Z. Y. Ge *et al.*, Physical Review E - Statistical, Nonlinear, and Soft Matter Physics **89**, 1 (2014).

[99] R. R. Buzyalis, A. S. Dement, and . . Kosenko, Soviet Journal of Quantum Electronics **15**, 1335 (1985).

[100] E. Gaizhauskas *et al.*, Soviet Journal of Quantum Electronics **16**, 854 (1986).

[101] R. R. Buzyalis *et al.*, Soviet Journal of Quantum Electronics **17**, 1444 (1987).

[102] V. B. Ivanov, A. A. Mak, S. B. Papernyi, and V. A. Serebryakov, Soviet Journal of Quantum Electronics **16**, 560 (1986).

[103] D. T. Hon, Optics Letters **5**, 516 (1980).

[104] C. B. Dane, W. a. Neuman, and L. a. Hackel, Optics letters **17**, 1271 (1992).

[105] V. Kubecek, K. Hamal, I. Prochazka, and P. Valach, OPTICS COMMUNICATIONS **73**, 251 (1989).

[106] H. Search *et al.*, Soviet Journal of Quantum Electronics **18**, 1035 (1988).